

## ABSTRACT

Title of Document: CONSTRUCTING HYBRID NANO-  
STRUCTURES OUT OF NOBLE METALS  
AND SEMICONDUCTORS

Huizhi Bai, Ph.D., 2015

Directed By: Professor and Chair, Janice Reutt-Robey,  
Department of Chemistry and Biochemistry

Fabrication of complex hybrid nanostructures with tunable properties is desirable to fulfill functional applications in multidisciplinary areas. Manipulation of pre-designed nanostructure building blocks composed of distinct materials to achieve finite control over crystallinity, morphology, and composition is a major challenge. This dissertation aims to address the topic and create material with new optical properties. Questions explored are: How to realize delicate control on crystallinity of hybrid nanostructures through unconventional synthetic routes? How to achieve precise hybridized nanostructures with designed geometry, topology and composition? How do these features affect optical properties? Specifically, this dissertation contains recent efforts on fabrication and characterization of functional hybrid nanostructures made from metal and semiconducting materials. I first present a critical review of a monocrystalline nonepitaxially grown metallic @ semiconducting core @ shell hybrid nanostructures. This includes a comprehensive description of the novel

nonepitaxial synthetic route, emphasizing critical experimental steps, anticipation of challenges, and ending with my perspective. This systematic review should expand knowledge of the newly developed nonepitaxial method and spread technical aspects of the experiments. I then introduce an anisotropically shaped semiconducting nanocrystal with binary alloy composition. The rod-shaped ensemble has exhibited tunable bright band gap fluorescence that is dependent on dimension. This work is the first to achieve binary semiconducting alloy nanocrystals with anisotropic shapes. Interestingly, the electronic behavior within the rod-shaped semiconducting nanocrystals is altered due to gradient element distribution of the binary material, which is of fundamental interest and potential practical importance. Lastly, a core – metallic satellites-styled nanoparticle assembly structure will be discussed. Control over Ag nanoparticles as surrounding satellites in terms of size, shape and quantity is achieved via a facile synthetic route, and a collective electronic (dipole – dipole coupling) behavior within the metallic assembly is observed, and supported by numerical simulation. This work provides a new facile pathway to achieve well-controlled silica – Ag hybrid nanostructures.

CONSTRUCTING HYBRID NANOSTRUCTURES OUT OF NOBLE METALS  
AND SEMICONDUCTORS

By

Huizhi Bai

Dissertation submitted to the Faculty of the Graduate School of the  
University of Maryland, College Park, in partial fulfillment  
of the requirements for the degree of  
Doctor of Philosophy  
2015

Advisory Committee:  
Professor and Chair Janice Reutt-Robey, Chair  
Professor John Fourkas  
Professor Sang Bok Lee  
Professor Bryan Eichhorn  
Professor Lourdes Salamanca-Riba

© Copyright by  
Huizhi Bai  
2015

# Dedication

To

My Grandmother Wenyi Ming Bai

柏明文义

## Acknowledgements

This acknowledgement is unlikely to cover all the people to whom I want to say many thanks. The long journey in Maryland has involved so many care, support and grace. Here I would like to begin by acknowledging my advisor Prof. Reutt-Robey, for her tremendous help and support during my PhD study, without which this dissertation wouldn't be possible.

I would like to thank Prof. Min Ouyang, for supporting me to conduct research in his lab and providing me guidance and suggestions whenever I needed. His perseverance and dedication of himself in research have been constantly encouraging me to go through a lot of the difficulties. Thanks to Prof. Jiatao Zhang, for he had taught me a lot in experimental work when I was a freshman in the area, with his kindness, patience and abundant experience in chemistry lab. I had always enjoyed the time we worked together. Thanks Dr. Kwan Lee to help me with the TEM characterization at the beginning of my research. Thanks Dr. Lin Weng, for any helpful discussion in the lab.

I would also like to acknowledge Dr. Li-Chung Lai, for his patient training of Transmission Electron Microscope on me.

I would like to especially thanks to Prof. Salamanca-Riba and Mr. Joshua Taillon to help me with EDS mapping characterization, and provide me their perspectives on results illustration. The collaboration with Josh in AIM lab had been enjoyable.

I would express my appreciation to Dr. Yvonne Oslin, for her constant support, unconditional care, and her always-amiable eyes on me.

Thanks to Dr. Lifang Ma, Mr. Yi-Hsieh Wang, for their unconditional cares and supports, as well as all the other sisters, brothers and friends in MCBSG.

Finally, thanks to my husband, Mr. Zhiyue Lu, and my brother in law, Mr. Zhixin Lu, without whose supports this dissertation wouldn't be possible. The pursuit of my PhD in Maryland is rewarding and glorious in my life.

# Table of Contents

Dedication.....	ii
Acknowledgements .....	iii
Table of Contents .....	v
List of Tables.....	vii
List of Figures.....	viii
List of Abbreviations .....	x
Chapter 1: Introduction.....	1
1. Motivation and Overview .....	1
2. Fundamental Background of Nanoparticles .....	3
2.1 Noble Metal Nanoparticles .....	3
2.2 Semiconducting Nanoparticles .....	8
3. Hybrid Nanostructures.....	14
3.1 Plasmonic Hybrid Nanostructures with concentric core @ shell morphology.....	14
3.2 Plasmonic Hybrid Nanostructures with dumbbell morphology.....	17
Chapter 2: Monocrystalline Nonepitaxial Metal @ Semiconducting Hybrid Nanostructure: Synthesis, Challenges and Prospects .....	21
1. Introduction .....	21
2. Methodology of Synthesis.....	27
2.1 Overview of the Methodology.....	27
2.2 <i>Step 1.</i> Au @ Ag and Effect of Ag shell thickness .....	30
2.3 <i>Step 2.</i> Ligand Exchange and Effect of Alkanethiol on Shape Regulation.....	33
2.4 <i>Step 3.</i> Chalcogenation and amorphization of Ag shell: Chalcogenide Precursor and Morphology Control.....	35
2.5 <i>Step 4.</i> Cation Exchange to Produce Monocrystalline Shell.....	38
3. Shape Considerations: Size Scaling .....	41
4. Remaining Challenges.....	42
5. Conclusion and Prospects.....	45
Chapter 3: Anisotropically Shaped CdS <sub>x</sub> Se <sub>1-x</sub> Pseudobinary Semiconductor Nanocrystals .....	47
1. Introduction .....	47
2. Experimental Methods.....	50
2.1 Preparation of 4.5 nm spherical zinc blende CdSe seeds.....	50
2.2 General procedure to synthesize shaped CdS <sub>x</sub> Se <sub>1-x</sub> alloy nanocrystals.....	51
2.3 Characterization .....	55
3. Results and Discussion .....	56
4. Perspective on Synthesis and Growth Mechanism.....	68
5. Conclusion.....	73
Chapter 4: Silica – Ag Satellites Nanostructure – Facile Synthesis and Study of Plasmon – Plasmon Coupling.....	74
1. Introduction .....	74
2. Experimental Methods.....	76



2.1	Synthesis of Silica-Ag Satellites Nanostructure .....	76
2.2	Synthesis of Core @ Spacer – Satellites Metallic Assembly.....	79
2.3	Synthesis of silica-CdSe quantum dots composites from silica-Ag composites .....	80
3.	Facile Synthesis of Silica – Ag Satellites Nanostructures.....	83
4.	Core @ Spacer – Satellites Metallic Assembly: Dipole – Dipole Interaction Between Metallic NPs .....	88
5.	Simulation of the Dipole – Dipole Interaction .....	94
6.	Chemical conversion of silica-Ag into hydrophilic silica-CdSe quantum dots composites from silica-Ag composites.....	101
7.	Summary.....	103
Chapter 5: Summary and Future Outlook .....		105
Bibliography .....		108

## List of Tables

Table 2-1	Summary of monocrystalline Au @ semiconducting hybrid nanostructures with various morphologies prepared via nonepitaxial method.....	44
Table 3-1	Reaction conditions for different anisotropically shaped semiconducting nanocrystal products and compositions .....	54
Table 3-2	Cd precursor-free reaction conditions with fixed 144 mM octanethiol injection concentration.....	69
Table 4-1	Synthetic parameters for controlled silica-Ag hybrid NPs formation.	77
Table 4-2	Parameters for Drude model used in the simulation.....	96
Table 4-3	Parameters used in simulation shown in Figure 4-9 .....	98
Table 4-4	Parameters used in simulation shown in Figure 4-10 .....	99

## List of Figures

Figure 1-1	Schematic illustration of the collective oscillations of free electron.....	5
Figure 1-2	Wavelength Tunable SPR of gold nanorods and silver nanoplate by varying the aspect ratios and edge lengths, respectively.....	7
Figure 1-3	Schematic spatial correlated electronic state diagram of bulk semiconducting material and the corresponding nanocrystal states.....	8
Figure 1-4	Size dependent band gap engineering of colloidal CdSe quantum dots.....	11
Figure 1-5	Change in optical property of CdSe quantum dot after surface protection with a CdS shell.....	12
Figure 1-6	Au @ CdSe core @ shell hybrid nanostructure integrates a surface plasmon of the Au core with an exciton of the monocrystalline CdSe shell .....	16
Figure 1-7	Purified plasmonic monomers, dimmers and trimmers.....	19
Figure 2-1	Nonepitaxial growth of isotropic monocrystalline Au @ semiconducting core @ shells hybrid nanostructure.....	23
Figure 2-2	Low-revolution TEM images of anisotropically shaped Au @ CdS core @ shell nanostructures showing the overall distribution and morphologies .....	25
Figure 2-3	Schematic illustration of a precision synthetic route to achieve anisotropic monocrystalline Au @ semiconducting core @ shells hybrid nanostructure.....	28
Figure 2-4	TEM characterization of the Au @ Ag core @ shell nanostructures where the Au @ CdS was convert from .....	32
Figure 2-5	Surface passivation of Au @ Ag nanorod core @ shell by dodecanethiol.....	34
Figure 2-6	Time-evolution of reaction between Ag shell and S precursor under surface passivation with C <sub>10</sub> H <sub>22</sub> S molecules .....	35
Figure 2-7	Different morphology of Au @ Ag <sub>2</sub> Se rod.....	36
Figure 2-8	High-resolution TEM images of a single Au @ PbS rod.....	39
Figure 2-9	Au @ CdS triangular plate of different edge size.....	42
Figure 3-1	Synthetic route to various anisotropically shaped CdS <sub>x</sub> Se <sub>1-x</sub> nanocrystals from zinc blende spherical CdSe seeds.....	49
Figure 3-2	Illustration of the experimental setup to synthesize CdS <sub>x</sub> Se <sub>1-x</sub> alloy nanocrystals.....	52
Figure 3-3	Low-resolution TEM images showing different shapes of CdS <sub>x</sub> Se <sub>1-x</sub> semiconducting nanocrystals prepared under different reaction conditions .....	57
Figure 3-4A	Histogram of rod diameter.....	57
Figure 3-4B	Histogram of joint angle of the bi-pods.....	57
Figure 3-5	High-resolution TEM images of differently shaped semiconducting nanocrystals.....	58
Figure 3-6	EDS mapping characterization of a single rod-shaped semiconducting nanocrystal .....	61
Figure 3-7	EDS line scan of an individual CdS <sub>x</sub> Se <sub>1-x</sub> rod .....	62

Figure 3-8	TEM images showing size evolution of rod-shaped CdS <sub>x</sub> Se <sub>1-x</sub> nanocrystals.....	63
Figure 3-9	Composition control of CdS <sub>x</sub> Se <sub>1-x</sub> nanorods.....	63
Figure 3-10	Optical characterization and band gap energy of a series of rod-shaped CdS <sub>x</sub> Se <sub>1-x</sub> nanocrystals grown with varying reaction times.....	65
Figure 3-11	TEM image of spherical CdS <sub>0.36</sub> Se <sub>0.64</sub> nanoparticles.....	71
Figure 3-12	UV-Vis absorption spectrum of time-dependent heated 4.5 nm spherical CdSe seed .....	72
Figure 4-1	Illustration of synthetic route for silica – Ag satellites nanostructures.....	83
Figure 4-2	Low-resolution TEM images of Silica-Ag satellites nanostructures with different quantity of Ag NPs per silica .....	84
Figure 4-3	Low-resolution TEM images showing different size of Ag NPs on silica .....	85
Figure 4-4	Normalized extinction spectra of Silica-Ag satellites nanostructures samples .....	86
Figure 4-5	Extinction spectra of cube-shaped Ag NPs on silica and the corresponding TEM image.....	87
Figure 4-6	Characterization of Au @ silica – Ag nanostructure with 12 nm silica shell as spacer.....	90
Figure 4-7	Characterization of Au @ silica NPs before and after APS surface functionalization. ....	91
Figure 4-8	Characterization of Ag @ silica – Ag nanostructure with ~ 5 nm silica shell as spacer .....	93
Figure 4-9	Simulation of a single Au and Ag NP using different dipole spacing.....	97
Figure 4-10	Simulation results of a single Ag NP with two adjusted parameters (the medium refractive index and g factor).....	98
Figure 4-11	Simulation of Ag @ 5 nm spacer – Ag satellites structures. ....	100
Figure 4-12	Simulated normalized electric field amplitude  E/E <sub>0</sub>   distribution on a Ag @ 5 nm spacer – 60 Ag structure, upon 434 nm resonance excitation.....	101
Figure 4-13	Characterization of silica-CdSe composites emitting at 640 nm and 590 nm .....	102

## List of Abbreviations

–SH	1-decanethiol	28
1D	one-dimensional	11
APS	(3-aminopropyl) triethoxysilane	76
CTAB	cetyltrimethylammonium bromide	28
DDA	Discrete Dipole Approximation	6, 75, 94
EDS	Energy-Dispersive X-ray Spectroscopy	55
EG	ethylene glycol	78
fcc	faced-centered cube	59
FTIR	Fourier Transform Infrared Spectroscopy	33
FWHM	full width at half maximum	66, 103
HAADF	High-angle Annular Dark Field	55
hcp	hexagonal close packed	59
LSP	localized surface plasmon	4
NIR	near infrared	6, 24
NP (NPs)	nanoparticle(s)	3, 21, 74
OA	oleic acid	36, 50
ODE	octadecene	50
OSE	Optical Stark Effect	16, 23
PL	photoluminescence	56
PVP	polyvinylpyrrolidone	77
R.T.	room temperature	76
SERS	surface enhanced Raman scattering	7, 18, 74
SPP	surface plasmon polariton	4
SPR	surface plasmon resonance	4, 21, 74
ssDNA	single strand DNA	18
STEM	Scanning Transmission Electron Microscopy	55
TBP	tributylphosphine	23, 83
TEM	Transmission Electron Microscopy	7, 23, 55, 84
TEOS	tetraethyl orthosilicate	76
UV-Vis	Ultraviolet–visible	18, 51, 71, 80

# Chapter 1: Introduction

## 1. Motivation and Overview

The rapid development of nanoscience and nanotechnology has launched a revolution in scientific research [1, 2]. It comprises an enormous number of popular research topics that have expanded into interdisciplinary areas including physics, chemistry, biology, and material science. As foreseen by Feynman [3], the scaling of size to sub  $10^{-7}$  meters makes surface/interface and quantum effects play a critical role, with emergent physical properties in contrast to bulk materials. The new properties of nanomaterials can enable new technical applications.

Colloidal nanoparticles are one of the most attractive nanomaterials that highlight novel physical phenomena under quantum confinement and enable various functionalities for optics, electronics, catalyst, and biosensors [4-7]. Fabrication of these colloidal nanoparticles is via “bottom-up” strategy, which involves building nanostructures from atoms, ions and molecules into self-organized and stable aggregates at the nanoscale. Taking advantage of chemical strategies, the synthesis and manipulation of nanoparticles can be realized by adjusting macroscopic variables such as reaction temperature and time, and judicious choice of species and concentrations used. In practice, it is often not straightforward to precisely control nanoparticles ensembles for size, shape and uniformity, needed to engineer the

tunable physical properties that enable applications. What's more, it can be challenging to fabricate even pre-designed nanostructure building blocks composed of distinct materials (hybrid nanostructures) and simultaneously, achieve finite control over crystallinity, morphology, and composition.

This dissertation has aimed to address these issues from the following perspective: How to realize delicate control on crystallinity of nanostructures through unconventional synthetic route? How to achieve precise hybridized nanostructures with designed geometry, topology and composition? How do these features affect properties of the nanostructures?

With the motivation stated above, my PhD research has mainly focused on fabrication and characterization of functional hybrid nanostructures made from metal and semiconductor materials via bottom up synthetic routes. In this dissertation, a brief introduction of the fundamental background in nanoparticles and a selected review of the related field in hybrid nanostructures will be covered. Following this, Chapter 2 is a critical review of a monocrystalline nonepitaxial grown metallic @ semiconducting core @ shell hybrid nanostructures. This includes a comprehensive description of the novel nonepitaxial synthetic route, critical experimental steps, anticipation of challengings and insights drawn. In Chapter 3, I will introduce an anisotropically shaped semiconducting nanocrystal with binary alloy composition. This work is the first to achieve binary semiconducting alloy nanocrystals with anisotropic shapes. Interestingly, the electronic behavior within the rod-shaped

semiconducting nanocrystals is altered due to gradient element distribution of the binary material. Lastly, a core – satellite styled metallic nanoparticle assembly structure will be discussed in Chapter 4. Control over Ag nanoparticles as surrounding satellites in terms of size, shape and quantity is achieved via a facile synthetic route, and a collective electronic (dipole – dipole coupling) behavior within the metallic assembly is observed, and described by numerical simulation.

## 2. Fundamental Background of Nanoparticles

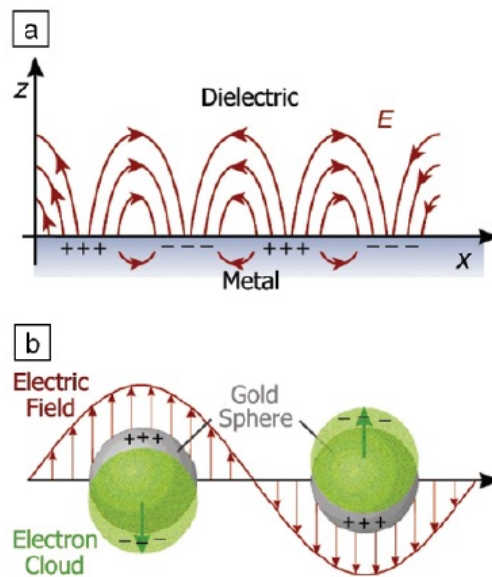
As in bulk single component materials, electronic behavior in noble metal and semiconducting nanoparticles with quantum confinement differ dramatically. This distinction is mainly due to the different bounding abilities of the nuclei toward the valence electrons. The background of noble metal and semiconducting nanoparticles and their fundamental properties are introduced as follows.

### 2.1 Noble Metal Nanoparticles

The history of noble metal nanoparticles (NPs) dates back to Roman times when bulk gold was dissolved and doped in glass exhibiting various lustrous colors after annealing [8]. However, people did not start to unveil the mystery until 1850s [9]. Michael Faraday prepared gold colloids by reduction of gold chloride with phosphorus and observed that the colloidal gold solutions have properties that differ from bulk gold. The fascinating properties of noble metal NPs intrinsically originate



from the free conductive electron in noble metal materials. Under exposure to irradiation of an oscillating electromagnetic wave (incident light), the free electrons are driven to propagate along the interface of the metal material and dielectric medium, coherently oscillating against the attraction of nuclei at a specific frequency (Figure 1-1). For bulk materials, the oscillating electron density wave is known as the surface plasmon polariton (SPP). When the noble metal material size is of nanoscale dimension, the SPP is confined within the boundary of the nanoparticle, and is called a localized surface plasmon (LSP) [10] (Figure 1-1b). Two important effects occur with a LSP. The electric field at the near vicinity of the NP is greatly enhanced, and concentrated locally at the nanoscale. Also, when the frequency of incident light matches the natural frequency of surface electron oscillations, a resonance condition is established and the NPs optical extinction cross-section ( $C_{ext}$ ) reaches a maximum. This is called a surface plasmon resonance (SPR). For noble metal NPs, the SPR occurs at the range of visible light.



**Figure 1-1 Schematic illustration of the collective oscillations of free electron:** (a) on a metal–dielectric interface (b) on a spherical gold colloid. Excited by the electric field of incident light, the free electrons can be collectively displaced from the lattice of positive ions (consisting of nuclei and core electrons). While the plasmon shown in (a) propagates across the surface as a charge density wave, the plasmon depicted in (b) is localized to each particle. (From Ref. [10])

For spherical NPs irradiated by an electromagnetic wave, Maxwell’s equation is exactly solvable by enforcing the boundary condition on the spherical surface. The exact solution describing light scattering and absorption features by the spherical NPs is known as Mie Theory, which predicts the extinction cross-section (sum of absorption and scattering cross section) to be [11]:

$$C_{ext}(\omega) = \frac{9\omega\epsilon_m^{3/2}V}{c} \frac{\epsilon_2(\omega)}{[\epsilon_1(\omega) + 2\epsilon_m]^2 + \epsilon_2(\omega)^2} \quad \text{Eqn 1-1}$$

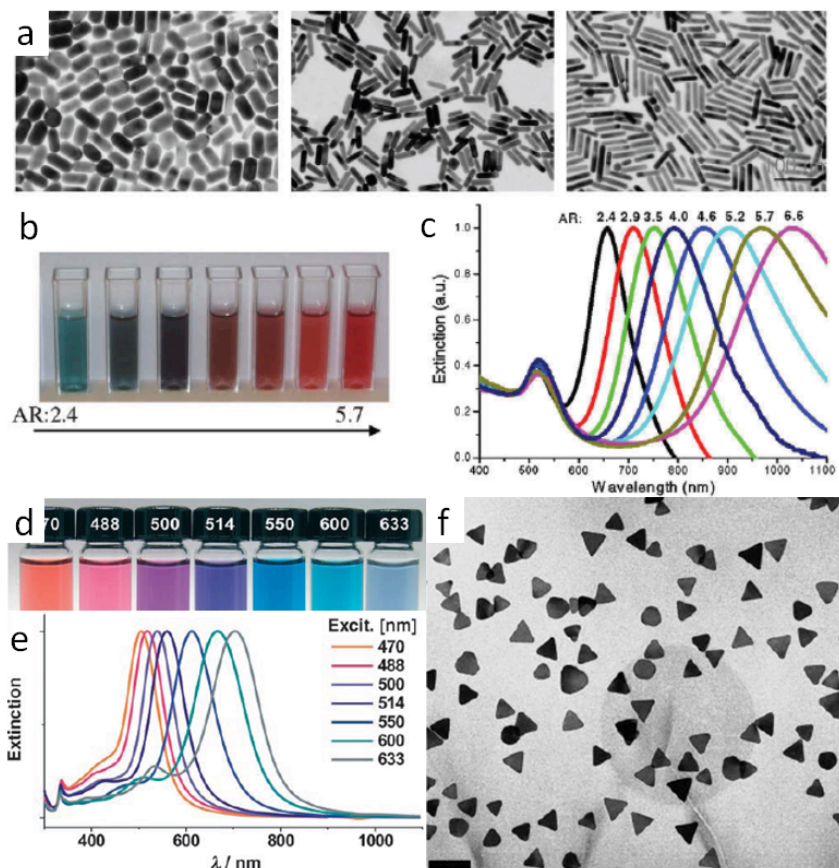
where  $\omega$  is the angular frequency of the incident light,  $V$  is the volume of a single NP and is equal to  $4/3\pi R^3$ ,  $c$  is the speed of light in vacuum, and  $\epsilon_m$  and  $\epsilon(\omega) = \epsilon_1(\omega) + i\epsilon_2(\omega)$  are the dielectric constant of the surrounding medium and the frequency dependent metal dielectric function, respectively. If  $\epsilon_2$  is small or weakly dependent on  $\omega$ , the resonance condition is determined by,

$$\epsilon_1(\omega) + 2\epsilon_m = 0 \quad \text{Eqn 1-2}$$

For arbitrary shapes (regular or irregular) of NPs, there may be no analytical solutions of Maxwell’s equation. Approximate methods are thus needed to simulate the electromagnetic interaction between arbitrary shaped NPs with incident light. The

Discrete Dipole Approximation (DDA) is one such method that is used in Chapter 4, to simulate the optical extinction by a Au and Ag NPs hybrid-assembled structure.

The features of SPR are strongly dependent on NP size [12, 13], shape [14, 15] and the dielectric constant of the surface environment.[16-18] The SPR frequency of noble metal NPs is tunable across the visible-near infrared (NIR) range, by varying the shape and size of the NPs. Typically, increasing NP dimension results in a red shift of SPR wavelength (Figure 1-2 d-f). For anisotropically shaped NPs, due to the reduced symmetry compared with the spherical case, additional plasmon modes occur associated with the collective electron oscillation along the different normal axes. For instance, Au nanorods show a transverse plasmon mode oscillating along the short-axes, and a longitudinal plasmon mode oscillating along the long-axis. The longitudinal plasmon mode has enhanced oscillator strength and a red shifted SPR wavelength dependent on the aspect ratio of the nanorod. As shown in Figure 1-2 a-c, the longitudinal plasmon wavelength is tunable from 600 nm to 1000 nm by increasing the aspect ratio.



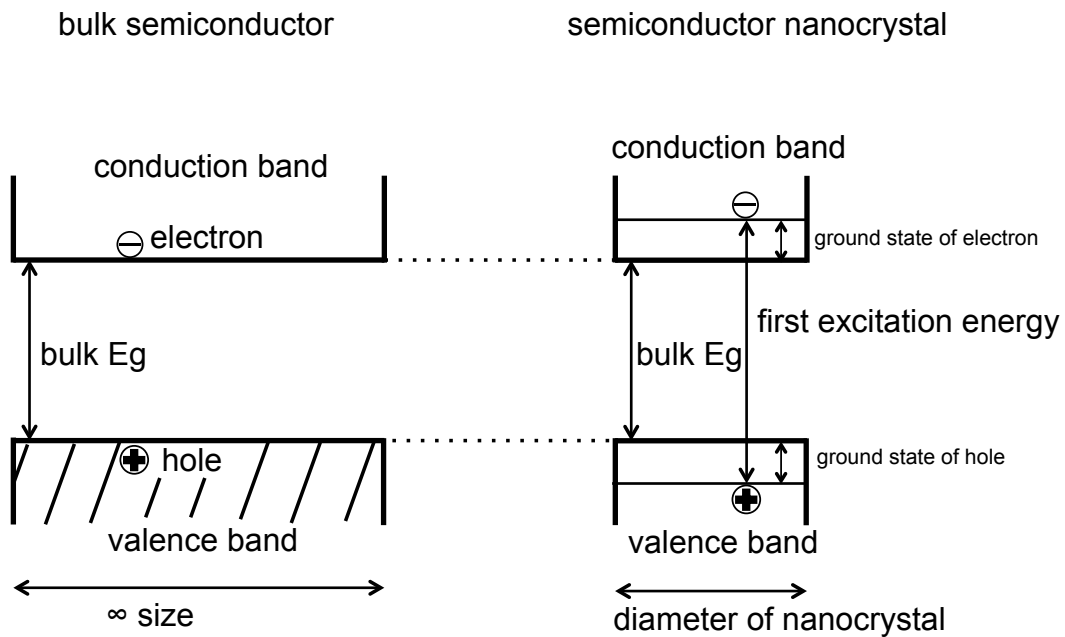
**Figure 1-2 Wavelength Tunable SPR of gold nanorods and silver nanoplate by varying the aspect ratios and edge lengths, respectively (a)** Transmission Electron Microscopy (TEM) images of different aspect ratios exhibiting different dimensions **(b)** in different color and **(c)** different SPR wavelength. **(d)** Photographs of Ag nanoplate solutions with varying edge length and **(e)** the corresponding extinction spectra, **(f)** TEM image of a typical Ag nanoplate, scale bar is 100 nm. (a) - (c) is from Ref. [15], (d) - (f) is from Ref. [14].

Due to the novel properties of noble metal NPs, there are multiple applications including catalysis [19], sensing [20], and optical signals enhancement of surface enhanced Raman scattering (SERS) [21], enhanced fluorescence [22], and light

absorption [23]. Controlled synthesis and manipulation of these NPs in terms of size, shape and homogeneity of the NPs ensemble thus become critical.

## 2.2 Semiconducting Nanoparticles

A semiconductor nanocrystal that is small enough to exhibit quantum confinement effects is called quantum dot. Quantum dots colloidal solutions were firstly discovered in 1983 [24], and have quickly emerged as key materials in nanoscience and technology, due to strongly size-dependent optical and electrical properties, which are important for both fundamental studies and device applications.



**Figure 1-3 Schematic spatial correlated electronic state diagram of bulk semiconducting material and the corresponding nanocrystal states.** The continuous conduction and valence energy bands of a bulk semiconductor are separated by a fixed energy gap,  $E_g$  (bulk), whereas a semiconductor nanocrystal has

a larger band gap dependent on diameter and quantized energy states, due to the quantum confinement.

In semiconducting materials, an electron in the valence band can be excited into the conduction band by absorbing a photon, and this leaves behind a hole in the valence band. The electron – hole pair is bound to each other via a Coulomb attractive force. The spatial separation between the electron and the hole is called the Bohr radius. In bulk semiconducting materials, the energy gap ( $E_g$ ) between the valence band and the conduction band is only dependent on the nature of the material. When the size of the semiconducting material is decreased down to the order of the Bohr radius, quantum effects play an important role, and the band gap becomes dependent on nanocrystal size. This can be pictured by simply adapting the particle-in-a-box model. As shown schematically in Figure 1-3, in bulk semiconductors, the electronic states in the conduction band and the valence band are continuous. The energy needed to excite the valence electron into the conduction band is fixed ( $E_g$ ), whereas in the semiconductor nanocrystal, the electron – hole pair is confined in a quantum well. Electronic states in the quantum well are quantized, as modeled by the particle in a box. The ground state energy of the electron and the hole in the rectangular potential well are:

$$E_e = \frac{\hbar^2 \pi^2}{8R^2 m_e^*} \quad \text{Eqn 1-3}$$

$$E_h = \frac{\hbar^2 \pi^2}{8R^2 m_h^*} \quad \text{Eqn 1-4}$$

where  $\hbar$  is the reduced Plank constant, R is the radius of the nanocrystal, and  $m_e^*$ ,  $m_h^*$  are the effective mass of the electron and the hole, respectively. Note that the electron and hole in a rectangular potential well has over simplified the actual spherical shape of the nanocrystal. A factor of 4 will be applied to the above equations to correct the effect of the spherically symmetric potential well, rather than a rectangular well. Additional energy is thus required to excite an electron from the valence band into the conduction band, forming an electron – hole pair, due to the quantum confinement effect. The summation of ground state energies of the electron and hole contributing the additional energy to the band gap energy is thus

$$E_{confinement} = \frac{\hbar^2 \pi^2}{2R^2 \mu} \quad \text{Eqn 1-5}$$

where  $\mu$  is the reduced effective mass of the electron and hole, and

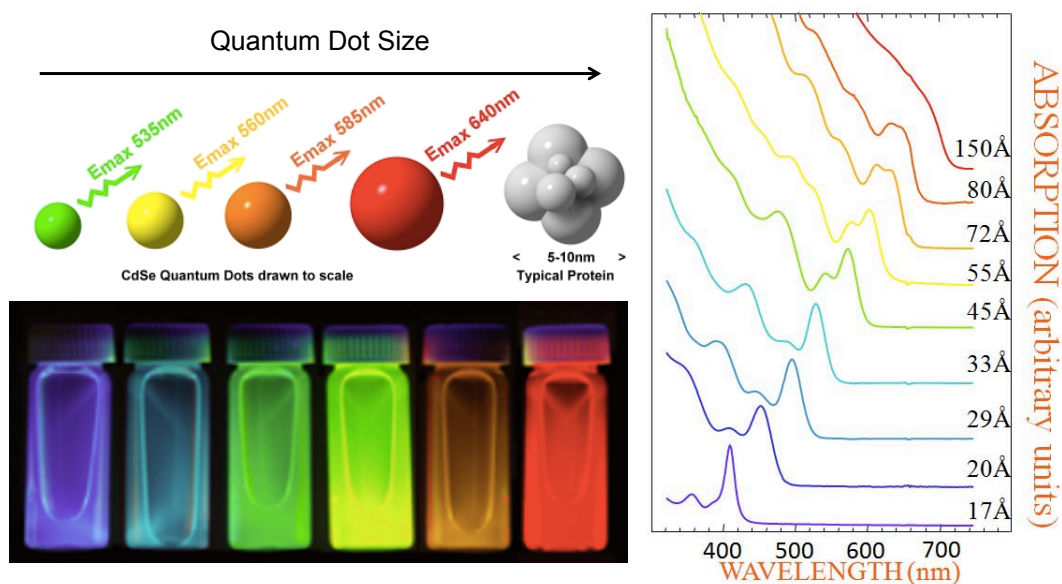
$$\frac{1}{\mu} = \frac{1}{m_e^*} + \frac{1}{m_h^*} \quad \text{Eqn 1-6}$$

Moreover, there is Coulomb attractive interaction between the negatively charged electron and the positively charged hole, and this part of the energy correction ( $E_c$ ) is in the order of  $\sim 1/R$  [25]. The overall band gap energy of the nanocrystal is thus

$$E_g = E_g(bulk) + \frac{\hbar^2 \pi^2}{2R^2 \mu} - E_c \quad \text{Eqn 1-7}$$

This enables semiconductor nanocrystals to possess tunable optical and electronic properties that strongly dependent on size. Among the various semiconducting materials, CdSe and CdS quantum dots are most extensively studied due to the band gap energy lying in the visible light range. For quantum dot colloidal solutions, size distribution is a key factor that allows precise tuning of the ensemble optical features.

The first successful synthesis of quantum dot colloidal solutions with narrow size distribution was realized in an organic liquid phase via high temperature decomposition of the organic precursor [26]. Figure 1-4 demonstrates the precise control of the band gap absorption and photoluminescence of the nearly monodispersed CdSe quantum dot ensembles in hexane. The band gap emission wavelength is tunable across the whole visible range with varying nanocrystal size.

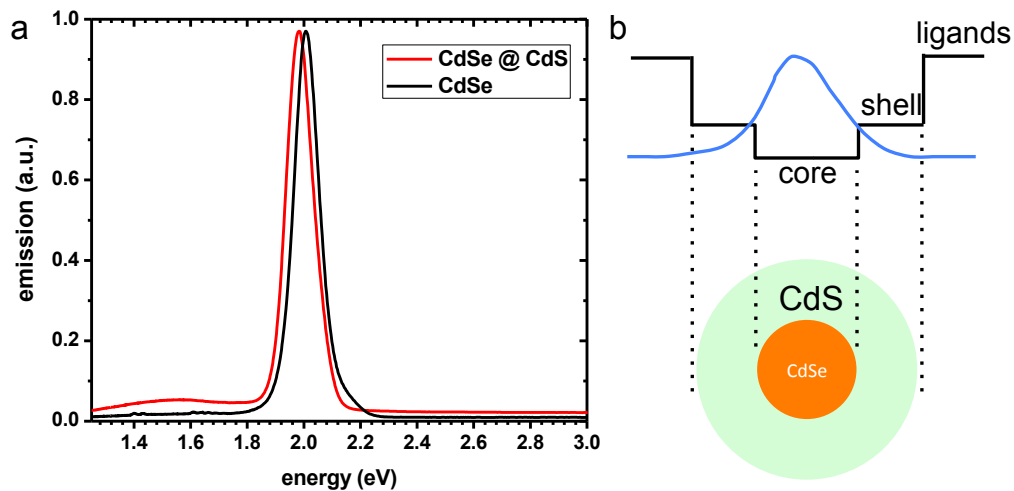


**Figure 1-4 Size dependent band gap engineering of colloidal CdSe quantum dots** (Left), colored fluorescent photographs of CdSe quantum dots colloidal dispersions in hexane and schematic models of quantum dots with varying size (Right), visible light absorption spectrums of the solution with different quantum dots size (from the website of Bawendi research group at the MIT, Department of Chemistry [27])

To date, other than spherical-shaped quantum dots, various anisotropically shaped semiconducting nanocrystals have been synthesized, including one-dimensional (1D)



nanowires, nanorods, 2D nanosheets, and tetrapods [28-32]. The band gaps of the 1D-confined sheets, 2D-confined wires, and 3D-confined quantum dots evolve differently with size [33]. For nanorods, the quantum confinement is intermediate between dots and wires, and the band gaps thus depend on both the diameter and the length [34]. What's more, the anisotropic morphology of rods and wires induces highly polarized optical and electrical properties [28, 35].



**Figure 1-5 Change in optical property of CdSe quantum dot after surface protection with a CdS shell.** (a) Normalized photoluminescence spectra of CdSe quantum dots before (black) and after (red) overgrowth of CdS shell (b) Schematic diagram showing the electronic state of a CdSe quantum dot with CdS shell protection surrounded by ligands (not shown in the cartoon). The 0.04 eV red shifting of the core @ shell is due to spreading of the wavefunction into the shell (blue) and the reduced kinetic energy of exciton.

Both size and shape greatly influence the properties of semiconducting nanocrystals. Beyond that, surface passivation and modification can play a critical

role, because the surface to volume ratio becomes significant when the particles size shrinks. Controlled surface passivation and surface stoichiometry of the component element can impact the photoluminescence property [36, 37]. Furthermore, forming a core @ shell structure is another way to protect the surface and alter the optical properties of quantum dots. For example, a CdSe core protected with a shell of wider band gap material (CdS or ZnS) via epitaxial growth shows an order of magnitude enhanced photoluminescence[38, 39], compared with plain CdSe dots. As depicted in Figure 1-5b, shell passivation forms an additional layer of the potential energy well, reducing the chance of electron and hole overlapping with the surface. Therefore, fluorescence efficiency will be enhanced with less influence of the surface defect states and trap sites. Also, the emission wavelength of core @ shell is red shifted compared with the plain core of comparable size (Figure 1-5a), due to spreading of the wavefunction into the shell and reduction of the kinetic energy of electron and hole. (Figure 1-5b, blue curve) To date, except for conformal spherical shell, rod-shaped and tetrapod CdS shells have been epitaxially grown on CdSe dots, with anisotropic optical emission [40-42]. These have stimulated exploitation of the material into functional device applications [43].

In addition, the composition of pseudobinary ( $AB_xC_{1-x}$ ) semiconductor alloy nanocrystals provides an additional degree of freedom to control the band gap and optical properties. In Chapter 3, an anisotropically shaped pseudobinary alloy semiconducting nanocrystal will be introduced and explored.

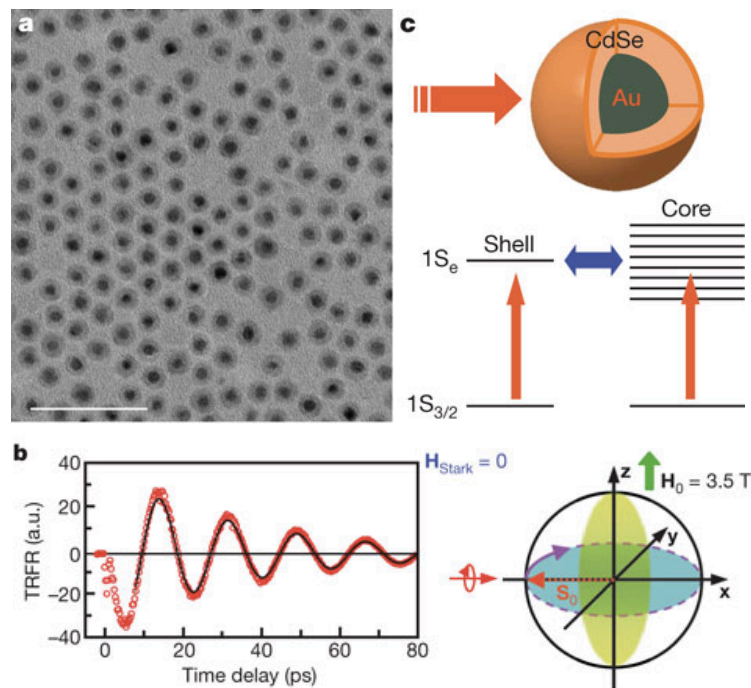
### 3. Hybrid Nanostructures

Building upon knowledge of noble metal and semiconducting NPs, researchers have further manipulated NPs into ordered building blocks (hybrid structures), with pre-designed geometry and NP components. This can provide additional opportunities to fine-tune nanostructure properties, probe fundamental inter-nanoparticle interactions, and enable technical applications. There are several comprehensive reviews of hybrid nanostructures [44, 45], written from the somewhat different perspectives of synthesis, properties and applications. In the following sections, I briefly review select motifs of plasmonic hybrid nanostructures that are representative of the field and most closely related to my Phd research.

#### 3.1 Plasmonic Hybrid Nanostructures with concentric core @ shell morphology

Core @ shell morphology architecture evolves with encapsulation of a nanoparticle in a uniform, concentric shell. One of a commonly studied plasmonic hybrid structure is the Au @ SiO<sub>2</sub> core @ shell via silica encapsulation [46]. Further incorporation of optically active species (dye molecules) can be realized via silica doping [47, 48] and surface functionalization [49]. The silica shell is an electric insulator with high-lying energy levels far from the plasmonic or molecular energy levels. The silica shell is thus free from charge transfer or Coulomb interaction with either the plasmon or dye. In addition, silica has a mesoporous structure that allows for dye molecule impregnation via surface adsorption and diffusion. The successful coating of a uniform silica shell on Au colloidal NPs [50] has enabled further research

to study the interaction between the plasmon and dye molecules in the near vicinity. Wiesner and coworkers [4] have demonstrated a lasing system with Au @ SiO<sub>2</sub> core @ shell nanostructures, in which dye molecules are doped throughout the shell. The stimulated emission in this colloidal nanoparticle is from surface plasmons, instead of the photons in a conventional laser. The dye molecules act as the energy source (gain medium) and couple to surface plasmons through a Forster resonance energy transfer process [51, 52]. This plasmon based laser could be used as a nanoscale quantum generator and ultrafast amplifier [53]. Bach and coworkers [49] used Au @ SiO<sub>2</sub> to systematically study distant dependent dye molecule fluorescence quenching by surface plasmons. In this system geometry, dye molecules are functionalized on the surface of the silica shell, and the silica shell acts as a spacer to enable fine-tuning of the molecule – plasmon distance. The complete transition from strong quenching to full recovery of the fluorescence was observed, signaling the energy transfer from the molecular emitters to the localized surface plasmon mode.



**Figure 1-6 Au @ CdSe core @ shell hybrid nanostructure integrates a surface plasmon of the Au core with an exciton of the monocrystalline CdSe shell. (a)** Typical large-scale TEM image showing uniform core @ shell nanostructures. The scale bar is 50 nm. **(c)** Schematic model showing transitions and resonant coupling (blue arrow) between core (continuum spectrum of plasmon) and shell (discrete interband exciton) in a core @ shell configuration under laser excitation (red arrows). **(b)** Time-resolved Faraday rotation (TRFR) experiment involving spin precession in the core @ shell hybrid nanostructures. (From Ref. [5])

Another interesting class of core @ shell nanostructure is built from metal @ semiconductor. This combination maximizes the plasmon and exciton coupling interaction. To overcome the synthetic difficulty of big lattice mismatch between semiconductor and gold, Ouyang and coworkers [54] have developed a robust, universal strategy, leading to nonepitaxially over growth of a monocrystalline conformal semiconductor shell on a spherical metal core (Figure 1-6a). The effort of developing the elegant nonepitaxial synthesis strategy is motivated by the intense interest of studying the plasmonic-exciton interaction. For 3 nm spherical Au NPs, the surface plasmon at 520 nm overlaps with the CdSe quantum dot first excited band gap transition energy. This makes it an ideal system to study the plasmonic-exciton resonance coupling, as schemed in Figure 1- 6c. In a follow up work by Ouyang and coworkers [5], the Optical Stark Effect (OSE) [55] was observed in the Au @ CdSe hybrid nanostructure. OSE is a fundamental light-matter interaction and typically observed as an energy level shift under exposure to intense optical irradiation. In another system without a plasmonic core (CdSe quantum dot), the light-matter

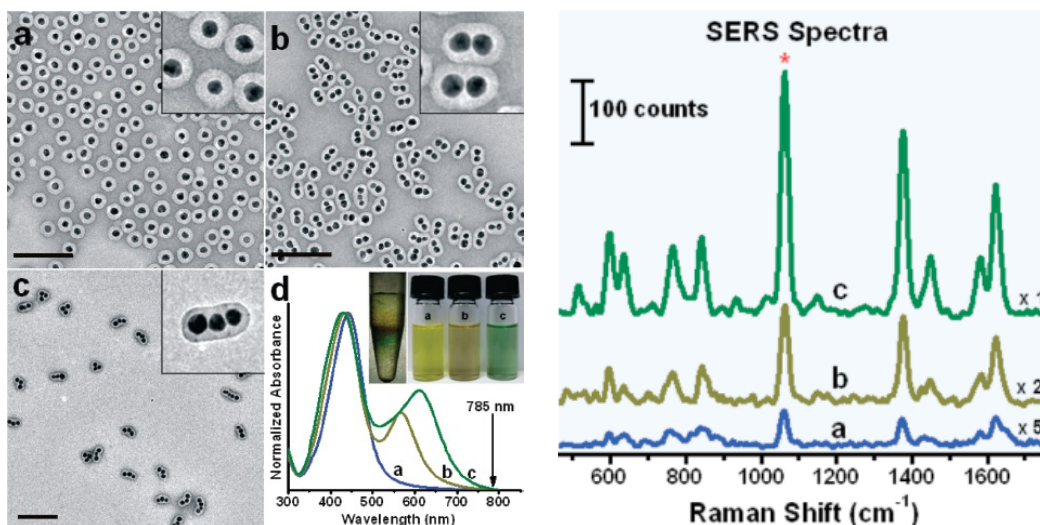
coupling is weakened in the nanoscale quantum dot colloid system. While in the Au @ CdSe hybrid nanostructure, OSE is enhanced by plasmon-exciton resonance coupling. The plasmonic core is used to concentrate the near field optical signal. The enhanced OSE signal is found to be strongly dependent on the polarization of the excitation light. This provides an internal tool to exert a light induced magnetic torque to manipulate the electron spin (Figure 1-6b). This work realized the first spin manipulation in a nanocolloid system, and demonstrated this class of hybrid nanostructures to be a candidate for quantum information and quantum computing [56].

New properties arise from reduced symmetry of anisotropically shaped Au NPs. This has motivated researchers to produce anisotropically shaped counterparts of the above structures. The nonepitaxial growth strategy actually has been adapted to synthesize anisotropically shaped monocrystalline metal @ semiconductor nanostructures. A detailed review of the synthetic methodology and perspectives will present in Chapter 2.

### 3.2 Plasmonic Hybrid Nanostructures with dumbbell morphology

Another category of hybrid nanostructure architecture is the dumbbell morphology. For noble metal nanostructures, new phenomena arise due to close proximity of multiple plasmonic NPs. Two effects occur when the plasmonic NPs are in proximity due to the plasmon coupling effect (1) a red shifting of the SPR [57], and

(2) local electric field enhancement at the gap between two NPs, i.e. “hot spot plasmon” formation. The hot spot plasmon has been widely applied to Raman signal enhancement known as SERS [58-61]. When the field enhancement is strong enough it has the sensitivity to detect the Raman scattering signal of a single molecule [60, 61]. The plasmon coupling effect is extremely sensitive to the inter-particle gap distance (surface-to-surface distance). Precisely control of the gap distance without fusing is not a straight forward task in colloid solution [61]. There are several strategies to combine noble metal NPs closely together and form dimers and trimers, with controllable inter-particle gaps, those including using complementary single strand DNA (ssDNA) [60, 62] and organic molecule linkers [63]. With ssDNA linkers, Alivisatos and coworkers [62] have synthesized Au – Ag heterodimers with inter-particles gaps tunable to the range of 3-8 nm. The plasmon coupling induced Ultraviolet–visible (UV-Vis) spectroscopy has shown a set of hybridized plasmon modes. In another work of Suh and coworkers [60], Ag has been progressively deposited onto ssDNA linked Au dimers and thus the inter-particle gap can be shortened from ~ 3.5 nm down to ~ 1.25 nm. Further thickening of the Ag shell has resulted in indiscernible (by TEM imaging) gap distance and a single molecule Raman signal has been detected. Ensemble effects, particularly when samples include NPs with large variations in gap distance, can obscure targeted plasmonic features. Consequently, these dumbbell studies have generally been performed as single nanoparticles measurements.



**Figure 1-7 Purified plasmonic monomers, dimers and trimers (a-c)** TEM images of monomers, dimers and trimers, respectively. Scale bars are 200 nm (d) UV-Vis spectra of structure enriched colloidal solution correspond to a (blue), b (yellow) and c (green); Inset shows photographs of the solutions after density gradient centrifugation, where monomers, dimers, and trimers were enriched in distinct yellow, brown, and green bands, respectively. The different surface enhanced Raman factors of the corresponding structures are shown in the right panel. (From Ref. [59])

Along these lines, Chen and coworkers in Singapore have demonstrated a simple and clever approach to assemble Ag NPs into ultra-short dimers and trimers through introducing colloid aggregation in ensemble solution followed by polymer encapsulation [64]. Coupled with a post-purification via density gradient ultracentrifugation, they successfully obtained highly purified plasmonic monomers, dimers and trimers encapsulated in a polymer shell (Figure 1-7 a-c), with 0.8 nm uniform inter-particle gap distance. The monomers, dimers and trimers exhibit different optical features characterized by UV-Vis spectroscopy, shown in Figure 1-



7d. Dimers and trimers have an additional plasmon mode arising from the dipole – dipole coupling between the individual Ag NPs. The local electric field is enhanced at inter-particle gaps within the dimers and the trimers, and SERS signal is determined to be enhanced by factors of 16 and 87, respectively, in comparison with the monomers. This well controlled plasmonic NPs assembly has allowed ensemble measurement with unambiguous calculation and interpretation of the SERS enhancement properties [59].

## Chapter 2: Monocrystalline Nonepitaxial Metal @ Semiconducting Hybrid Nanostructure: Synthesis, Challenges and Prospects

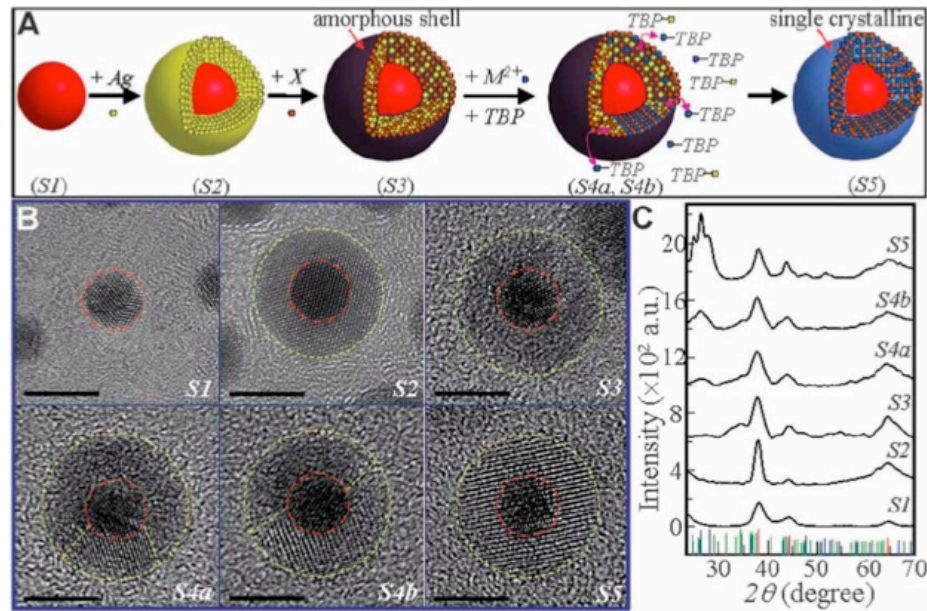
### 1. Introduction

Both metal nanoparticles (NPs) and semiconducting quantum dots have been intensively studied by researchers and emerged as key materials in today's nanoscience and technology [65, 66]. Metal NPs have prominent optical properties with controllable absorption and scattering resonances originating from the surface plasmon resonance (SPR), while semiconducting quantum dots possess engineered electronic band gap structures that give rise to finely tunable optical properties. Recently, a new class of nanomaterial, which integrates metal and semiconducting material into a discrete nanoscale building block, has attracted attention as a promising route to multi-functional properties for targeted application in electronics [67, 68], photocatalysis [69, 70] and spintronics [5]. Such hybrid building blocks introduce new and attractive properties due to the coupling between the dielectric-confined electromagnetic resonance in the metal segment and the quantum-confined electronic states in the semiconductor one [71]. In principle, the plasmon-exciton interaction within the metal-semiconducting hybrid nanostructure permits exquisite control of the nanoscale energy transfer path, yielding tunable absorption and

emission properties. In practice, the availability of high quality metal-semiconductor hybrid nanostructure remains a hurdle for this field.

Fabrication of metal-semiconducting hybrid nanostructures with high morphology and crystallinity control is challenging due to the large lattice mismatch between the two distinct materials. For dissimilar materials prepared according to well established epitaxial growth methods [72, 73], the lattice mismatch between metallic and semiconductor materials generally leads to the formation of grain boundaries within the semiconducting block [67], as well as defects and strong interfacial lattice strain [74]. However, growth of defect-free single-crystalline semiconductor based hybrid nanostructures is highly desired to support high performance devices. Recently, Ouyang and coworkers [54] developed a delicate and versatile non-epitaxial growth process to fabricate spherical core @ shell metal @ semiconducting colloidal NPs down to 10 nm size, with perfect single-crystalline semiconducting shells, as shown in Figure 2-1. This method also offered remarkable control over the nanostructure ensemble in terms of size, uniformity and gradient of both core and shell. The essence of the preparation is to first synthesize the  $M_1 @ Ag$  bimetallic ( $M_1=Au, Pt, FePt$ ) spherical core @ shell; and subsequently chemically convert into  $M_1 @ Ag_2X$  ( $X=S, Se, Te$ ) by controlled reaction with selected chalcogenide precursors. The final step involves cation exchange with the desired metal ions ( $M_2$ ) to create  $M_1 @ M_2X$  ( $M_2=Cd, Pb, Zn$ ). Hybrid nanostructures synthesis by this non-epitaxial method has successfully overcome the big lattice mismatch problem of two distant materials components, permitting studies of plasmon-exciton coupling in monocrystalline Au

@ CdSe core @ shell hybrid nanostructures. Already this unique nanostructure has been harnessed for studies of the plasmon enhanced optical stark effect (OSE) [5]. This work provided an elegant demonstration of light-matter-spin interactions through plasmon-exciton resonant coupling in a colloidal nanoparticle system.



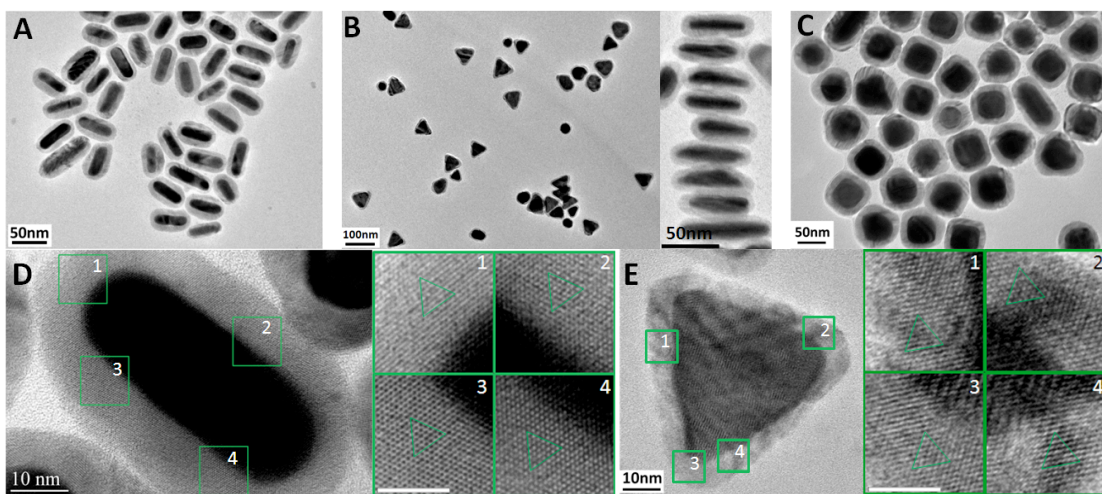
**Figure 2-1** Nonepitaxial growth of *isotropic* monocrystalline Au @ semiconducting core @ shells hybrid nanostructure (A) Schematic illustration of the synthesis procedure (Scheme 1). X: chalcogenide precursor;  $M^{2+}$ : Metal ion including  $Cd^{2+}$ ,  $Pb^{2+}$ , and  $Zn^{2+}$ ; and TBP: tributylphosphine (B) High-resolution Transmission electron microscopy (TEM) images showing the product of the corresponding S1-S5 steps. Scale bars are 5 nm. (C) X-ray Diffraction characterization of the nanostructure of the five stages. From Ref [54]. Reprinted with permission from AAAS.

The multifunctional properties of non-epitaxial metal @ semiconducting hybrid nanostructures become even more apparent upon moving beyond core @ shell

structures to nanostructure varieties with defined anisotropic shapes. The reduced symmetry of anisotropically shaped plasmonic NPs introduces additional plasmon modes associated with the corresponding collective electron oscillation. For example, a rod shaped gold nanoparticle has a longitudinal plasmon mode oscillating along the long-axis direction, with a rod-length dependent tunable resonance of 600 nm to NIR wavelength [15]. Moreover, the local electric field enhanced by the plasmon resonance of the longitudinal mode is highly polarized along the long-axis. These attractive optical properties enable tailored plasmon-exciton interaction in a more precise manner, and are of particular interest for applications such as photocatalysis and functional optoelectronic devices. Following the original report of the nonepitaxial synthesis method, Ouyang and coworkers further improved the synthetic methods and adapted the technique to produce various anisotropically shaped monocrystalline metal @ semiconducting hybrid nanostructures, from conformal and non-conformal core @ shell of cubic, triangular plate, rod to large aspect ratio nanowire up to micron-meter scale [75]. The synthetic route achieved both well-defined anisotropic shape and perfect monocrystallinity throughout the whole semiconducting shell (Figure 2-2) with independent control of the two chemical ingredients. Improvements in the chemical synthesis of these materials are elaborated in the section below.

Additionally, Wang *et al.* have adapted the nonepitaxial synthetic method for spherical hybrid nanostructures to fabricate anisotropically shaped Au @ semiconducting hybrid nanostructures [76]. In this work, sulfur powder was used as

the S precursor to achieve a rod shaped Au @ CdSe core @ shell with controllable shell thickness. A longitudinal plasmon enhanced two-photon luminescence under near-infrared laser excitation was thereby demonstrated. Wang *et al.* further reported a strong plasmon-exciton interaction characterized by a sign-reversed and magnitude-enhanced absorption feature in the same system [77]. Cubic-shaped Au @ AgCdS hybrid core @ shell structures were similarly pursued via this method, resulting in incomplete cation exchange [78]. Alternatively, Su *et al.* used a one-pot hydrothermal method to make closed-shelled Au @ CdS and Au @ ZnS hybrid nanostructures, with rod-shaped cores and shells with flower-like outer shell edge [79]. The process involves direct over growth of either CdS or ZnS shells on rod-shaped Au cores, using transition metal thiobenzoate complexes as the metal sulfide precursor in the presence of Ag<sup>+</sup>. The formation mechanism is attributed to a nonepitaxial process, initialized by the formation of a Ag<sub>2</sub>S wetting layer, followed by cation exchange with Cd (II) or Zn (II).



**Figure 2-2 Low-resolution TEM images of different anisotropically shaped Au @ CdS core @ shell nanostructures showing the overall distribution and**

**morphologies (A) Rod (B) Triangular plate**, right inset shows the cross section of the plate, and **(C) Cubic shape**; and high-resolution TEM images of a single anisotropic Au @ CdS monocrystalline nanostructure of **(D) rod shape, (E) triangular plate**, showing the monocrystallinity throughout the whole structure. In each images of **(D)** and **(E)** four areas outlined in green are enlarged and highlighted to the right, showing the identical lattice orientations (green triangles). Scale bars of insets are 5 nm.

Reports of anisotropic  $M_1 @ M_2X$  plasmonic @ semiconducting hybrid nanostructures demonstrate the challenges to achieve single crystalline semiconducting shell with precision anisotropic shapes. Without rigorous understanding and control of experimental protocols, hybrid nanostructures can become polycrystalline and exhibit irregular edges in the semiconducting shell. Nonetheless, such hybrid nanostructures already demonstrate strong plasmon- exciton coupling, and pose considerable opportunities for further tailoring. Realizing these opportunities requires detailed consideration of the stepped synthetic process. Each step involves a subtle chemistry that must be optimized in order to achieve precision of the final hybrid nanostructure product. Moreover, some shape anisotropies are particularly challenging. In this chapter, we will review and discuss in detail the methodology of nonepitaxial  $M_1 @ M_2X$  synthesis, presenting challenges and prospects.

## 2. Methodology of Synthesis

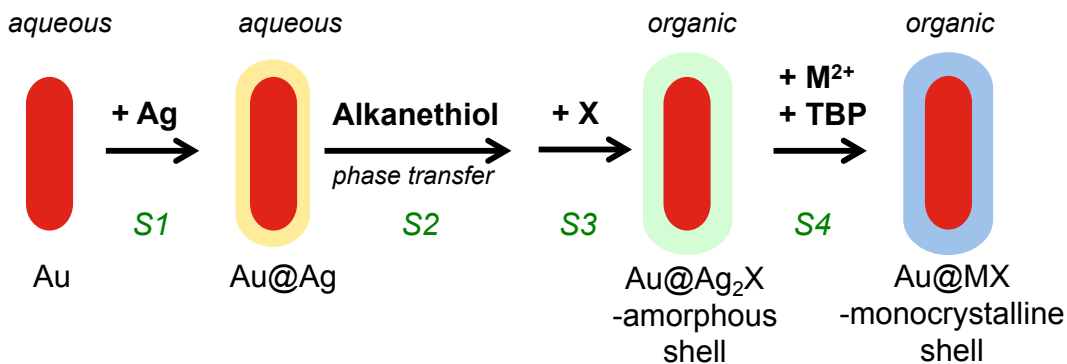
### 2.1 Overview of the Methodology

*Isotropic Hybrid Nanostructures:* Nonepitaxial growth of hybrid nanostructures involves multiple solution chemistry steps, as shown schematically in Figure 2-1 for the simplest case involving an isotropic core @ shell structure. The route starts from a monodispersed ensemble of Au NPs in toluene solution. (S1), followed by overgrowth of a uniform Ag shell around the Au NP core (Au @ Ag NPs, S2). The Ag shell is next reacted with a chalcogenide precursor (X), forming an amorphous Ag<sub>2</sub>X shell (S3). Finally, the Au @ Ag<sub>2</sub>X is chemically converted to Au @ MX (M=Cd, Pb, Zn) via cation exchange [80] (S4-S5). Remarkably, after replacement of Ag<sup>+</sup> with the desired ions, a continuous, uniform monocrystalline semiconducting shell forms around the core. The formation of an amorphous Ag<sub>2</sub>X shell is a key step that leads ultimately, but counter-intuitively, to a single crystal MX shell. This is because the amorphous Ag<sub>2</sub>X matrix facilitates the motion of the ions, as well as the growth of the monocrystalline MX domain, due to a reduced interfacial and grain boundary energies between amorphous Ag<sub>2</sub>X and crystalline MX [81]. For spherical metal @ semiconducting hybrid nanostructure, the entire process is conducted in a *uniform dispersed organic* colloidal solution.

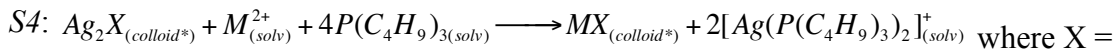
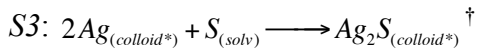
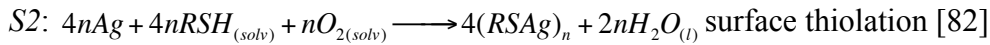
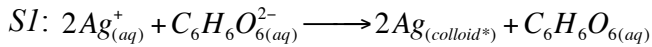
*Anisotropic Hybrid Nanostructures:* The production of hybrid nanostructures with anisotropic shapes requires phase transfer from aqueous to organic solution via ligand exchange. This is because as-made Au @ Ag is originally achieved in aqueous solution. More importantly, the additional ligand exchange steps are needed to



preserve the created anisotropic morphologies during subsequent reaction with the chalcogenide precursor. As shown for a rod-shaped hybrid nanostructure in Figure 2-3, 1-decanethiol ( $-SH$ ) was used to bind tightly onto the Ag surface and replace the cetyltrimethylammonium bromide (CTAB) surfactant in aqueous solution. Then the  $-SH$  capped Au @ Ag NPs are phase transferred into a toluene-acetone mixture, where they react with a chalcogenide precursor. Due to the strong binding between  $-SH$  and Ag, the kinetics of chalcogenation reaction can be well regulated appropriately such that the anisotropic shape feature of shell is well maintained, since a too intense reaction can result in change of surface morphology of  $Ag_2S$  and even lost the original anisotropic shape. Preparation of anisotropic metal @ semiconducting hybrid NPs following these protocols can preserve the original bimetallic shape, enabling versatile shape control of the final product regarding both core and shell. Following the identical protocols, this method has been extended to additional anisotropic shapes, including triangular plate and cubic shapes, with sharp edges and exposed facets. The shape preservation of rods with dome-capped ends is readily achievable, while preservation of sharp edges (facets) present additional challenges, discussed in the section below.



**Figure 2-3 Schematic illustration of a precision synthetic route to achieve anisotropic monocrystalline Au @ semiconducting core @ shells hybrid nanostructure (Scheme 2).** In contrast to spherical synthesis in scheme 1, additional steps involving ligand exchange with alkanethiol and phase transfer are required. X: chalcogenide precursor;  $M^{2+}$ : Metal ion including  $Cd^{2+}$ ,  $Pb^{2+}$ , and  $Zn^{2+}$ ; and TBP: tributylphosphine. The reaction steps are labeled in green as *S1* through *S4*. The overall chemical reaction can be described by the following equations:



S, Se

\* core@shell colloid with a Au core

† Net observable reaction; S is presumably in situ generated by organosulfur precursor.

Figures 2-1, 2-2 demonstrate the synthetic approach of generating high quality monocrystalline hybrid nanostructures. A key goal is to make the approach more robust so that the synthesis is scalable and highly selective of the targeted structure. Starting from core material with high purity and narrow size distribution, each chemical step requires careful optimization. There are specific challenges in each step of nanostructure synthesis, due to the dual need to preserve morphology and achieve monocrystallinity. These step-wise methods and challenges are reviewed below.

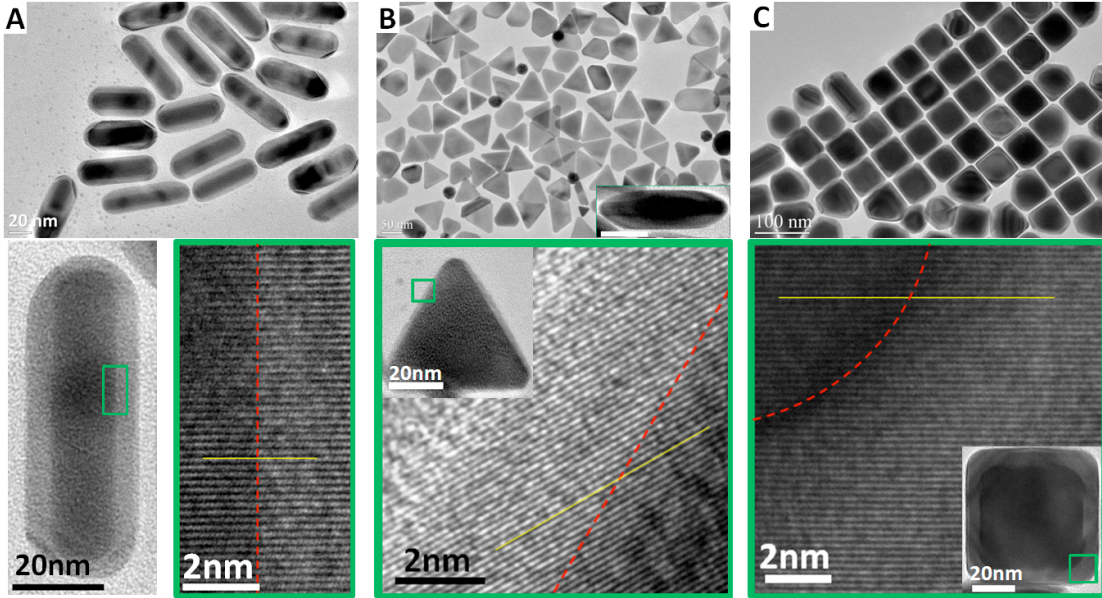
## 2.2 Step 1. Au @ Ag and Effect of Ag shell thickness

The Ag shell serves as the starting template to be converted to the semiconducting shell with conformal shape and uniform thickness. The choice of silver for the template is based on two considerations. (1) As shown in Figure 2-4, silver has a 0.2 % near lattice-match to gold, facilitating epitaxial over growth on gold NPs to produce a conformal shell; (2) silver has more reactivity with the chalcogenide precursors than the core gold material, allowing for silver-to-semiconductor chemical conversion, while keeping the plasmonic gold core intact. For both isotropic and anisotropic shape Au @ Ag core @ shells, control over the initial NPs ensemble distribution in terms of silver shell thickness and morphology, as well as suppressing silver self-nucleation, is prerequisite for subsequent chemical transformation. Precise and independent control of the dimension of the metal core and the semiconducting shell is important for it provides the basis for tunable optical features. Consequently, methods for the strict control of Ag shell thickness during the first step of hybrid nanostructure synthesis have been developed. Coating of a conformal Ag shell on the spherical Au core is achieved by thermal reduction of silver (I) by oleylamine in toluene under mild temperature. Typically, as-made oleylamine capped monodispersed Au NPs were re-dispersed into 8 ml toluene and 0.2 ml oleylamine in a small vial. The silver (I) is introduced by adding 2 ml of freshly prepared Ag<sup>+</sup>-methanol solution (10 mg of silver nitrate in 2 ml methanol) into the Au NP toluene solution. The reaction vial is merged in 35 °C oil bath overnight without agitation. The shell thickness can be precisely controlled by adjusting the reaction time and

temperature. For all the anisotropic conformal Au @ Ag materials prepared, procedures were inspired by a method previously reported for the production of Au @ Ag triangular nanoplates [83]. Briefly, Au NPs in as-made shapes are first washed and re-dispersed into 1.5 mL 0.05 M CTAB aqueous solution, followed by sequential addition of 0.2 mL 0.1 M ascorbic acid, 40  $\mu$ L 0.01 M AgNO<sub>3</sub> and 0.3 mL 0.1 M NaOH aqueous solution with mixing thoroughly. Reduction of Ag<sup>+</sup> by ascorbic acid in the presence of base occurs spontaneously, yielding a uniform conformal Ag shell with a typical thickness of ca. 3 nm. Thickening of the Ag shell can be realized by repeatedly conducting the above process. The successive coating of silver by the addition of small aliquot, rather than a one-time coating with large amount of silver precursor, yields a superior control over the shape replication of the template core.

The shell thickness of best quality of the Au @ semiconducting product generally falls within a certain range. The ideal range of shell thickness is really depending on the shape and dimension of the core. Take the rod shaped NPs as an example, when reacted with the chalcogenide precursor, a too thick (> ca. 10 nm) Ag shell leads to overall elliptic feature of shape due to rounding corners of Ag<sub>2</sub>X. We note that careful control of the reaction rate with chalcogenide precursor is particularly needed to prevent core from etching with a thick shell. At the other extreme, a too thin (< ca. 2 nm) Ag shell often results in fusion of different rods through the CdS layer after cation exchange for chemical conversion [77]. Also, a too thin shell results in a multicrystalline semiconducting shell instead of the targeted monocryatlline shell, after cation exchange. Figure 2-4 shows TEM images of three different shaped Au @

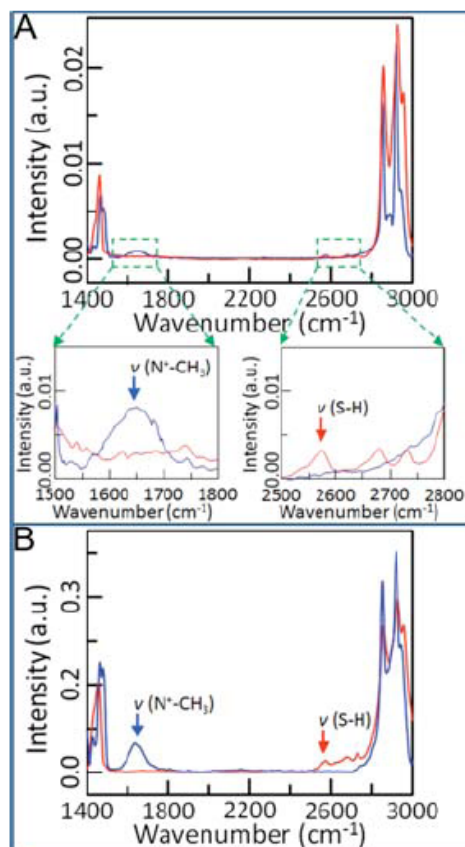
Ag NPs where the Au @ CdS was convert from. After three cycles of silver coating on each sample, the thickness (~6 nm) is within the ideal range to best maintain the quality of the Au @ CdS hybrid NPs.



**Figure 2-4 TEM characterization of the Au @ Ag core @ shell nanostructures where the Au @ CdS was convert from.** (A) nanorods. **(Top)** large scale TEM image, scale bar is 50 nm. **(Bottom-left)** TEM image of a single nanorod, **(Bottom-right)** high resolution TEM image of the green outlined area in **(bottom-left)** nanorod. **(B)** triangular plates. **(Top)** large scale TEM image, scale bar is 50 nm. Inset shows a typical TEM image of a cross-section Au @ Ag triangular plate. Scale bar is 20 nm. **(Bottom)** a single triangular plate and its high resolution TEM image of the green outlined area. **(C)** nanocube. **(Top)** large scale TEM image, scale bar is 100 nm. **(Bottom)** a single nanocube and its high resolution TEM image of the green outlined area. For eye guidance, red dash lines in each high resolution image distinguish the Au-Ag interface. Yellow lines show the uniform lattice orientation across the Au-Ag interface, revealing nature of epitaxial crystalline growth process.

### 2.3 Step 2. Ligand Exchange and Effect of Alkanethiol on Shape Regulation

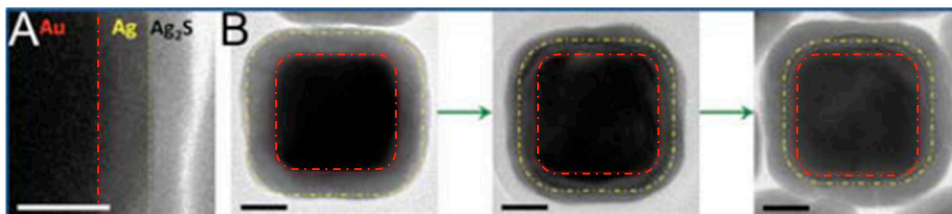
For anisotropic nanostructure synthesis, preservation of anisotropic shapes with inhomogeneous surface curvature is a great challenge. Sharp geometric features on the exposed surface tend to be unstable, and can spontaneously evolve into rounded “edges” with lower surface energies [84, 85]. In order to retain the anisotropic shell morphology during the subsequent chemical transformation, the as-made Au @ Ag surface with well-defined anisotropic shape is chemically passivated with alkanethiol. The alkanethiol (typically dodecanethiol C<sub>10</sub>H<sub>22</sub>S) strongly binds to Ag, forming robust interfacial thio-metal bonds on shell surface. As the Au @ Ag is originally capped by CTAB as grown in water, ligand exchange by alkanethiol can be done by simply re-dispersing Au @ Ag to 10 % (v/v) alkanethiol acetone solution, followed by mild sonication and centrifugation. Such alkanethiol capped Au @ Ag can be then transferred to organic phase and well dispersed into toluene and acetone mixed solution (with addition of alkanethiol to suppress ligand loss on re-dispersion). Successful ligand exchange and alkanethiol capping can be confirmed by Fourier Transform Infrared Spectroscopy (FTIR) (Figure 2-5).



**Figure 2-5 Surface passivation of Au @ Ag nanorod core @ shell by dodecanethiol** The Au @ Ag nanorods were originally capped with CTAB surfactants as synthesized. **(A)** FTIR spectra of Au @ Ag core @ shell nanorods before **(blue)** and after **(red)** ligand exchange with C<sub>10</sub>H<sub>22</sub>S molecules. For clarity and comparison, two energy regimes are further highlighted to show spectra characteristics of CTAB and C<sub>10</sub>H<sub>22</sub>S molecules, respectively. Peaks are assigned by comparing with molecular spectra as well as with literature results [86-88] **(B)** FTIR spectra of pure CTAB and pure C<sub>10</sub>H<sub>22</sub>S molecular films on ZnSe windows.

Surface passivation with alkenethiol ligands on Au @ Ag plays a key role in shape preservation during the subsequent formation of the Ag<sub>2</sub>X shell (Scheme 2, S3). Control experiments have been done to clearly revealed the key roles of alkanethiol: (1) Reaction of Ag shell with the S precursor in the absence of alkanethiol surface passivation leads to irregular morphology of Ag<sub>2</sub>S shell with etched Au core, due to

immediate and intense reaction between the bimetallic NP and the S precursor; (2) Time dependent experiments indicated that alkanethiol passivation onto the Ag surface allows regulation of the reaction rate, which has led to homogeneous reaction between Ag and the S precursor over the whole shell (Figure 2-6). Such regulation is important for preserving morphology and preventing the occurrence of localized reaction zones on the NP's [89] during the reaction.



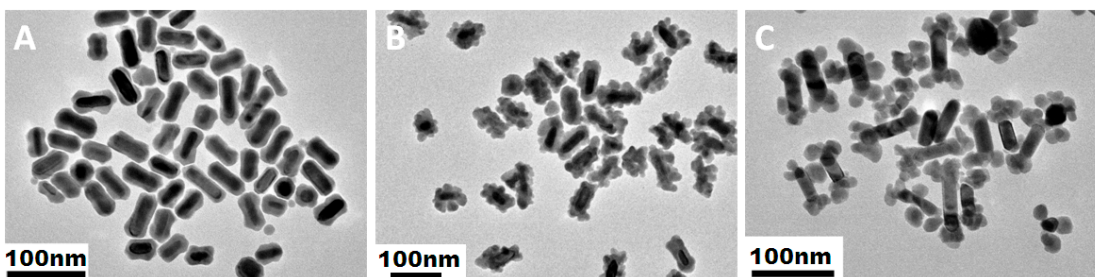
**Figure 2-6 Time-evolution of reaction between Ag shell and S precursor under surface passivation with C<sub>10</sub>H<sub>22</sub>S molecules (A)** TEM image highlighting different image contrast among Au, Ag and amorphous Ag<sub>2</sub>S, which has allowed us to distinguish and monitor reaction zone when Ag shell reacts with S-precursor. Scale bar is 10nm. **(B)** TEM images showing evolution of Ag-Ag<sub>2</sub>S boundary (yellow dashed line) with time. Red dashed lines represents Au-Ag interface. Scale bar is 20 nm.

#### 2.4 Step 3. Chalcogenation and amorphization of Ag shell: Chalcogenide Precursor and Morphology Control

Chemical conversion from Au @ Ag to monocrystalline Au @ MX starts with the reaction of the Ag shell with the chalcogenide precursor to form the amorphous Ag<sub>2</sub>X shell matrix. This is the key step of the overall nonepitaxial method. Both the crystallinity and morphology of Ag<sub>2</sub>S is highly upon on the reaction kinetics between the Ag and the chalcogenide precursor, so the selection of precursor is very crucial. In



the original work, the organic based sulfuric precursor was prepared by dissolving 2 mmol sulfur powder into a mixture of 5 ml oleylamine and 10 ml oleic acid in 100 °C oil bath for 40 min with constant stirring, forming a highly viscous, clear, bright orange homogenous solution. In the mixture sulfur reacts with oleylamine likely forming a mixture of complexes including alkylammonium polysulfides, thioamide and byproducts [90]. The resulting sulfuric-precursor(s) react well with the Au @ Ag particles to generate amorphized and conformal Ag<sub>2</sub>S shells on both spherical and anisotropic particles. Trials of all other forms of sulfuric- precursors (such as sulfur powder, dimethyl sulfoxide, NaHS, etc) generally result in the formation of a multicrystalline Ag<sub>2</sub>S shell and change in shell morphology. For aggressive reactants (e.g. sulfur powder), the Ag shell can be fully or partially peeled off from the Au core.



**Figure 2-7** Different morphology of Au @ Ag<sub>2</sub>Se rod with a relative smooth surface shape (A), a flower-like surface shape (B), and bone shape (C). The morphology difference is due to the reaction with different batch of selenium precursor.

We next discuss shape preservation in the formation of Au @ Ag<sub>2</sub>Se hybrid nanostructures. Analogous to the S precursor above, the Se precursor is prepared by mixing 0.5 mmol Se powder, 5 ml oleic acid and 2.5 ml oleylamine in 180 °C oil bath

for 19 hours with constant stirring. Dissolution of Se powder into oleic acid and oleylamine makes a very dark red viscous solution. However, even following extended reaction time and temperature relative to S precursor preparation, selenium reacts incompletely, leaving a black solid precipitate. After the reaction, the product is added with 7.5 ml toluene to decrease the viscosity and then is centrifuged in order to separate the unreacted selenium powder, as well as any white selenium oxide solid. Evidently, selenium does not react with oleic acid / oleylamine to the extent that sulfur does. Preparation of the selenium precursor is thus not as well controlled and as concentrated under parallel experiments to that of sulfur. As shown in Figure 2-7, three motifs of Ag<sub>2</sub>Se surface morphology were observed by using different batch of Se precursor reacting with rod shaped Au @ Ag core @ shell NPs. The Au @ Ag<sub>2</sub>Se rod in Figure 2-7A depicts the amorphous Ag<sub>2</sub>Se shell with a relatively smooth surface morphology around the rod shaped core, indicating the reaction proceeded in relatively homogenous manner. The anisotropically shaped Ag shell converts to amorphous Ag<sub>2</sub>Se with original shape, accompanied with volume expansion due to the insertion of Se<sup>2-</sup> ions. However, the poorly controlled selenium precursor makes it difficult to control this reaction. As shown in Figure 2-7B, a Ag<sub>2</sub>Se shell consisting of multicrystalline domains forming flower-like closed shell was readily generated. Finally, Figure 2-7C shows bone shaped Au @ Ag-Ag<sub>2</sub>Se morphology, where there are spherical single crystalline Ag<sub>2</sub>Se domains only on the tips of the rod. Herein, the reaction between Ag and selenium occurs preferentially on the tips of the rod. This suggests stronger binding of alkanethiol on the cylindrical sidewalls and weaker binding on the tip facets of rod shaped Au @ Ag. We rationalize these observations

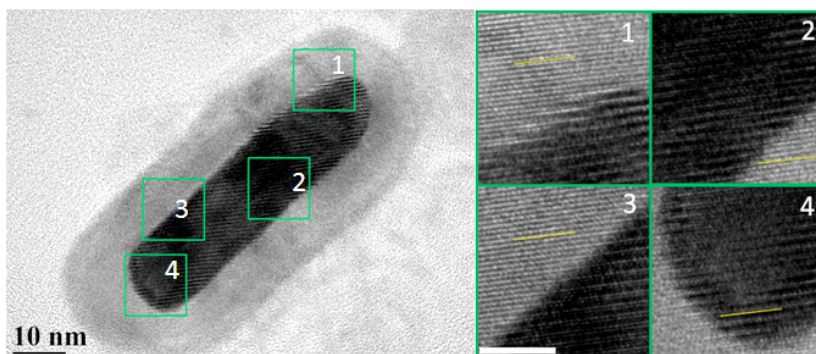
by considering the strength of the binding of the Se precursor with Ag (I). The binding must be sufficiently weak to maintain amorphous  $\text{Ag}_2\text{Se}$  matrix, and must compete with the alkanethiol ligand to regulate the surface morphology. At present, refinement and improved reproducibility in the development of Se precursors are needed for generation of precision  $\text{Au} @ \text{Ag}_2\text{Se}$  hybrid nanostructures.

#### 2.5 Step 4. Cation Exchange to Produce Monocrystalline Shell

The last step to realize the chemical transformation is to convert  $\text{Au} @ \text{Ag}_2\text{X}$  to  $\text{Au} @ \text{MX}$  via cation exchange, a process that can preserve the morphology of the initial nanostructure template upon exchange and enable the formation of new material with versatile composition [91]. To insure completed conversion from  $\text{Ag}_2\text{X}$  to  $\text{MX}$ , tributylphosphine (TBP) is used to extract  $\text{Ag}^+$  from the nanocrystal to facilitate  $\text{MX}$  grain growth. Importantly, cation exchange from amorphous  $\text{Ag}_2\text{X}$  leads to a monocrystalline  $\text{MX}$  shell with independent lattice orientation with respect to the core material. For 10 nm outer-shell spherical  $\text{Au} @ \text{Ag}_2\text{X}$ , cation exchange is presumed to initiate and propagate from a single nucleation site, accounting for the formation of a monocrystalline shell. However, targeted anisotropic nanostructures have much larger dimensions up to 100 nm. For such cases, single site nucleation and propagation might not be applicable. Thus, additional reaction kinetic control may be needed to facilitate formation of monocrystalline semiconducting shell. In practice, the formation of polycrystalline shells in as-grown nanostructure is commonly observed in larger anisotropic NPs. However, repeatedly refluxing of  $\text{Au} @ \text{Ag}_2\text{S}$  with alkanethiol efficiently promotes formation of monocrystalline semiconductor

shell after cation exchange with metal ion. Single crystalline domain growth can thus be thermally activated in this regime through the simple refluxing protocol.

On the other hand, addition of oleylamine molecules greatly enhances the formation of polycrystalline semiconductor shell. This suggests that surface passivation of the  $\text{Ag}_2\text{S}$  regulates the kinetics of cation exchange, and the subsequent grain crystallization-and-growth process. Studies indicate that surface passivation with alkanethiol can efficiently inhibit cation exchange nucleation, while introduction of oleylamine molecules can facilitate ion diffusions and cation exchange through outward surface of amorphous  $\text{Ag}_2\text{S}$  matrix. Therefore, an appropriate combination of alkanethiol and oleylamine must be applied to regulate the number of initiated nuclei in a large scale of amorphous  $\text{Ag}_2\text{S}$  matrix. It is also found that with high density of alkanethiol capping on the  $\text{Ag}_2\text{S}$  surface, spontaneous nanocrystalline  $\text{CdS}$  nucleation occurs every ca.  $0.5 \mu\text{m}$  at the initial stage of cation exchange process. Monocrystalline shells produced larger than this scale are dominated by a mechanically driven grain growth process [75].



**Figure 2-8 High-resolution TEM images of a single Au @ PbS rod, showing the monocrystallinity throughout the whole structure. Four areas outlined in green are**

enlarged and highlighted to the right, showing the identical lattice orientations (yellow lines). Scale bars of the insets are 5 nm.

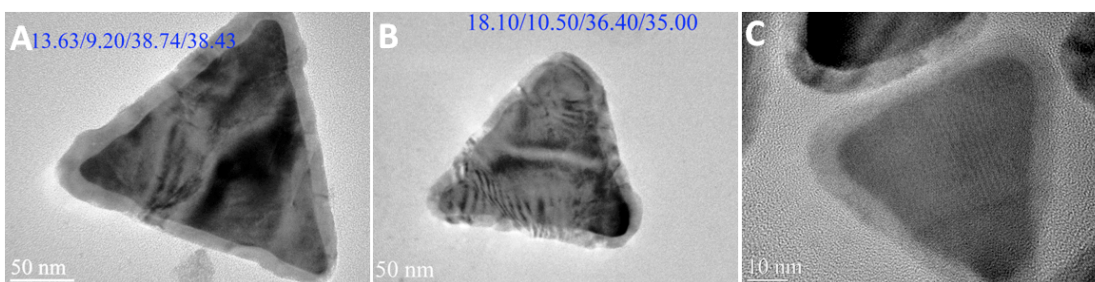
Additional factors regulating the cation exchange kinetics include temperature, concentration of TBP, and identity of the metal ions to be exchanged. It is found that the reaction temperature up to 60 °C to 90 °C to be the optimal to produce high quality monocrystalline semiconducting shell. Higher temperature can accelerate the full exchange, at the expense of converting the amorphous  $\text{Ag}_2\text{X}$  matrix into a multicrystalline semiconducting shell. TBP has the effect of donating its lone electron pair of P to  $\text{Ag}^+$ , forming a stable coordinate complex thus facilitates the exchange with the desired metal ions. Unfortunately, the lone pair is also sensitive to oxygen in the air, forming tributylphosphine oxide. Thus, air-free operation is usually required when handling TBP. Cation identity is an important factor. The cation exchange method is versatile and amenable to different desired metal ions. Yet different cations encounter different exchange challenges, requiring adjustment of the synthesis condition to ensure monocrystalline of final products. To introduce the metal ions into the reaction mixture, the metal salts are dissolved in methanol and added into the toluene solution of the NPs. The solubility of the metal ions in methanol differs from each other and this limits the quantity of Au @ MS produced at a time. Additionally,  $\text{Pb}^{2+}$  forms coordination complex with oleylamine ( $\text{Pb}^{2+}$ -oleylamine) and this makes the replacement of  $\text{Pb}^{2+}$  by  $\text{Ag}^+$  harder. To overcome these difficulties, repeatedly refluxing of the Au @  $\text{Ag}_2\text{S}$  intermediate product with alkanethiol to replace oleylamine ligands is especially necessary to produce high quality monocrystalline

PbS shell (Figure 2-8). For producing ZnX semiconducting shell,  $Zn^{2+}$  is the hardest Lewis acid among  $Cd^{2+}$ ,  $Pb^{2+}$ ,  $Ag^+$  and  $Hg^{2+}$ , thus has the least binding strength with TBP and the exchange with  $Ag^+$  become the most spontaneous. This makes the ZnX nuclei easily forms on multiple sites during cation exchange, resulting in multicrystalline shell.

### 3. Shape Considerations: Size Scaling

To date, different range of size of the hybrid nanostructure has been explored. For the case of spherical core @ shell particles, precision structures have been realized with outer diameters up to 35 nm and semiconducting shell thickness of 15 nm. For various anisotropic shapes, yet larger structures have been realized. Precision cubes with core edge length of 50 nm have been attained. Rods with varying aspect ratios from 1:2 (20 nm × 40 nm) to 1:5 (15 nm × 75 nm) have been realized. Wires have reached up to 3.3 μm length with 30 nm Au core diameter [75]; and for triangular plate, different edge sized structure - from 50 nm to 200 nm, have ben produced, as shown in Figure 2-9. When the size of anisotropic nanostructure scales up with nonepitaxial synthesis method, it is not surprising that new structural features can emerge. For example, large aspect ratio (20-100) nanowire assume curvature, and bent over the length-axis, due to the mechanical force during the monocrystalline growth of semiconducting shell [75]. What's more, larger sized triangular plates adopt a wrinkled morphology, as manifested by shape distortion in TEM images (Figure 2-9A, B). The wrinkle feature forms during the cation exchange process. Due

to reduced dimension in thickness of the triangular plate, the core is likely bent by mechanical force of monocrystalline CdS grain growth. For smaller sized anisotropic nanostructure, it is more challenging to preserve the sharp feature of the core, where the plasmonic material has its function of local field enhancement rely on. As shown in Figure 2-9 B and C, smaller triangular plate has less degree of distortion compare to the larger one, but exhibits more notable rounding corner of the core.



**Figure 2-9 Au @ CdS triangular plate of different edge size (A) 200 nm, (B) 150 nm, and (C) 50 nm. The blue numbers on the images are the element molar ratio of Au/Ag/Cd/S.**

#### 4. Remaining Challenges

The general method for producing metal @ semiconducting hybrid nanostructures has been developed, however, the variation of the reaction kinetics with respect to nanostructure morphology, requires the optimization of processing conditions for each starting material. To date, there are a few different monocrystalline hybrid nanostructures consisting of combinations of materials that have been explored with various shapes, as summarized in Table 2-1. Synthesis of hybrid nanostructures of Au @ CdS and Au @ PbS have been studied most extensively, while reported work on

Au @ ZnS, and Au @ CdTe limited to spherical structures. Further efforts and attempts are needed before this chart is expanded.


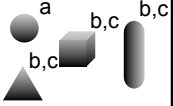
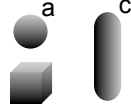
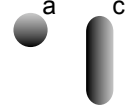

The kinetics of the synthetic protocol precludes its applicability to HgX. The binding strength of  $\text{Hg}^{2+}$  with TBP is comparable as  $\text{Ag}^+$  does with TBP thus cation exchange of  $\text{Hg}^{2+}$  with  $\text{Ag}^+$  will not occur. An interesting question is the extension to other core materials. To date Au has been the primary core in these model studies, primarily because of its attractive plasmonic properties. In addition, other spherical core materials including platinum and  $\text{Fe}_{0.5}\text{Pt}_{0.5}$  NPs have also been demonstrated (Science). In practical, obtaining the starting core NPs ensemble with narrow distribution in terms of size and morphology is a challenging, and this is especially the case for certain anisotropic NPs such as Au cubes. Triangular plate is grown in an ensemble mixture of plates and spheres and it requires preliminary purification before silver coating. Moreover, the feasibility of Ag shell coating is another difficulty to overcome when considering using varieties of core material. For example,  $\text{Fe}_{0.5}\text{Pt}_{0.5}$  @ CdS nanowire would be a very interesting hybrid nanostructure to study the effect of ferromagnetism on spin polarization of the semiconducting nanowire. However, uniform coating of Ag on the entire  $\text{Fe}_{0.5}\text{Pt}_{0.5}$  slim wire remains challenging. Attempts of several strategies of Ag coating have resulted in silver over growth only at two ends of the wire.

Also, as discussed above, the reaction between the Ag shell with the chalcogenide precursor is the key step of the nonepitaxial method. Synthesis of the amorphous



Ag<sub>2</sub>S shell is experimentally well developed, yet Ag<sub>2</sub>Se remains a challenging, as the reproducibility of a selenium precursor that leads to amorphous Ag<sub>2</sub>Se shell with well-controlled morphology needs to be improved in order to make the chemistry robust. This is more problematic for the larger dimensional anisotropic nanostructure than spherical one. What's more, tellurium does not dissolve at all following the precursor preparation of sulfur and selenium. The development of other chemical forms of chalcogenide precursor is needed to address this limitation.

**Table 2-1 Summary of monocrystalline Au @ semiconducting hybrid nanostructures with various morphologies prepared via nonepitaxial method.**

	Zn <sup>2+</sup>	Cd <sup>2+</sup>	Pb <sup>2+</sup>
S <sup>2-</sup>			
Se <sup>2-</sup>			
Te <sup>2-</sup>			

a. Ref. [54]

b. Ref. [75]

c. Huizhi Bai, original result.

## 5. Conclusion and Prospects

The class of metal @ semiconducting core @ shell hybrid nanostructure has been synthesized with remarkable monocrystalline and morphology control by nonepitaxial method. This new material exhibits attracting optical properties due to strong plasmon-exciton coupling between the core and the shell, and has potential application in electronics, photocatalysis and spintronics. Promising improvements have been made to allow flexible combinations of both core and shell in terms of chemical ingredient, size and morphology. At this stage, spherical and rod shaped nanostructure is ready for scaling up synthesis, while cubes and triangular plates may require more stringent refinement of experimental protocols of the starting material synthesis. Furthermore, improvement and searching other possibilities of Se and Te precursor would open up more choices to material diversity and allow engineered optical properties. One aspect of the materials that is not well understood involves the metal-semiconductor interface. Given the lattice mismatch of the core-shell materials, one might expect the prevalence of defects or reconstruction at the immediate interface. A recent study using transient absorption spectroscopy has shown fewer defects in the Au-CdS interface due to the nonepitaxial nature [92]. In contrast of metal-semiconductor interface by epitaxial growth method showing defects due to lattice strain, non-radiative energy loss in the nonepitaxial grown spherical Au @ CdS nanostructure is significantly reduced due to fewer defect scattering. Compared with the thermal reduction grown Au-CdS heterostructure, charge transfer into metal domain of the nonepitaxial structure is relatively slow and this leads to longer exciton lifetime, implication of the existence of a higher potential barrier at the Au-CdS

interface. The nonepitaxial semiconductor lattice seems decoupled with the core shown by both high-resolution TEM characterization and transient optical spectroscopy. Gaining more knowledge of the interface is an important and challenging area for future study.

## Chapter 3: Anisotropically Shaped $\text{CdS}_x\text{Se}_{1-x}$ Pseudobinary Semiconductor Nanocrystals <sup>1</sup>

### 1. Introduction

Semiconductor nanocrystals have been extensively studied over the past decade due to their unique electronic and optical properties [65], which largely depend on size, shape, and chemical composition. It is well known that band gap engineering of semiconductor nanocrystals can be realized by fine tuning the dimension due to quantum confinement on the nanoscale [93]. In addition, nanocrystal shape is another key property that has led to a broad range of device functionality [94]. Changes in nanocrystal shape modify the band structure and attendant optical and electronic properties. In contrast to nonpolarized fluorescence from spherical semiconductor nanocrystals, rod-shaped semiconductor nanocrystals emit polarized fluorescence along the length-axis [95]. These properties offer new opportunities for improved performance in devices that include semiconductor-nanorod lasers [96], nanorod-based solar cells [97, 98], and nanoscale transistors from a single cadmium selenide ( $\text{CdSe}$ ) tripod [99] and tetrapod [100]. Over recent years, the controlled synthesis of semiconductor nanocrystals in organic colloidal solution has been extensively studied [101]. Nonetheless, robust synthetic routes to tailor nanocrystal shape and the elucidation of growth mechanisms remain important issues in nanomaterial

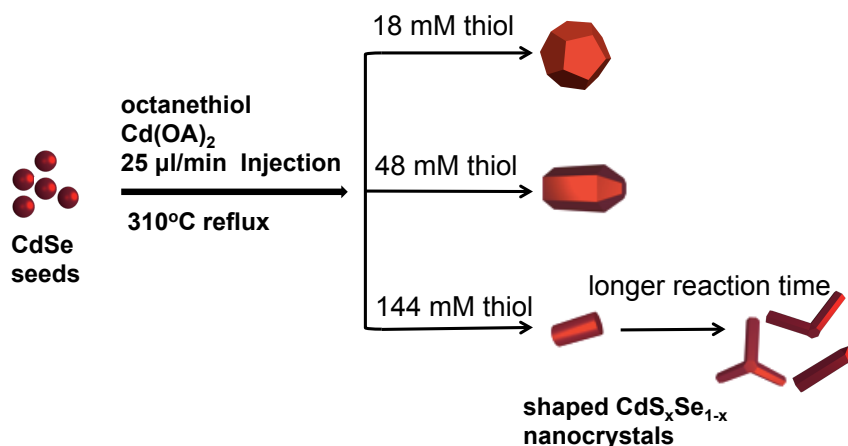
---

<sup>1</sup> This work is lead by Huizhi with collaboration of Joshua Taillon and Dr. Lourdes Salamanca-Riba. Huizhi synthesized all the nanocrystal and performed all the TEM and spectroscopy characterization. Joshua Taillon conducted the EDS mapping characterization, with advice of Dr. Lourdes Salamanca-Riba.

chemistry. Various anisotropically shaped semiconductor nanocrystals have been synthesized, including highly faceted cubes, tetrahedrons [102], and quasi two-dimensional platelets [103]. These anisotropically shaped semiconductor nanocrystals typically adopt the zinc blende or wurtzite crystal structure. The wurtzite-structured nanocrystal presents additional categories of anisotropic shape, such as the rod and bullet [29, 104]. Interestingly, a polycrystalline tetrapod [32] has also been synthesized with four wurtzite arms growing from a zinc blende seed. So far, all of these anisotropically shaped semiconductor nanocrystals were synthesized with uniform chemical composition (AB). On the other hand, pseudobinary ( $AB_xC_{1-x}$ ) semiconductor alloy nanocrystals can provide an additional degree of freedom (beyond size and shape) to control the band gap properties. To date, synthesis of semiconductor alloy nanocrystals has been limited to sub-10 nm homogeneous [105] and gradient [106] alloy spherical structures [107-109], while synthesis of *anisotropically shaped* alloys has gone unreported. In this work, we present a synthetic route to  $CdS_xSe_{1-x}$  alloy semiconducting nanocrystals with various anisotropic shapes through seed-mediated growth.

As shown in Figure 3-1, our synthetic route starts from 4 nm zinc blende spherical CdSe nanocrystals which function as seeds in the colloidal solution. Cadmium oleate and octanethiol are slowly injected into the reaction solution via a syringe pump at rate of 25  $\mu$ l/min, while the reaction solution is ramped up to the temperature of 310 °C. (See the experimental section for detailed procedure.) After sufficient reaction time (order of 100 min), larger anisotropically shaped  $CdS_xSe_{1-x}$  alloy

semiconducting nanocrystals form. By varying the concentration of the octanethiol solution injected and the growth time, we achieve relatively uniform ensembles of nanocrystal with select shapes, including polygons, bullets, and rods. Rod-shaped nanocrystals can further develop into a mixture of bipods, tripods, and tetrapods with longer reaction times. This work achieved the first anisotropically shaped pseudobinary ( $AB_xC_{1-x}$ ) semiconductor alloy nanocrystals with a seed-mediated growth method, selectively achieving a variety of shapes.



**Figure 3-1 Synthetic route to various anisotropically shaped  $CdS_xSe_{1-x}$**

**nanocrystals from zinc blende spherical CdSe seeds.** By varying the concentration of octanethiol solution injected and the growth time, pure ensembles of nanocrystals in different anisotropic shapes can be obtained, including polygons, bullets, and rods. A mixed ensemble of bipods, tripods, and tetrapods is obtained with longer reaction time.

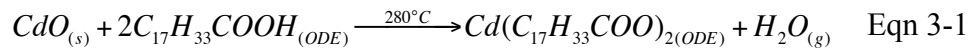
Using rod-shaped anisotropic nanocrystals as a model system, we further demonstrate that the size and chemical composition (S : Se ratio) can be fine tuned co-dependently through the reaction time. This further permitted optical

measurements on a series of rod-shaped CdS<sub>x</sub>Se<sub>1-x</sub> nanocrystals. The band gap of semiconducting nanorods were found to be altered by the gradient element distribution of S and Se within the length-axis direction of the rods. Finally, a set of control experiments (without cadmium precursor) were conducted to explore the mechanisms that lead to the formation of shaped alloy nanocrystals. Octanethiol is found to act as both sulfide precursor and shape-directing reagent, with rod-shaped nanocrystals evolving into multi-pods ensemble at late growth stages.

## 2. Experimental Methods

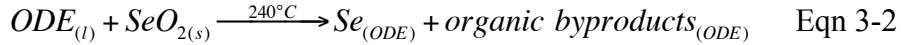
### 2.1 Preparation of 4.5 nm spherical zinc blende CdSe seeds

Zinc blende CdSe seeds are synthesized with modification of a published method [110]. First, cadmium oleate precursor was prepared by mixing 1 mmol cadmium oxide (CdO), 10 ml octadecene (C<sub>18</sub>H<sub>36</sub>, ODE) and 1.87 ml oleic acid (OA) in a 250 ml three neck-flask flushed by nitrogen (N<sub>2</sub>) gas for 30 min. Then the mixture was heated to 280 °C under N<sub>2</sub> gas protection to allow full reaction between CdO and OA to produce a clear solution, upon which the reaction was stopped and cooled to room temperature. The production of cadmium oleate precursor is described by the reaction equation:



To the above clear cadmium oleate solution, 1 mmol selenium dioxide (SeO<sub>2</sub>) and 63 ml ODE were added. After flushing by N<sub>2</sub> for 30 min, the solution was heated to 240 °C and subsequently maintained for 1 min before 1 ml OA was added dropwise

under N<sub>2</sub> protection. During the process the solution became yellow, orange and then red. Then, the solution was held at 240 °C for another 30 min, after which the heater was removed and the solution returned to room temperature. During the process SeO<sub>2</sub> powder was dissolved in ODE forming clear solution. The reaction between ODE and SeO<sub>2</sub> is described as follows [110]:



Subsequent dissolution of selenium in ODE or oleylamine-forming organoselenium species can yield multiple byproducts [111]. In the reaction equation below, Se then reacts with cadmium oleate and ODE to form CdSe colloid.

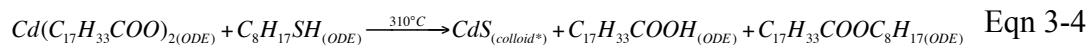


The product was precipitated and washed by adding propanol or anhydrate acetone with centrifugation at 6500 rpm for 20 min, and re-dispersed into ~ 15 ml hexane for further usage. This quantum dot ensemble has a first band gap absorption peak at 583 nm and fluorescence emission at 617 nm, as measured by UV-Vis absorption spectroscopy and fluorescence spectroscopy, respectively. The concentration of the 15 ml solution was calibrated according to the absorption peak at 583 nm. A 1 : 5 hexane dilution should have an intensity of 0.988 at 583 nm absorption peak with 2 mm optical path.

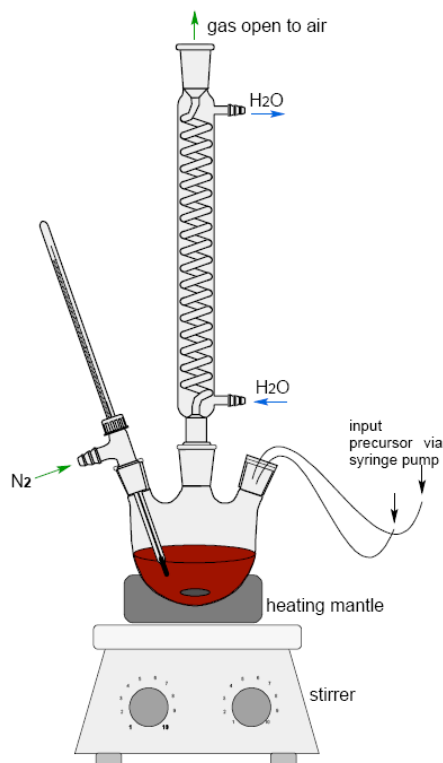
## 2.2 General procedure to synthesize shaped CdS<sub>x</sub>Se<sub>1-x</sub> alloy nanocrystals

Shaped CdS<sub>x</sub>Se<sub>1-x</sub> alloy nanocrystals were synthesized by adaptation of a previously published procedure [112]. The reaction between cadmium oleate and octanethiol is proposed to be:





\*Nucleate on CdSe seed



The experimental set up is shown in Figure 3-2 and detailed steps are described as follows.

- i. Combine 1.5 ml oleylamine and 1.5 ml ODE in a 100 ml three-neck bottle.
- ii. Take 1 ml CdSe hexane stock solution and combine with the solution of step 1, stirring 1 min to mix thoroughly.
- iii. Pump the mixture of step 2 with a vacuum pump at room temperature for 1.5 hours to remove hexane.
- iv. Take 1.2 ml cadmium oleate precursor prepared by the above method (1 mmol in 10 ml ODE) with a biotech pipette, and dilute with ODE up to 6 ml, then load into a 6 ml plastic syringe. The final concentration of cadmium oleate is 20 mM.
- v. In the glove box, take 1.5 mL octanethiol and add 4.5 ml ODE to make a sulfuric precursor stock solution. Dilute the stock solution 10 times by withdrawing 0.6 ml with a 1 ml syringe and adding ODE up to 6 ml. Load the diluted solution into a 6 ml syringe. The final concentration of octanethiol is 144 mM.

- vi. Transfer the 3-neck bottle of the step 3 mixture above a heating mantle. Set up a condenser, a thermometer, and a two-port syringe pump on the three-neck bottle following Figure 3-2. Note that this synthesis process was conducted with flowing N<sub>2</sub> gas, with a positive N<sub>2</sub> pressure (15 - 30 PSI) and N<sub>2</sub> directly exhausted to atmosphere from the top of the condenser. The reaction mixture was degassed with N<sub>2</sub> for 1 hour at room temperature, and then heated to 120 °C and held for 20 min, and then the temperature was quickly raised to 310 °C with the maximum heating power. Once temperature reached 280 °C, the syringe pump was started to inject the precursor of cadmium oleate and octanethiol, as prepared in steps 4 and 5. The syringe pump was set up with two 6 ml syringes injecting simultaneously, 3.0 ml total deliver volume at a 1.5 ml/hr rate of delivery.
- vii. After ~ 2 min of the precursor injection, the temperature reached 310 °C and the solvent started to boil throughout. At the end the precursor injection, 0.5 ml OA was quickly injected to the solution by penetrating a syringe needle through the rubber stopper and the solution was maintained at 310 °C for an additional hour before cooled to room temperature.
- viii. To remove the un-reacted precursors and wash the sample, anhydrate acetone was added to the cooled solution until white cloudy precipitation occurred. (The amount of anhydrate acetone addition depended on size of the nanocrystal product). The product was centrifuged at 3500 rpm for 15 min. The nanocrystals were then dispersed into hexane. Repeat the washing procedure three times to obtain a better-cleaned nanocrystal sample.

**Table 3-1 Reaction conditions for different anisotropically shaped semiconducting nanocrystal products and compositions (based on 4.5 nm CdSe spherical seeds)**

shape	Octanethiol Concentration (mM)	Reaction Time (min)	$x=S/(S+Se)$
polygon	18	180	0.63
bullet (2:3 aspect ratio)	48	180	0.68
bullet (1:1 aspect ratio)	96	180	0.69
rod (varying size)	144	12-104	varying
rod and mixed bi-, tri- pods	144, 192	120	0.73

The above procedure was used to synthesize a mixture of bi-pods, tri-pods and tetra-pods. By changing the octanethiol concentration prepared in step 5 and the total reaction time, different shapes of nanocrystals were produced (see Table 3-1). For rod-shaped nanocrystals, control experiments were conducted with fixed 144 mM octanethiol concentration and varied reaction time (Time zero was defined as when the reaction mixture reached 280 °C.) Multiple reaction ports permitted sample collection at different reaction times. To stop the reaction, the solution was extracted with a long needled glass syringe and injected in cold acetone in a separate vial, without addition of OA.

## 2.3 Characterization

### *Transmission Electron Microscopy Characterization (TEM):*

Transmission Electron Microscopy images were obtained using a JEOL model JEM 2100 LaB<sub>6</sub> microscope at an acceleration voltage of 200 kV. The specimens were prepared by adding a drop of hexane dispersion onto an amorphous carbon-coated 300 mesh copper grid and drying in air.

### *Energy-Dispersive X-ray Spectroscopy (EDS) mapping and High-angle Annular Dark Field Scanning Transmission Electron Microscopy (HAADF STEM)*

#### *Characterization:*

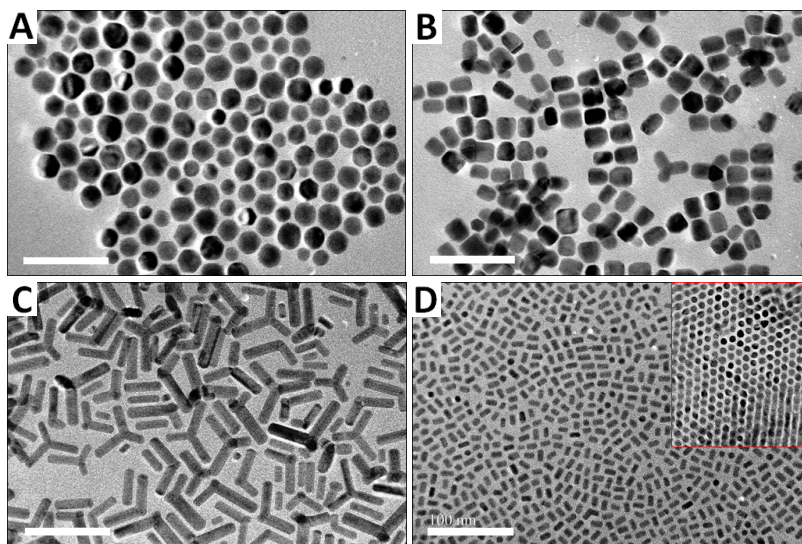
EDS area maps, line scans and HAADF images were obtained using a JEOL JEM 2100F field-emission transmission electron microscope equipped with an ultra-high resolution pole piece and an Oxford 6498 INCA X-sight EDS system with polymer window (energy resolution of 136 eV at the Mn-K $\alpha$  line). The microscope was operated in scanning TEM (STEM) mode, allowing for precise analytical information to be obtained from a focused probe. Due to the tendency for hydrocarbon contamination buildup under the electron beam (from the hexane dispersion), a relatively large probe size of approximately 1 nm was used, together with a fast scanning rate (0.5 s dwell time for area maps and approximately 1 s for line scans) and a process time of 5 in the Oxford INCA EDS software. For each map (or line scan), repeated passes were collected until suitable statistics had been obtained. HAADF-STEM images were recorded at the same beam settings, with a camera length of 8 cm.

*Photoluminescence (PL) measurement:*

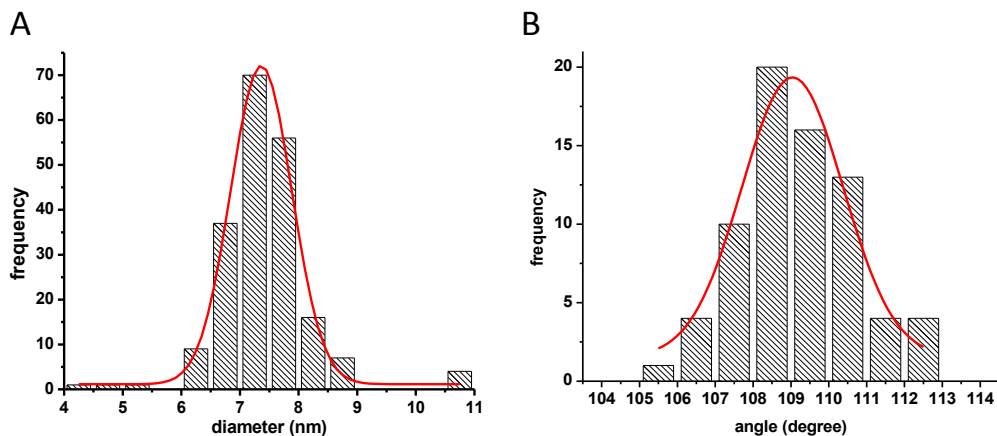
The ensemble photoluminescence measurement is conducted using a portable USB fluorescence spectrometer by Ocean Optics™. The hexane colloidal solution was placed in a 2 mm quartz cuvette supported on a 10 mm sample holder across the diagonal direction to make a  $\sim 90^\circ$  optical path. The sample was radiated with a 400 nm blue laser and the luminescence was monitored from 350 nm to 1100 nm.

### 3. Results and Discussion

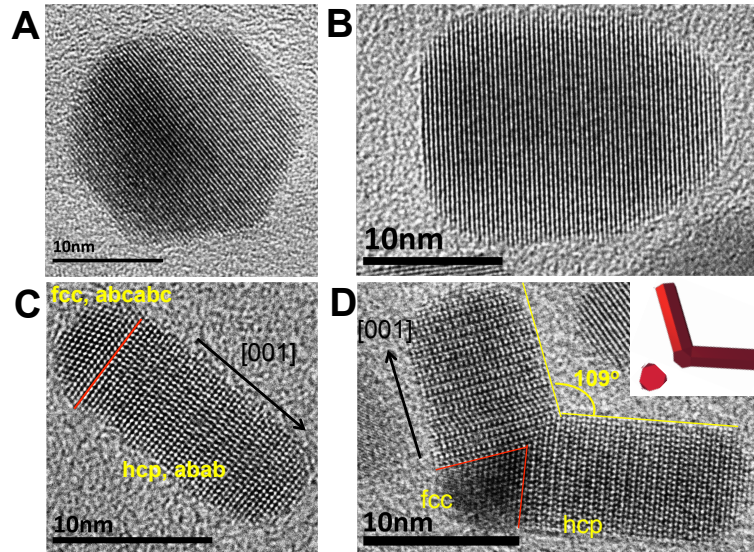
The low-resolution TEM images of various anisotropically shaped semiconductor nanocrystals are shown in Figure 3-3. Four ensembles of nanocrystals with different morphologies are discovered with the experimental condition explored; polygon, bullet, rod, and mixture of bi-pods, tri-pods and tetra-pods. High-resolution TEM images shown in Figure 3-5 better reveal the morphology of each ensemble structure. According to the low-resolution TEM images, the rod ensemble is the most uniform in shape manifestation and size distribution, as shown in Figure 3-3D. The self-assembly of nanorods with its length-axis perpendicular to the TEM grid (Figure 3-3D inset) confirms the narrow size distribution of the rod diameter. A histogram of rod diameters according to the assembly image reveals the mean diameter is  $7.4 \pm 1.0$  nm. (Figure 3-4A)



**Figure 3-3** Low-resolution TEM images showing different shapes of  $\text{CdS}_x\text{Se}_{1-x}$  semiconducting nanocrystals prepared under different reaction conditions. **(A)** polygons synthesized with 18 mM initial thiol injection; **(B)** bullets, 48 mM initial thiol injection; **(C)** mixture of bi-pods, tri-pods and tetra-pods with 144 mM thiol injection, and **(D)** rods synthesized with 144 mM thiol injection. The inset is the TEM image of a rod-shaped nanocrystal assembly with its length-axis perpendicular to the TEM grid. Scale bars are 100 nm for all images. The S composition for each sample from A to D is 63 %, 67 %, 73 %, and 68 %, respectively.



**Figure 3-4 (A) Histogram of rod diameter** and a Gaussian fit (red line) revealing mean diameter is  $7.4 \pm 1.0$  nm. **(B) Histogram of joint angle of the bi-pods** and its Gaussian fit (red line) showing the  $109 \pm 3^\circ$  angle.



**Figure 3-5 High-resolution TEM images of differently shaped semiconducting nanocrystals:** (A) polygon, (B) bullet, (C) rod, and (D) bi-pods with a zinc blend seed at the joint of two wurtzite arms. Inset of (D) shows physical models of a truncated tetrahedron seed and the developed bi-pods from the seed model.

High-resolution TEM characterization provided further details of the crystalline structure. The polygon- and bullet-shaped structures (in Figure 3-5 A, B ) are single crystalline, while rod (Figure 3-5 C) and bi-pods display two distinct crystalline phases (separated by red lines in the Figs) stemming from the zinc blend seed and wurtzite arms (Figure 3-5 D). Upon further inspection of the 2-dimensional projection of the TEM images in Figure 3-5 C, the layer stacking is revealed. One end of the rod displays ...abc... stacking (marked in yellow on Figure 3-5 C), revealing a faced-

centered cubic (fcc) zinc blende semiconducting lattice structure, while the remaining body of the rod has ...ab... stacking pattern, revealing a hexagonal close packed (hcp) wurtzite semiconducting lattice structure, with the lattice vector [001] along the length-axis. Coincidentally, the bi-pods similarly consist of two arms of hcp lattice structure with the [001] vector pointing along the length-axis, and the arm joint is a fcc lattice. Notably, a histogram of 70 individual bipods images (Figure 3-4B) reveals the two arms join at an angle of  $109 \pm 3^\circ$ . This indicates that the pods are grown from a tetrahedron seed, confirming the fcc crystalline structure of the seed that joins the two arms. Figure 3-5 D inset shows the schematic 3D models of a truncated tetrahedron seed and the developed bi-pods from the seed model, consistent with the TEM images. Conversion from the starting zinc blende CdSe seed to the final partial wurtzite structured nanocrystal is achieved by annealing the nanocrystal in the solution at 310 °C.

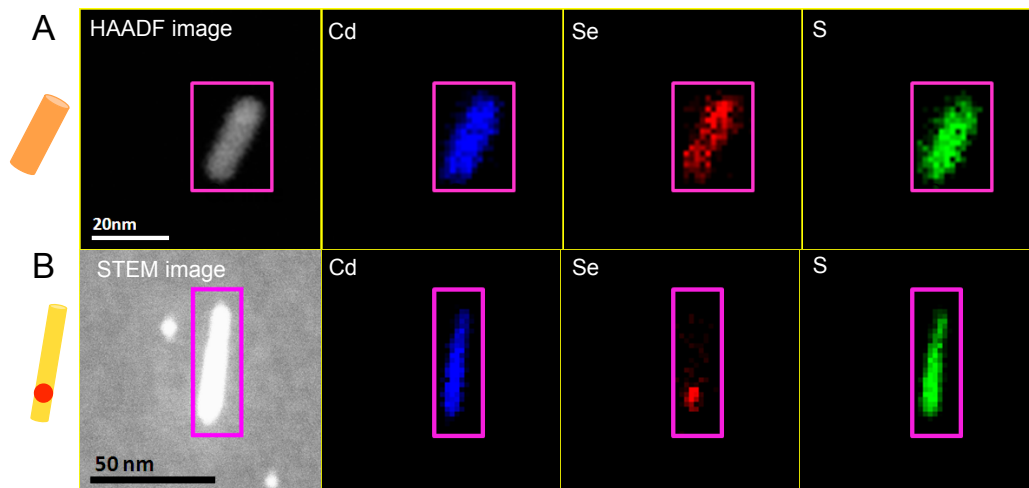
In order to gain information of the chemical composition and element distribution, we characterize the nanocrystals with large area quantitative elemental analysis using EDS, as well as high-resolution EDS mapping. For all of the quantitative EDS analysis, about 500 peak counts were obtained for the Cd, S and Se elements. Three or more spots on TEM grid were targeted and consistent results were acquired. The precision of percentage atomic ratio is estimated to be within 5 %. We found that both characterizations reveal closed to 1:1 atomic stoichiometry of Cd: (S + Se) on both averaged nanocrystals and on an individual nanocrystal. More precisely, the atomic composition of cadmium is measured as 51 % - 55 % relative to the combined atomic



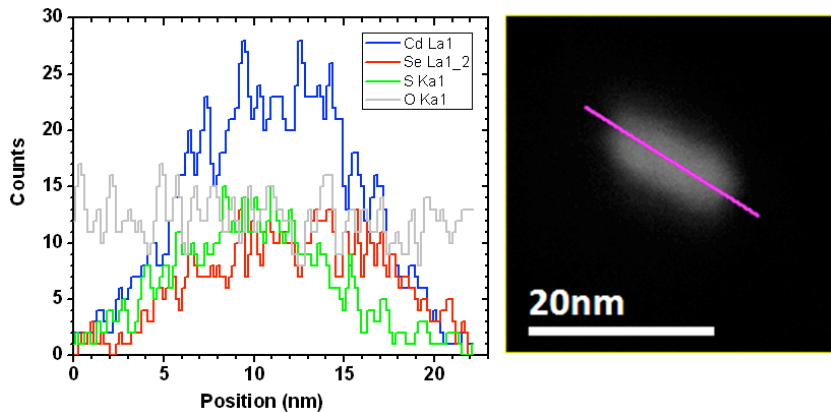
composition of S and Se (49 % - 45 % correspondingly). The 1 – 1.2 ratio of Cd: (S + Se) measured by EDS is consistent with previous findings on CdSe nanocrystals synthesized by other wet lab chemistry methods [37], due to a Cd-rich surface stoichiometry. There is no appreciable oxygen content in the nanocrystal, according to both the stoichiometry of Cd: (S + Se) ratio and oxygen (O) profile of EDS mapping, showing that the oxygen level on the nanocrystal sample is no greater than the carbon film background (See Figure 3-7).

We note that differently shaped nanocrystals possess distinct chalcogenide compositions, as quantified by the ratio of S over S and Se (x value), and summarized in Table 3-1. Generally, the S : Se ratio is around 1:1 to 4:1 for different nanocrystals. Notably, we started from 4.5 nm spherical CdSe as seed particles, without further addition of any selenium precursor, and surprisingly end up with anisotropically shaped  $\text{CdS}_x\text{Se}_{1-x}$  nanocrystals of much larger dimension. We propose the structure of the grown nanocrystal to be a crystalline pseudobinary alloy, rather than a core @ shell structure. We reason that the correspondingly sized core @ shell nanocrystal with a 4.5 nm CdSe core (in a 8 nm dia  $\times$  20 nm CdS rod) would display a S : Se ratio of  $\sim 20 : 1$ , in conflict with our observations. High-resolution EDS mapping characterization further confirmed this. As shown in Figure 3-6A, the Cd, Se, and S elements are distributed throughout the whole nanorod and thus inconstant with a core @ shell structure. As a control comparison, a core @ shell styled CdSe @ CdS nanorod was synthesized following a literature method [41] and characterized with the EDS mapping presented in the Figure 3-6B. Unlike the pseudobinary alloys we

produced, this control readily shows a CdSe core is located at about  $\frac{1}{4}$  of the rod length-axis, in agreement with the literature result [41].

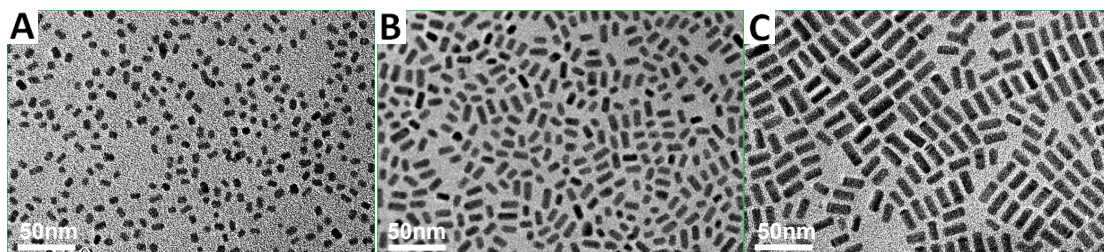


**Figure 3-6 EDS mapping characterization of a single rod-shaped semiconducting nanocrystal. (A)** EDS element mapping of an individual rod-shaped  $\text{CdS}_x\text{Se}_{1-x}$  semiconducting nanocrystal showing the S and Se distribute throughout the whole rod, rather than forming a core @ shell styled structure. The magenta frame outlines the scanning area by focused electron beam on STEM mode. **(B)** EDS mapping of a core @ shell styled  $\text{CdSe} @ \text{CdS}$  nanorod as a control comparison. Se element is located at the lower quartile of the rod length-axis as a core. Element maps of Cd, Se and S are shown in blue, red and green color, respectively. The left column schematically illustrates each structure.



**Figure 3-7** EDS line scan of an individual  $\text{CdS}_x\text{Se}_{1-x}$  rod (left) and its HAADF image (right). The magenta line represents the scanning trace. Cd, Se and S profiles are shown in blue, red and green curves, respectively.

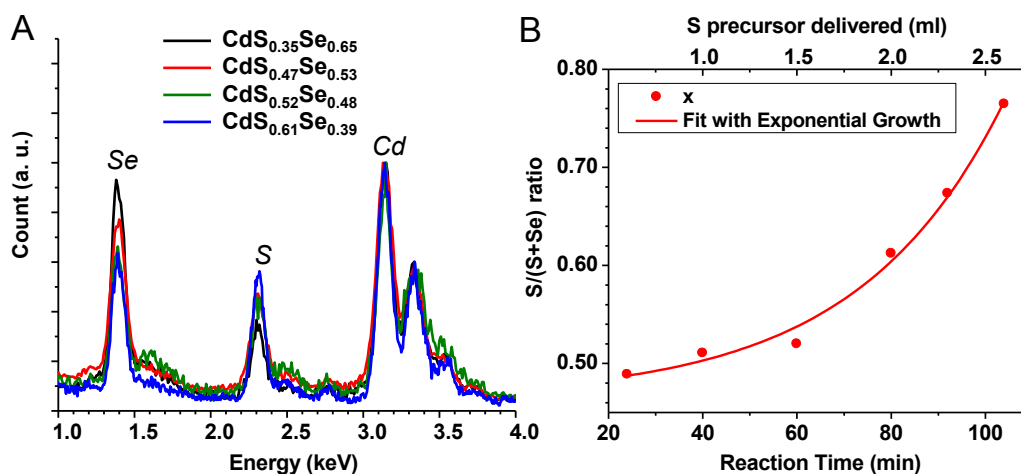
Closer inspection of the rod-shaped nanocrystal through EDS line scans reveals that the S and Se in the rod were not fully homogeneously distributed along the length-axis, but exhibited separated features with one end S-rich and the other end Se-rich. As shown by the EDS line profiles in Figure 3-7, the S and Se peaks appear at distinct positions along the long axis, while the Cd peaks at the middle of the rod, between the chalcogenide peaks. This means that the pseudobinary semiconducting rod has a gradient composition, as opposed a homogenous alloy. We did not observe such separated feature across the short-axis direction. At later nanorod growth stages, larger multi-pods structures developed with homogenous S and Se element distribution on the legs. This is attributed to ion diffusion under further annealing of the nanocrystals.



**Figure 3-8 TEM images showing size evolution of rod-shaped  $\text{CdS}_x\text{Se}_{1-x}$**

**nanocrystals** prepared with reaction times of 12 min, 92 min and 104 min from A to C. Scale bars are normalized to 50 nm in each image.

Besides anisotropy shape control over the nanocrystal using different concentrations of octanethiol, we further use the rods as a model to explore how reaction time affects nanocrystal growth. Not surprisingly, we found that as the growth time increased, the overall size (length and diameter) of the rod increased. Figure 3-8 shows representative TEM images of samples produced in time-lapsed synthesis using 12 min, 92 min, and 104 min growth time.

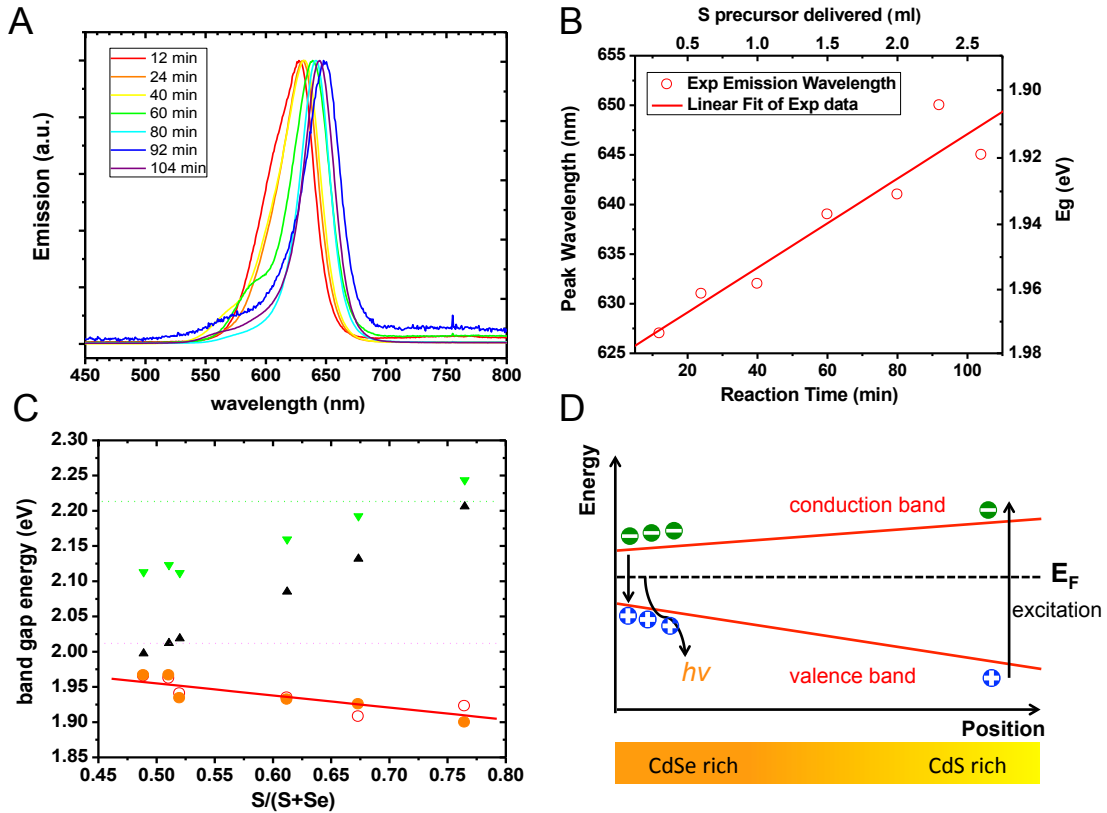


**Figure 3-9 Composition control of  $\text{CdS}_x\text{Se}_{1-x}$  nanorod (A) Normalized EDS**

spectrum of a series of  $\text{CdS}_x\text{Se}_{1-x}$  nanocrystal grown in different stages. Peaks at 1.4 keV, 2.3 keV and 3.1 keV originate from Se, S and Cd, respectively, as labeled on the

graph; **(B)** Plot of composition (x value) over the growth time as well as the sulfur precursor delivered to the reaction vial. **Red curve** is an exponential fit to the experimental data (**red sphere**). The sulfide precursor (octanethiol) was delivered into the reaction vial via the syringe pump at a rate of 0.025 ml/min, thus the corresponding volume of precursor delivered is labeled in the upper axis.

As the reaction time and nanorod size increases, there is a concomitant increase in the sulfur content in the nanorod, characterized by quantitative EDS measurement (Figure 3-9A). Peaks in Figure 3-9A are normalized to the Cd-L $\alpha$  peak at 3.13 keV. We demonstrate that the composition of the semiconducting rod nanocrystal can be fine tuned by varying the reaction time (Figure 3-9B). The CdS content can eventually take up to 77 % in the rod. This suggests that we can control the CdS composition along the length-axis of the semiconducting rod. Consequently, we adjusted the reaction time to obtain a series of rod-shaped semiconducting nanocrystals with both size and chemical composition co-dependently controlled. This has allowed us to conduct optical measurements on the series of rod-shaped CdS $_x$ Se $_{1-x}$  nanocrystals to analyze the relationship between band gap energy (E $_g$ ) of the semiconductor as a function of dimension and chemical composition.



**Figure 3-10 Optical characterization and band gap energy ( $E_g$ ) of a series of rod-shaped  $CdS_xSe_{1-x}$  nanocrystals grown with varying reaction times (A) Normalized fluorescence emission spectra following 400 nm laser excitation; (B) Peak emission wavelength versus nanocrystal growth time; (C) Band gap energy versus composition; **red circles** and the **red line** are experimental  $E_g$  and the best linear fit of the experimental data, respectively; **orange solid sphere**: theoretical  $E_g$  calculated from pure CdSe rods of the same size as the experiment; **black triangle**:  $E_g$  of bulk  $CdS_xSe_{1-x}$ ; **green triangle**: estimated lower bound limit of  $E_g$  of the  $CdS_xSe_{1-x}$  rod of the same size as the experiment. (D) Schematic energy diagram of the spatial-dependence band gap structure of a gradient  $CdS_xSe_{1-x}$  rod. The band offset data of CdSe-CdS interface is from Ref [113].**

Nanorods at different growth stages have strong band gap fluorescence, with emission peak full width at half maximum (FWHM)  $\sim 30$  nm, as characterized by ensemble fluorescence measurement in hexane colloidal solution (Figure 3-10A). The data is normalized by shifting the baseline to 0 and peaks are rescaled to the same height. For direct band gap semiconductors, fluorescence originates from band gap emission following exciton recombination, providing a measure of the band gap energy ( $E_g$ ). As shown in Figure 3-10B, the peak emission evolves with growth time. The band gap energy here decreases linearly in growth time from  $\sim 1.98$  eV to  $\sim 1.91$  eV. Note that nanorods at a specific growth time possess a unique size in terms of length and diameter, and a unique chemical composition. Both rod size and composition can influence the width of the band gap of the semiconducting nanoparticle. In order to gain better understanding of the observed range of band gap energies, we plot the  $E_g$  of nanorods grown with different reaction times versus their chemical composition (Figure 3-10C, red circles) revealing the linearly decreasing relationship between gap energy and increasing S composition (Figure 3-10C, red line). Generally, the band gap energy of a homogenous alloy material ( $\text{CdS}_x\text{Se}_{1-x}$ ) is a linear combination of  $E_g$  of the two binary materials, weighted by the molar ratio with the addition of a small non-linear term, expressed as [105]:

$$E_g(\text{CdS}_x\text{Se}_{1-x}) = xE_g(\text{CdS}) + (1-x)E_g(\text{CdSe}) - 0.3x(1-x) \quad \text{Eqn 3-5}$$

Using  $E_g$  of 1.74 eV for CdSe and 2.42 eV for CdS bulk materials, we calculated the corresponding  $E_g$  of the binary bulk material  $\text{CdS}_x\text{Se}_{1-x}$ , shown in black triangles, without considering the quantum confinement effect. Note that our nanorods synthesized at different growth times have successively larger sizes and this should

affect an additional change in  $E_g$ . Intuitively, taking the finite size effect will further increase the band gap energy due to the quantum confinement. Experimentally determined values for the  $E_g$  of rod-shaped CdSe nanoparticles have been well described by the empirical formula [34]:

$$E_{g(CdSe)}^{rod} = 1.8563 - 2.0835L^{-2} + 4.5507D^{-2} - 0.0018\left(\frac{L}{D}\right)^2 + 0.0001\left(\frac{L}{D}\right)^3 + 10.5824L^{-3} - 0.3833D^{-3} \quad \text{Eqn 3-6}$$

In this equation, L and D represent the length and diameter of the nanorod, respectively. Even though the corresponding empirical formula for CdS nanorods is not available, we can utilize the above equation to estimate the lower limit of  $E_g$  for a homogenous  $CdS_xSe_{1-x}$  nanorod, by plugging Eqn 3-6 and the bulk  $E_g$  data of CdS into Eqn 3-5, shown as the green triangle in Figure 3-10C. This yields a higher value of  $E_g$  than the bulk material shown as the black triangles. Evidently, when taking account of the homogenous chemical composition effect, both bulk and estimated nanorod  $CdS_xSe_{1-x}$  (black and green triangles in Figure 3-10C) result in a fast linear increase of  $E_g$ , as S composition increases. Our experimental data for  $E_g$  disagrees with the above-calculated band gaps that assume homogenous binary composition. Significantly, when considering a pure CdSe nanorod of the same size as the experiment, we obtain good agreement with experimental data (Figure 3-10C, orange solid spheres, and the x axis should be viewed as the size of the nanorod). This suggests that the photoluminescence from our binary  $CdS_xSe_{1-x}$  nanorods is dominated by size effects and exhibits band gap emission energy corresponding to CdSe composition only. However, this is not surprising, considering that the hybrid composition of S and Se is not uniformly distributed along the rod (See Figure 3-7 data of EDS line scan), but distributed in a gradient with S and Se enriched at



separated ends. Gradient chemical composition in one dimension creates the gradient band gap proposed in Figure 3-10D. The exciton diffusion length is of the order of hundreds of nanometers [114]. Our synthesized nanorods are well within the exciton diffusion length. Thus, when an electron is excited from the valance band to the conduction band, the electron-hole pair will then transfer to the Se enriched side, where there is lower potential for both electron and hole and additional energy gained. Recombination to the ground state at the CdSe enriched side will be accompanied by fluorescence emission. This process should enable applications that require unidirectional electron and hole transfer and uniaxial emission.

#### 4. Perspective on Synthesis and Growth Mechanism

The binary shaped semiconducting nanocrystals were discovered serendipitously, by adapting a previously published synthetic procedure [112], with modification of the concentration of injected octanethiol. Notably, we started from 4.5 nm spherical CdSe as seeds. However, instead of forming a core @ shell styled CdSe @ CdS product, we surprisingly produce select anisotropically shaped nanocrystals when varying the octanethiol injecting concentration, as summarized in Table 3-1.

In order to gain more insight of the growth mechanism, we conducted additional control experiment. Of the two injection ports via the syringe pump, we replaced the Cd precursor octadecene solution by pure octadecene, retaining only the octanethiol injection at fixed concentration of 144 mM. In the absence of Cd precursor injection,

rod-shaped  $\text{CdS}_x\text{Se}_{1-x}$  nanocrystals with the previously observed S/Se ratio still result. This control experiment indicates that octanethiol plays an important role in the formation of shaped binary nanocrystals. We further explored reaction conditions by using different nanocrystals as seeds and varying the reaction time, while maintaining the octanethiol injecting concentration fixed at 144 mM and no Cd precursor injection. Reaction conditions and results are summarized in Table 3-2. Along with the experimental conditions summarized in Table 3-1 with Cd precursor injection, nanorods under both sets of reaction conditions evolved to successively larger size and increased sulfur content, before finally transforming into multi-pods shaped nanocrystals. These experiments show that octanethiol acts as both S precursor and shape-directing reagent, presumably by preferentially capping selected crystalline facets to confine the growth rate. Importantly, the Cd precursor is unnecessary to produce rod-shaped binary nanocrystal products, but the Cd precursor accelerates the growth process. We thus conclude that the original spherical seeds are partially etched, with the dissolution of Cd and Se acting as an internal material supply for further growth.

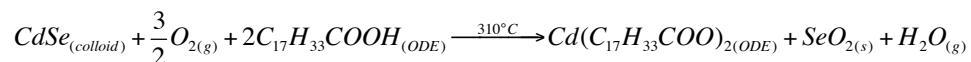
**Table 3-2 Cd precursor-free reaction conditions with fixed 144 mM octanethiol injection concentration.**

seed shape	seed S/Se ratio	reaction time (min)	product shape	product S/Se ratio
4.5 nm CdSe sphere	0	24	sphere	0.3
4.5 nm CdSe sphere	0	90	rod	0.5

<b>CdS<sub>x</sub>Se<sub>1-x</sub> nanorod</b>	1.1	120	rod, bi, tri-pods	1.4
<b>CdS<sub>x</sub>Se<sub>1-x</sub> nanorod</b>	0.56	30	rod	1.0
<b>CdS<sub>x</sub>Se<sub>1-x</sub> nanorod</b>	0.56	90	rod	1.0
<b>CdS<sub>x</sub>Se<sub>1-x</sub> nanorod</b>	0.56	150	rod, bi, tri-pod	0.9

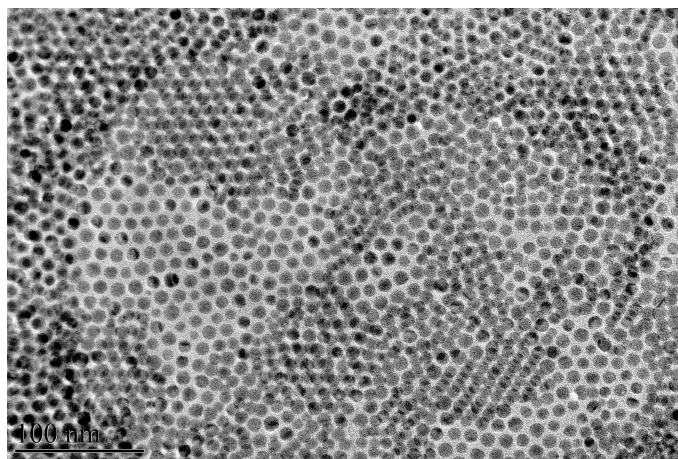
---

Another factor resulting in anisotropically shaped CdS<sub>x</sub>Se<sub>1-x</sub> nanocrystal is the presence of oxygen during growth. Instead of using the open reaction set up shown in Figure 3-2, several control experiments were performed under nitrogen flow in an airtight configuration. In this anaerobic growth, 10 nm spherical CdS<sub>0.36</sub>Se<sub>0.64</sub> nanocrystals, rather than anisotropic structures, were produced, as shown in Figure 3-11. We note that oxygen is known to physisorb and oxidize CdX (X = S, Se, Te) surfaces [115, 116]. In cooperation with octanethiol, oxygen may thus be expected to partially etch select facets of the CdSe spherical seeds by oxidation, resulting in SeO<sub>2</sub> product [115]:



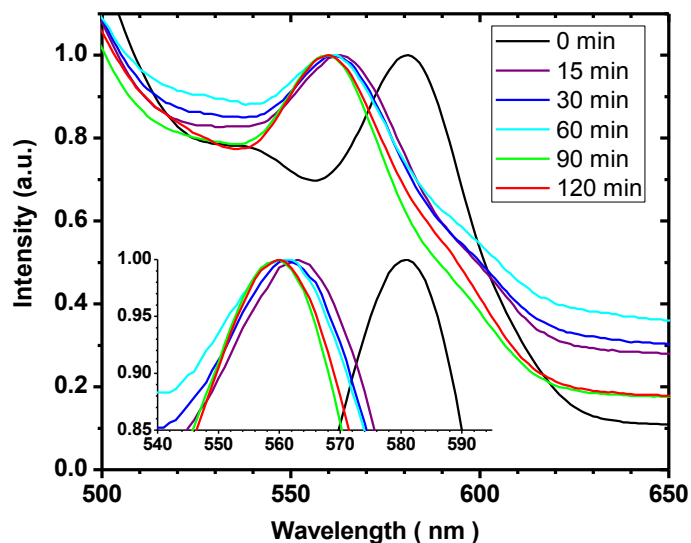
Eqn 3-7

The SeO<sub>2</sub> product dissolves in octadecene at the 310 °C reaction temperature, serving as Se precursor for further reaction.



**Figure 3-11 TEM image of spherical  $\text{CdS}_{0.36}\text{Se}_{0.64}$  nanoparticles** that results from anaerobic reaction conditions with 144 mM octanethiol injecting concentration. The scale bar is 100 nm.

To corroborate further this oxygen etching effect, we heated the starting CdSe seeds to 310 °C using the original (aerobic) experimental condition without precursor addition. We sampled aliquots of the CdSe solution along the heating time and traced the UV-Vis spectrum after the sample was cooled to room temperature. As shown in Figure 3-12, the band gap excitation of CdSe undergoes a 20 nm blue shifting within the first 15 min of heating, corresponding to a reduction of the quantum dot size up to 1 nm. This size reduction reflects partial oxidation and dissolution. At the initial growth stage, the concentration of Cd precursor supplied solely by dissolution of CdSe quantum dots is estimated to be ~ 7 mM in the growth solution, comparable with 2.5 mM  $\text{Cd}(\text{OA})_2$  precursor introduced via syringe pump injection.



**Figure 3-12 UV-Vis absorption spectra of time-dependent heated 4.5 nm spherical CdSe seed.** The 4.5 nm to 3.5 nm size decrease within 15 min indicates CdSe dissolution.

Additional kinetic studies are needed for a more detailed understanding of the impact of oxygen on the formation of anisotropic gradient alloy crystals. Oxygen may impact additional processes, including ion diffusion and fcc to hcp phase transformation at the 310 °C annealing temperature, impacting anisotropic growth. Diffusion of  $S^{2-}$  and  $Se^{2-}$  is occurring throughout the annealing process, so that gradient rod forms first, followed by the formation of more uniform alloy multi-pods. We reason that anisotropic growth is initiated at the facets of anisotropic nuclei at the very early stage. Octanethiol and oxygen cooperatively shape the original CdSe seed particle into an anisotropic faceted nuclei by selectively surface passivation and etching. In the reaction solution, the initial concentration of the CdSe quantum dots is estimated to be  $\sim 17 \mu\text{M}$ , according to measured value of the molar extinction coefficient [117]. The initial concentration of octanethiol in the reaction solution is  $\sim$

2 mM, too low to fully cap the quantum dot surface. Thus, at the initial stage of spherical nanocrystal seed, the octanethiol selectively binds to particular facets. In a wurtzite crystal, the {100} plane is the most closed packed facet. The interaction within the layer is to be the strongest and thus presumably the binding with thiol to be the weakest. A higher initial concentration of octanethiol results in tight control on growth kinetics of all other facet and epitaxial growth is preferable along the [100] direction. While a lower initial concentration of octanethiol leads to a larger portion of the crystal seed exposure to O<sub>2</sub> and multi-facets being etched at different rate depending on feature of the specific plane, results in polygon shaped nuclei.

## 5. Conclusion

In this work, anisotropically shaped pseudobinary CdS<sub>x</sub>Se<sub>1-x</sub> nanocrystals including polygon, bullet, rods and multipod structures have been synthesized for the first time as semiconducting nanomaterials. The nanorods ensemble exhibit tunable bright band gap fluorescence that is dependent on dimension. The gradient energy bands generated by one-dimensional gradient composition are of fundamental interest and potential practical importance. Such gradient energy bands could enable unidirectional emission and have potential applications in nanoelectronic devices. Experiments suggest that octanethiol acts as a shape directing reagent and oxygen is shown to also factor into the formation of the anisotropically shaped nanocrystals. Growth mechanism is proposed, and supported with control experiments.

## Chapter 4: Silica – Ag Satellites Nanostructure – Facile Synthesis and Study of Plasmon – Plasmon Coupling

### 1. Introduction

Noble metal nanoparticles (NPs) have drawn much attention due to the unique optical properties of Surface Plasmon Resonances (SPR) [10]. The properties of a SPR are greatly dependent on the metal NP's size, shape, and surface environment [12, 15, 16]. Silver (Ag) NPs, an intensively studied material, possess SPRs with optical absorption tunable across the whole visible spectrum by varying the NPs shape and size [118]. As such, Ag NPs have been applied in the field of Raman enhancement [119, 120], optical sensing [121], and catalysis [122, 123]. Moreover, various types of Ag-based nano-sized composites have also been synthesized. Ag NPs are immobilized on substrates of different nanomaterials, such as Ag NPs on polystyrene micro- beads [124] and silica nano-spheres [125, 126], and Ag NPs on the surface of carbonaceous nano-spheres [127]. Compared with the free standing metal NPs in colloidal solution, those hybridized with the substrates present higher stability and better catalytic performance. Immobilization on the substrate effectively prevents NPs forming agglomerates even in the presence of electrolytes [125]. Furthermore, Ag NP-decorated silica micro- beads with high NP surface coverage have good surface-enhanced Raman scattering (SERS) performance [126], due to the existence of a hot spot plasmon between the closely neighbored Ag NPs, and the highly rough surface [128]. Ag NPs on carbonaceous nano-spheres have

demonstrated selective biomolecule sensing. Because of the dissimilarity of the materials, direct growth of the Ag NPs on silica is often lacking in control, in terms of NPs size, uniformity, and shape, all potentially important factors for applications of SPR. The main difficulty lies in simultaneously immobilization of Ag NPs on the substrate with control of NP growth kinetics.

In this work, I introduce a facile synthetic route to achieve a silica-Ag nano-composite consisting of Ag NPs as satellites on a silica nano- sphere. The Ag satellites are well controlled in size, shape, and quantity on silica nano- spheres, and exhibit optical extinction spectra with features indicative of dispersion in solution. The silica-Ag satellites nanostructure is well suited to the manipulation of plasmonic NPs into coupling assemblies for generating hot spot plasmon. Herein, I selectively fabricated a core @ shell – satellites chain-like assembly structure by adapting a gold or Ag NP core into a silica shell with controlled shell thickness. By stepwise increasing the surface coverage of the Ag satellites, plasmon-plasmon coupling within the assembly structure, characterized by consistently red shifting of surface plasmon resonance, was directly observed. The dipole-dipole interactions among the metallic NPs are simulated and confirmed by Discrete Dipole Approximation simulation (DDA). Lastly, the Ag NPs on silica nano-sphere were converted into hydrophilic CdSe quantum dots on amorphous silica. The resulting silica-CdSe hybrid nanocomposites have shown size dependent band gap fluorescence and trap state emission characterized by fluorescence spectroscopy.



## 2. Experimental Methods

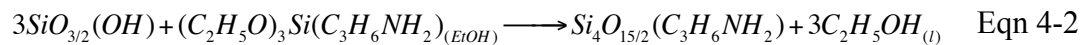
### 2.1 Synthesis of Silica-Ag Satellites Nanostructure

#### *Synthesis of 50 nm silica nano- sphere*



Adapted from a base-catalyzed silica formation from tetraethyl orthosilicate (TEOS) in a water-in-oil microemulsion method [129], 50 nm silica nano-spheres are prepared by mixing 34 ml cyclohexane, 1.6 ml IgePAL CO-520 and 0.26 ml (25 % - 28 %) ammonium hydroxide solution, sonicating and stirring for 5 min at room temperature (R.T.), followed by quick injection of 0.3 ml TEOS. The reaction solution is then constantly stirred at R.T. for 24 hours. Then reaction product is precipitated by addition of acetone (up to 50 ml) and centrifugation (under 1000 rpm for 5 min). The white, semitransparent gel is re-dispersed into methanol and centrifuged at 5500 rpm for 15 min. After another re-dispersion/precipitation cycle in methanol is repeated, the resultant 50 nm silica spheres are dispersed into 50 ml ethanol and stored for further usage.

#### *APS functionalization on silica surface*



A 50 ml silica nano-spheres dispersion in ethanol (EtOH) is mixed with 0.5 ml (25 % - 28 %) ammonium hydroxide, added with 30 µl pure (3-aminopropyl) triethoxysilane (APS, air aged or freshly opened protected in glove box), and stirred overnight at R.T. The resultant product is washed three times with ethanol under 5500

rpm centrifugation for 10 min, to remove excess APS and re-disperse into 50 ml ethanol.

*Synthesis of silica-Ag Satellites Nanostructure (spherical Ag NPs)*



A 2.5 ml aliquot of APS functionalized silica nano-sphere in ethanol solution is combined with ethanol to a volume of 4 ml, and then 0.04 g polyvinylpyrrolidone (PVP) powder is added and mixed by fast vortex until totally dissolved, then 50  $\mu\text{l}$  (0.1 M)  $\text{AgNO}_3$  aqueous solution is added before aged at R.T. overnight without perturbation. The product is washed by centrifugation at 3700 rpm for 15 min three times and the deep yellow precipitate is re-dispersed into 4 ml ethanol. Table 4-1 summarizes the synthetic conditions used to fabricate silica-Ag hybrid NPs with controlled Ag NP size and quantity.

**Table 4-1 Synthetic parameters for controlled silica-Ag hybrid NPs formation**

<b>N Ag / D*</b>	<b>13 Ag<sup>#</sup> / 5 nm</b>	<b>25 Ag<sup>#</sup> / 3 nm</b>	<b>25 Ag<sup>#</sup> / 5 nm</b>	<b>17 Ag / 8 nm</b>	<b>80 Ag / 3 nm<sup>†</sup></b>
<b>APS</b>	fresh	aged	aged	aged	aged
<b>PVP (g)</b>	0.04	0.04	0.04	0.04	1.6
<b>AgNO<sub>3</sub> concentration (M)</b>	0.1	0.1	0.1	0.02	0.1
<b>AgNO<sub>3</sub> volume (ml)</b>	0.05	0.05	0.05	1	0.05
<b>temperature (°C)</b>	R.T.	R.T.	R.T.	70	R.T.
<b>Time (hours)</b>	24	24	72	24	24

\*N and D represent the averaged number and diameter of Ag satellites. The range of observed diameter from TEM images is  $\pm 1$  nm, unless otherwise noted.

# Standard deviation of  $\pm 8$  nm was obtained according to Gaussian fit of the corresponding histograms.

† Observed diameter ranges as 2 – 6 nm.

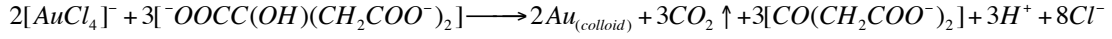
#### *Synthesis of silica-Ag Satellites Nanostructure (cube-shaped Ag NPs)*



Silica-Ag Satellites Nanostructures with cube-shaped Ag NPs on silica are prepared by modification of Xia's method [130]. The APS functionalized silica is centrifuged and re-dispersed into 5 ml ethylene glycol (EG) via sonication in a 50 ml flask. In 150 °C oil bath, 0.06 ml 3 mM sodium hydrosulfide EG solution was quickly injected into the flask. After 2 min, 0.5 ml 3 mM EG solution of hydrochloride acid (prepared from 37 % hydrochloride acid) was injected followed by addition of 1.25 ml PVP (MW55000, 20 mg/ml in EG). After another 2 min, 0.4 ml 282 mM silver trifluoroacetate EG solution was added. During the whole process the flask was capped with a glass stopper except during the addition of reagents. After 15 min – 30 min, the solution became cloudy and deep yellow, and then the reaction was quenched by placing the flask in an ice-water bath. To remove EG, excess PVP and un-reacted chemicals, the product was thrice added with acetone and centrifuged under 3000 rpm for 10 min and re-disperse into ethanol.

## 2.2 Synthesis of Core @ Spacer – Satellites Metallic Assembly

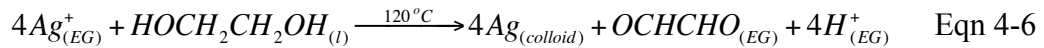
### *Synthesis of Au @ silica core @ shell NPs*



Eqn 4-5

Au @ silica NPs was synthesized following a previously published method developed by Liz-Marzan [131]. A freshly prepared citrate stabilized Au colloidal must be used to prepare non-aggregated Au @ silica NPs. Firstly, 25  $\mu$ l freshly prepared 1 mM APS water solution was added to 5 ml as made citrate stabilized 15 nm Au colloidal solution and fast stirred at R.T. for 15 min, followed by quick injection of 0.2 ml 1 : 40 (v/v) sodium silicate water dilution. This mixture was allowed to stand at R.T. and constantly stirred for 4 days to get silica shell thickness of 5 nm, and 10 days for 10 nm. Ultracentrifugation at 10000 rpm for 30 min was then used to separate the Au @ silica NPs and re-disperse into ethanol.

### *Synthesis of Ag @ silica core @ shell NPs*



Firstly, PVP capped 20 nm sized Ag NPs were synthesized following a published method [132]. 40 mg AgNO<sub>3</sub>, 1 g PVP, and 7.5 ml EG were mixed and stirred at R.T. until dissolved. The solution was then heated to 120 °C, and remained for 1 hour at this temperature. The colloidal dispersion was then cooled to R.T. The product can be easily separated from EG after addition of 50 ml acetone followed by centrifugation. Finally the PVP capped Ag NPs were re-dispersed in ethanol.

This ethanol dispersion was washed again and re-dispersed into 8 ml ethanol, followed by addition of 0.336 ml ammonium hydroxide (29.3 wt % NH<sub>3</sub> in water). Immediately after this 0.1 ml TEOS solution (10 v/v % in ethanol) was added with fast stirring. The reaction mixture was then stirred for another 12 hours and separated by ultracentrifugation and re-dispersion. The resulting silica shell thickness is 5 nm.

#### *Synthesis of core @ silica – satellites structure*

The above Au (Ag) @ silica core @ shell was functionalized with APS by addition of 10 % (v/v) APS ethanol solution in 2 ml ethanol dispersion of metal core @ silica NPs, allowing aging at R.T. for 2 hrs, then 50°C for 1 hr [133]. At this point, one can follow the above method for growth of Ag NPs satellites on a silica shell.

#### *Ensemble measurement of surface plasmon resonance*

The SPR was characterized with a Shimadzu UV-2501PC UV-Vis absorption spectrometer. The ethanol dispersion of different nanostructures was delivered in a 10 mm cuvette, and the light signal is monitored from 300 nm to 800 nm.

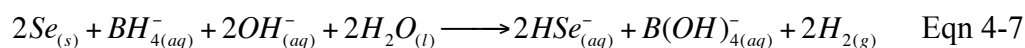
### 2.3 Synthesis of silica-CdSe quantum dots composites from silica-Ag composites

#### *Preparation of silica-Ag composites*

To prepare silica-Ag composites, 0.04 g PVP was added in 4 ml ethanol dispersion of APS functionalized silica nano-sphere, followed by addition of 0.05 ml 0.1 M silver nitrate aqueous solution and subsequent aging for 24 hours at R.T without

stirring. After washing three times with ethanol, the resulting silica-Ag composites were used to convert into silica-CdSe composites with a characteristic 590 nm emission from band edge transitions. Another batch of silica-Ag composites were prepared with the same protocols, except for using 0.8 g instead of 0.04 g PVP, resulting in silica-CdSe composites emitting at 640 nm at band edge transition.

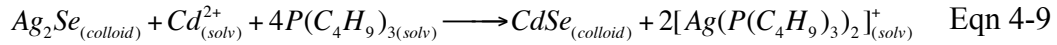
*Preparation of NaHSe water solution*



Freshly prepared NaHSe was used as a precursor to react with silica-Ag forming silica-Ag<sub>2</sub>Se. To prepare aqueous solutions of NaHSe, a 50 ml plastic centrifuging tube was loaded with 50 ml water, pre-cooled in ice-water bath and kept degasing with N<sub>2</sub> by inserting a glass pipette into the vial bottom. 37 mg Se powder was loaded in a 5 ml glass vial, followed by addition of several drops of acetone to thoroughly soak all the Se powder. A glass pipette was inserted to gently blow the N<sub>2</sub> gas to dry the acetone soaked Se powder, to obtain a clot of compacted Se powder aggregated on the bottom of the vial. Then, 60 mg NaBH<sub>4</sub> powder and 1 ml cold water (taken from the above 50 ml ice cold water) were added into the Se glass vial and quickly sealed with Parafilm. A syringe needle was inserted through Parafilm to prevent O<sub>2</sub> admission and to avoid overpressure due to generation of H<sub>2</sub>. The reaction was left in the ice-water bath and allowed to react for 2 – 3 hours, until all the black Se powder transformed into colorless NaHSe concentrated aqueous solution. (A pink solution indicates presence of Se, due to oxidation of NaHSe back to Se). Then, 1 ml of the colorless NaHSe solution was carefully extracted and injected quickly into the

remaining 49 ml ice-cold degassed water in the centrifuging tube. The tube was then immediately capped and quickly shaken by hand for thoroughly mixing to make a 1 : 50 dilution of NaHSe solution. This NaHSe solution is extremely sensitive to oxygen and decomposed quickly, and must be freshly prepared and directly used.

*Preparation of silica-CdSe composites*



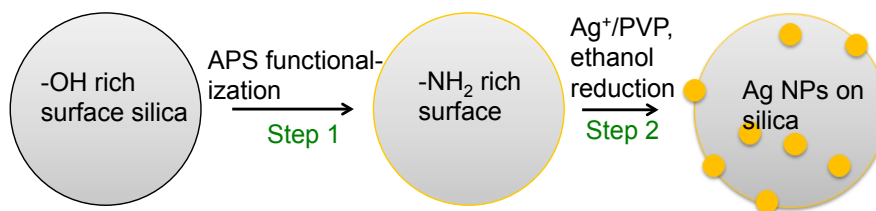
The Ag-silica in 4 ml ethanol solution was pre-degassed by N<sub>2</sub> at 60 °C in an oil bath for 15 min, followed by addition of 0.2 ml above 1 : 50 diluted NaHSe aqueous solution, and reaction for 15 min under gas protection at 60 °C. After the reaction was completed, the product was centrifuged at 3500 rpm for 10 min, and re-dispersed into 4ml ethanol. Then, 0.5 ml methanol solution of cadmium nitrate (0.25 g dissolved in 10 ml methanol) was added under N<sub>2</sub> protection at room temperature, followed by addition of 2 drops of TBP. After 30 min, the product of silica-CdSe composite was washed and re-dispersed into ethanol.

*Measurement of fluorescence*

The ensemble fluorescence measurement of silica-CdSe composites was conducted using a portable USB fluorescence spectrometer by Ocean Optics™. The ethanol dispersion was placed in a 2 mm quartz cuvette supported on a 10 mm sample holder across the diagonal direction to make a ~ 90 ° optical path. The sample was

irradiated with a 400 nm blue laser and the luminescence was monitored from 350 nm to 1100 nm.

### 3. Facile Synthesis of Silica – Ag Satellites Nanostructures



**Figure 4-1 Illustration of synthetic route for silica-Ag satellites nanostructures**

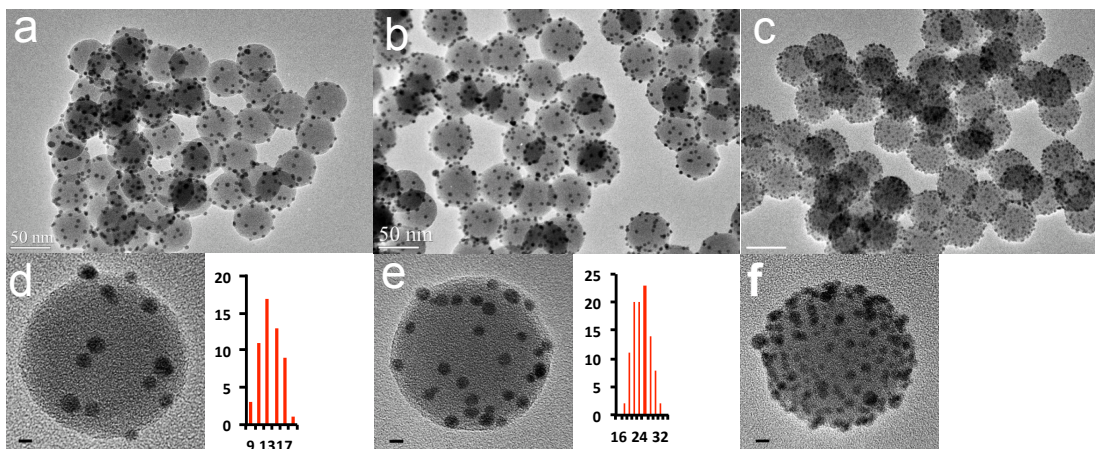
APS: (3-aminopropyl) triethoxysilane; PVP: polyvinylpyrrolidone and TBP: tributylphosphine

The silica-Ag Satellites Nanostructure consists of Ag NPs “satellites” distributed on the surface of a 50 nm silica nano- sphere. The facile synthetic route is schematically described in Figure 4-1. The as prepared silica nanoparticles dispersed in ethanol possess hydroxyl-rich surfaces to prevent silica particle aggregation. Because of the low affinity of hydroxyl for Ag, the direct overgrowth of Ag NPs on silica, suffers from very limited control of the growth kinetic. To circumvent this difficulty, the silica surface is first functionalized with a silane coupling reagent, (3-aminopropyl) triethoxysilane (APS) (step 1), forming an amine-rich surface which possess much higher affinity for Ag. Next, over growth of Ag NPs is realized by adding aliquots of AgNO<sub>3</sub> aqueous solution as the precursor and polyvinylpyrrolidone (PVP) as the capping ligand into the ethanol dispersion of silica nano- spheres (step 2). Ethanol then serves as a mild reducing reagent to slowly reduce Ag (I) to Ag (0),

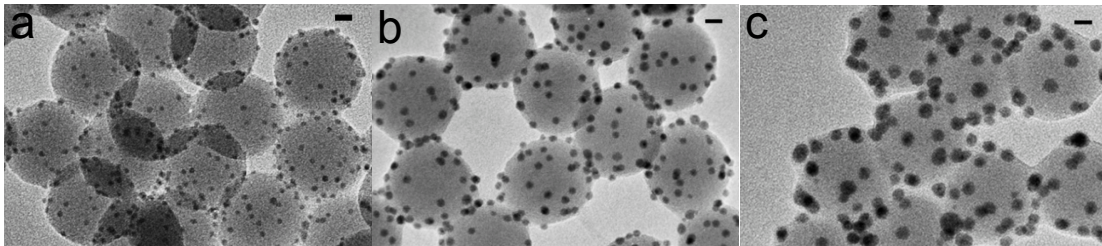


forming Ag NPs on silica nano- sphere. Notably, this facile synthetic route successfully achieved control on quantity, size and shape of Ag NPs on silica, by variation of reaction conditions including temperature, time, and reagent concentration.

This facile synthetic route allows a degree of control of Ag NPs growth. Figure 4-2 demonstrates the control achieved over the addition of different quantities of Ag NPs on a silica nano-sphere of a given diameter. Figure 4-2 (a, d) and (b, e) shows samples with an average of 13 and 25 Ag NPs, respectively. The histograms of (d) and (e) are constructed from counting ~ 60 individual silica-Ag satellites nanostructure. Figure 4-2 (c, f) presents a sample that has more Ag NPs up to ~ 80 on a silica sphere. Moreover, by extending the reaction time and raising the temperature, the size of the Ag NPs is tunable from 3 nm up to 8 nm, as shown in Figure 4-3.

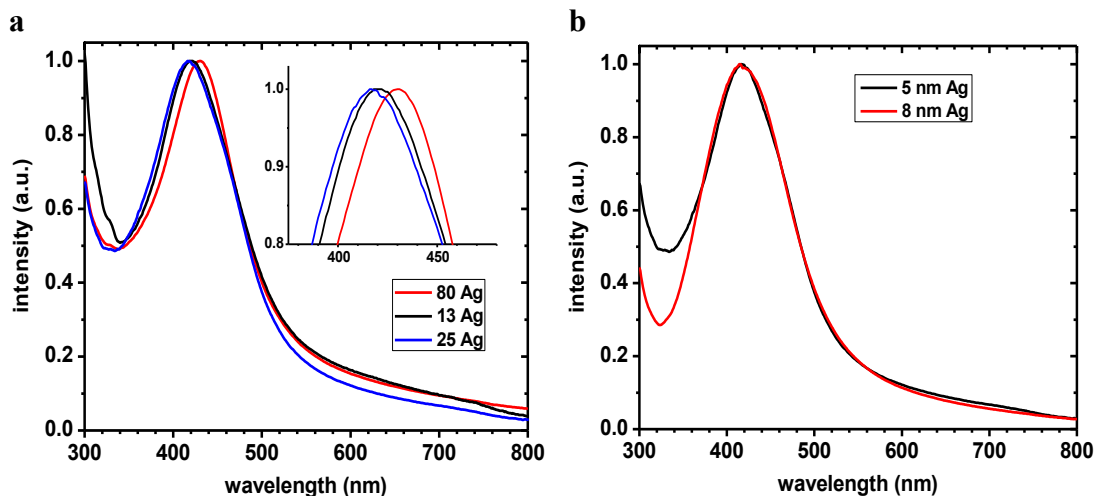


**Figure 4-2** Low-resolution TEM images (a-c) of Silica-Ag satellites nanostructures with different quantity of Ag NPs per silica and the corresponding close-up view of TEM images (d-f) Scale bar is 50 nm on a-c and 5 nm on d-f. Histogram of number of Ag NPs on one silica nano-sphere is shown to the right of d and e.



**Figure 4-3** Low-resolution TEM images showing different size of Ag NPs on silica. The diameters of Ag NPs range as 3 nm, 5 nm, and 8 nm from (a) to (c). The scale bars are 10 nm.

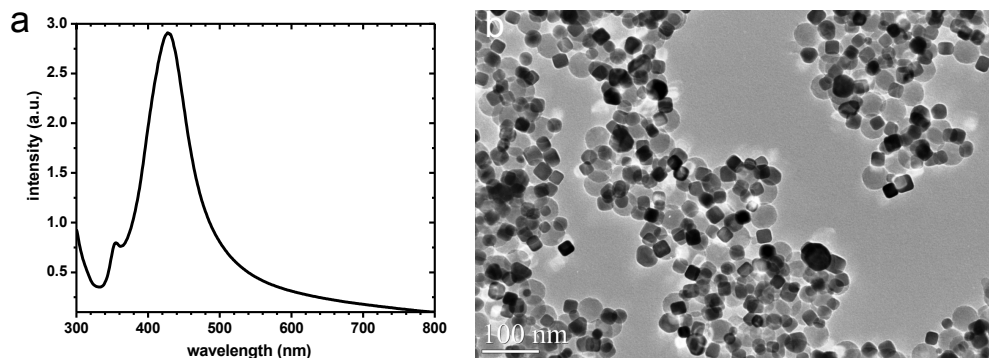
The Ag NPs satellites on silica are characterized by UV-Vis absorption spectroscopy shown in Figure 4-4. The Ag NPs in all samples present well-dispersed features in solution, according to the 420 nm peak position of surface plasmon resonance for individual Ag NPs. In Figure 4-4 (a), the sample of highest coverage with  $\sim 80$  Ag NPs per silica has a 10 nm red-shifted SPR. However there is no corresponding broadening of the spectral feature, indicating that aggregation of NPs is unlikely. This also suggests that there is no significant dipole-dipole coupling between the Ag NPs due to an increase of surface coverage on silica. A randomly distributed Ag NPs assembly on a spherical surface plus the inhomogeneity between individual assemblies typically leads to broadening of the SPR, if any dipole couplings are presented. (See section 4 and 5) Noting that the largest Ag NPs loadings ( $\sim 80$  numbers of Ag NPs) on silica required high concentration of PVP capping, the red shifting of SPR is attributed to increase of the dielectric constant of the surface environment.



**Figure 4-4 Normalized extinction spectra of Silica-Ag satellites nanostructures**

**samples (a)** Differing numbers of Ag NPs per silica. Black, blue and red represent the 13, 25 and ~ 80 Ag NPs on average per silica, respectively **(b)** different size of Ag NPs. Black and red represent the 5 nm sized Ag NPs and 8 nm sized Ag NPs, respectively, and the common peak at 420 nm.

I next show that the synthetic route can also produce cube-shaped Ag NPs on silica, by adapting a polyol process assisted by PVP. The polyol process was previously used to synthesize freestanding Ag nanocubes [134]. I applied the condition of the Ag nanocubes synthesis to the step-2 reaction described above, and found it works well to load Ag nanocubes on silica (Figure 4-5b). Figure 4-5a shows the extinction spectrum of the silica-Ag nanostructures ensemble. The main peak at 428 nm, accompanied with an extra plasmon resonance mode as a small peak at 355 nm, are the characteristic signature of a well dispersed cube-shaped Ag NPs.



**Figure 4-5 Extinction spectra of cube-shaped Ag NPs on silica (a) and the corresponding TEM image (b)**

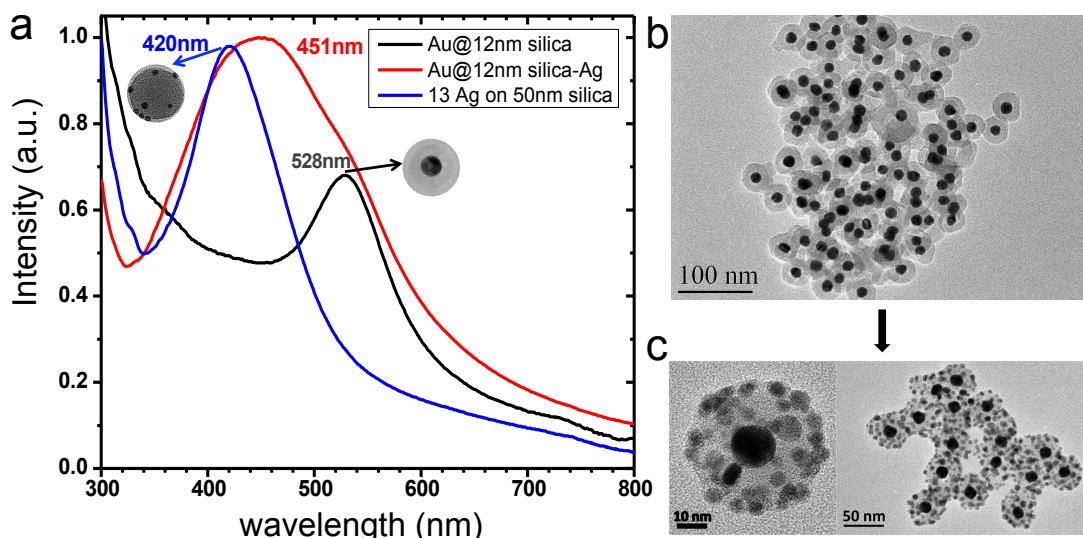
In the synthetic strategy, surface functionalization of silica with APS and addition of PVP play critical roles. Control experiment shows that silica without APS functionalization results in few to no Ag nuclei on silica, due to the low affinity of –OH with Ag. With APS functionalization, < 1 nm Ag nuclei easily form on silica at the initial growth stage. Further kinetic control on Ag NPs growth can then be realized only with the presence of PVP. In agreement with previous studies, PVP plays several roles in the Ag NP growth process: (1). Ag<sup>+</sup> and PVP form coordination complex with N and O atoms of PVP units sharing their lone pairs with Ag<sup>+</sup>, forming a complex that can serve as Ag (I) precursor [135]; (2). Enlargement of Ag nuclei on the silica surface is promoted by PVP [132]. PVP as a hydrophilic polymer can wrap on silica nano-spheres presumably via hydrogen bonding between O atoms of PVP and -NH<sub>2</sub> / -OH groups on the silica surface. This enriches the silica surface of Ag (I) precursor, promoting the enlargement of Ag nuclei on silica. Thus, the greater PVP wrapping on silica, the more each Ag NP develops from the initial nuclei. This agrees with our general observation that a higher concentration of PVP leads to more and larger Ag NPs per silica. In contrast, our control experiment showed that without

enough PVP, only  $< 1$  nm Ag nuclei was observed on silica. The lower bound limit of PVP concentration required is determined to be 0.5 %. (3). PVP serves as capping ligand to stabilize Ag NPs and harness the growing rate [135]. A higher concentration of PVP typically leads to more quantity coupled with smaller size of Ag NPs (see Figure 4-2), due to stronger surface capping on Ag and tight control on the growth rate.

#### 4. Core @ Spacer – Satellites Metallic Assembly: Dipole – Dipole Interaction Between Metallic NPs

With the above synthetic route, I designed and synthesized a core @ shell – satellites metallic chain-like assembly structure, by over coating a silica shell on a Au (or Ag NP) core and then growing Ag NPs as satellites on the silica shell. In this structure silica serves as an intermediate to assemble the metallic NPs into a close unit. More importantly, Silica as an electric insulator has high-lying energy levels that are far from the plasmonic levels, thus does not have any charge transfer or Coulomb interaction with metallic NPs. The silica shell thus serves as a spacer of the metallic NPs assembly, where the dipole – dipole coupling between the metallic NPs occurred due to proximal distances between NPs. In order to direct the coupling between the metallic core and the surrounding satellites, the thickness of silica shell must be controlled within the interaction range of 12 nm.

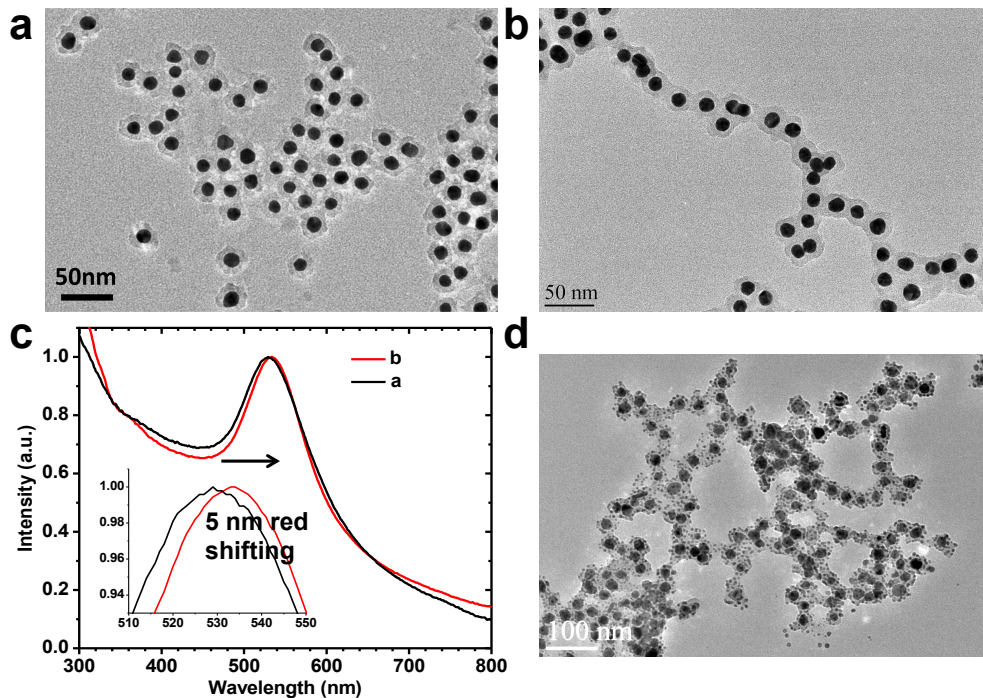
Plasmon - plasmon coupling is observed with a decreased energy of surface plasmon resonance in extinction spectrum, due to collective Coulomb interaction between the vibrating electrons within nearby metal nanoparticles. Such coupling occurs in our designed synthesized Au @ silica – Ag and Ag @ silica – Ag nanostructures. In the case of Au @ silica – Ag nanostructure, a 13 nm Au core in 12 nm thick silica shell, surrounded by 5 nm Ag NPs as satellites, was synthesized (Figure 4-6 c). The corresponding SPR feature is shown in Figure 4-6 a (red curve). For comparison, the extinction spectrum of the starting material of Au @ silica with 12 nm shell in ethanol is plotted (black curve). The resonance peak at 528 nm confirms that the individually dispersed Au @ silica NPs are without dipole – dipole coupling [49]. (Due to the increased dielectric constant of silica shell and ethanol solvent, the 520 nm SPR of as made Au NPs in water is red shifted to 528 nm.) The SPR of a silica-Ag satellites nanostructure without a metallic core is also plotted in blue. The corresponding 420 nm SPR clearly shows non-coupling Ag NPs on silica. In contrast, the SPR of the Au @ silica – Ag nanostructure (red curve) exhibits a broadened and red shifted main peak at 451 nm, relative to the 420 nm non-coupling Ag NPs, and a shoulder near 528 nm non-coupling Au @ silica NPs. Notably, a linear combination of spectra of the two reference structures cannot lead to the broadening and red shifting of the SPR peak at 420 nm. Instead, since both the black and the blue curves have negative slopes at the peak position of the other (420 nm for the black curve and 528 nm for the blue curve), a linear combination of the two spectra will result in blue shifting of peaks at 420 nm and 528 nm. We thus attribute the 30 nm red shifted SPR of Ag NPs to the dipole-dipole coupling between metallic NPs.



**Figure 4-6 Characterization of Au @ silica – Ag nanostructure with 12 nm silica shell as spacer (a) extinction spectra (red curve), (c) TEM images and (b) the starting Au @ 12 nm silica core @ shell NPs, from which the Ag NPs satellites were grown (extinction spectra is in black curve). Blue curve: silica-Ag satellites nanostructures without metallic NPs as core, showing SPR of Ag NPs without coupling. Note: Nanoparticles are dispersed in solvent, and aggregate on TEM grid following solvent evaporation.**

We next explore how hierarchical structure of the nanoparticles impacts the SPR. The Au @ silica colloids become unstable and form onset of aggregates after APS functionalization. This is more evident when the thickness of silica shell decreases to 6 nm, and is characterized both with TEM images as well as UV-Vis spectroscopy. As shown in Figure 4-7, the Au @ silica with 6 nm thickness NPs are well dispersed before the APS functionalization, as seen from the TEM images of Figure 4-7 a, and as consistent with the 528 nm peak of SPR (Figure 4-7 c black curve) for non-aggregating Au NPs [49]. After APS functionalization, however, the SPR has red

shifted to 533 nm, and appears as onset of aggregates in TEM characterization, shown in Figure 4-7 b. SPR is very sensitive to the distance of NPs within this regime, thus the 5 nm red shifting likely reflects the plasmon coupling between the Au cores in the chain-like structures. As previously discussed [49], the reduced colloidal stability of APS functionalized Au @ silica NPs occurs from insufficient net charges within the interfacial double layer of NPs, as characterized by zeta potential measurement. For silica coated Au NPs with ~ 6 nm shell, the zeta potential changes from - 40 mV to + 20 mV after APS functionalization. This means the negatively charged silica surface is shield by APS moiety with insufficient positive charges, producing an instable colloidal system. This results in onset of aggregates of subsequent Au @ silica – Ag nanostructures after Ag NPs growth, instead of well-isolated core – satellites (Figure 4-7 d).



**Figure 4-7 Characterization of Au @ silica (6 nm thickness) NPs before and after APS surface functionalization: (a) Typical TEM image of Au @ silica (6 nm)**

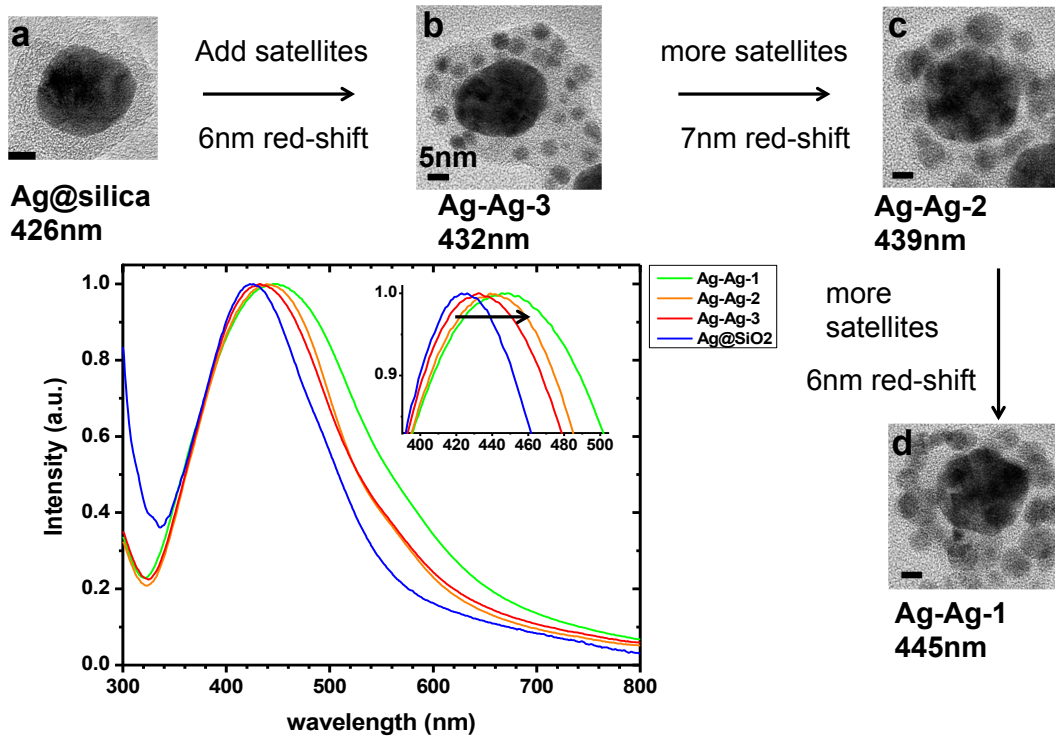


prior to APS functionalization. Note aggregation due to solvent evaporation as in Figure 4-6. **(b)** Typical TEM image following APS functionalization. Note the chain-like and branched structure indicative of the morphology of APS functionalized particles in ethanol. **(c)** Corresponding normalized extinction spectra; Black curve and red curve represent sample in (a) and (b), respectively. **(d)** Typical TEM image of the Au @ silica – Ag after subsequent growth of Ag NPs satellites.

Other than Au core with Ag NPs satellites assembly, I also synthesized 22 nm Ag core in ~ 5 nm silica shell with increasing coverage of Ag satellites, shown in Figure 4-8. As the surface coverage of the Ag satellites increases, there is systematic broadening and red shifting of SPR for Ag NPs, from 426 nm to 445 nm, suggesting the features of dipole – dipole coupling due to closed assembly of Ag NPs. Similar to the case of Au @ silica NPs, Ag @ silica NPs exhibit onset of aggregation after APS functionalization. Thus, extra factors must be taken into account to describe the plasmon coupling. Other than coupling of core – satellites and satellites – satellites on a silica shell, coupling between the neighboring cores within a chain (core – core) as well as satellites – satellites coupling at adjacent silica shells also play a role.

In order to estimate the order of magnitude of SPR red shift due to plasmon coupling within the metallic assembly, and verify the experimental observations, numerical simulations are performed to calculate the extinction spectrum of an isolated 22 nm Ag core with a 5 nm dielectric shell surrounded by different quantity

of smaller Ag satellites. The simulated SPR feature shows reasonable agreement with the experiment, as described in detail in the next section.



**Figure 4-8 Characterization of Ag @ silica – Ag nanostructure with ~ 5 nm silica shell as spacer:** Close-up TEM images of the starting Ag @ silica NPs after APS functionalization (**a**) and the varying Ag @ silica – Ag nanostructure with increasing coverage of Ag satellites (**b – d**). Scale bars are 5 nm. The corresponding normalized extinction spectra are shown in blue, red, orange and green curves for structure (a) through (d), respectively. All nanostructures are dispersed in ethanol for UV-Vis absorption spectroscopy measurement.

## 5. Simulation of the Dipole – Dipole Interaction

Numerical simulations are performed with the Discrete Dipole Approximation (DDA) method, using the open source code package DDSCAT developed by Draine and Flatau [136]. DDA is a method for computing the scattering and absorption property of a target with arbitrary geometry [137]. The method divides the targeted object onto an array of a uniform lattice, where each lattice point consists of a dipole. Under the framework of electrodynamics, by calculating how the dipoles are polarized in response to the local electromagnetic field radiating on the object, the scattering and absorption coefficient of the object, as well as the electromagnetic field distribution over the internal and surrounding space can be obtained. Other than interacting with the external monochromatic plane wave, individual vibrating dipoles also generate local electromagnetic fields that can interact with neighboring dipoles, thus the method take fully into account the coupling between dipoles. The only approximation in the DDA method is the treatment of a continuum target with an array of discrete dipoles. Thus the method is valid and accurate within a few percent only when the dipole spacing is small enough to well describe the geometry of the target and small compared to the wavelength. Nevertheless, smaller dipole spacing will give higher accuracy in sacrifice of the computing time.

DDSCAT Fortran code package handles the calculation by searching the self-consistent solution for the dipole polarization, with specified location of the dipoles (describing the geometry of target) and dipole polarizability via input of dielectric function of targeted material. For absorbing material such as gold and silver, the

frequency dependent complex dielectric function,  $\varepsilon(\omega)$ , has real and imaginary parts  $\varepsilon_1$  and  $\varepsilon_2$ , and is directly related to refractive index ( $m$ ),

$$\varepsilon(\omega) = m(\omega)^2 \quad \text{Eqn 4-10}$$

where  $m$  is also consisted of real and imaginary parts  $n$  and  $k$ . Thus, we have

$$n^2 - k^2 = \varepsilon_1 \quad \text{Eqn 4-11a}$$

$$2nk = \varepsilon_2 \quad \text{Eqn 4-11b}$$

From Eqn 4-11a and 4-11b, the refractive index  $m=n+ik$  is solved with

$$n = \sqrt{\frac{\sqrt{\varepsilon_1^2 + \varepsilon_2^2} + \varepsilon_1}{2}} \quad \text{Eqn 4-12a}$$

$$k = \sqrt{\frac{\sqrt{\varepsilon_1^2 + \varepsilon_2^2} - \varepsilon_1}{2}} \quad \text{Eqn 4-12b}$$

The real part  $n$  accounts for refraction of incident light by the material, and the imaginary part,  $k$ , deals with the absorption. According to Drude model for bulk metal material [138],

$$\varepsilon(\omega) = 1 - \frac{\omega_p^2}{\omega(\omega + i\gamma)} \quad \text{Eqn 4-13}$$

In the equation,  $\omega_p$  is plasma frequency.  $\gamma$  is damping frequency and inverse of the electron relaxation time. In bulk metal materials, the parameter  $\gamma$  deals with how frequently the collisions between the conducting electrons and lattice occur. For the case of nanoparticles, an additional damping frequency related to collisions of electrons with the particle surface need to be taken into account [139]. Thus, we introduce a damping correction  $\gamma_a$  for nanoparticles,

$$\gamma_a = g \times \frac{v_F}{a_{eff}} \quad \text{Eqn 4-14}$$

where  $a_{eff}$  and  $v_F$  are effective radius (equal to radius for spherical particles) and Fermi velocity, respectively. The  $g$  factor is of the order of 1 and is related to the limitation of the electron motion due to electron scattering off the surface [140]. The dielectric constant for bulk material ( $\epsilon_b$ ) over this wavelength range is available from reported experimental measurements [141]. Upon the damping correction the dielectric function becomes,

$$\epsilon = \epsilon_b + \frac{\omega_p^2}{\omega(\omega + i\gamma)} - \frac{\omega_p^2}{\omega(\omega + i\gamma + i\gamma_a)} \quad \text{Eqn 4-15}$$

The real and imaginary parts of  $\epsilon$  are separated as,

$$\epsilon_1 = \text{Re}(\epsilon_b) + \omega_p^2 \left[ \frac{1}{\omega^2 + \gamma^2} - \frac{1}{\omega^2 + (\gamma + \gamma_a)^2} \right] \quad \text{Eqn 4-16a}$$

$$\epsilon_2 = \text{Im}(\epsilon_b) - \frac{\omega_p^2}{\omega} \left[ \frac{\gamma}{\omega^2 + \gamma^2} - \frac{\gamma + \gamma_a}{\omega^2 + (\gamma + \gamma_a)^2} \right] \quad \text{Eqn 4-16b}$$

The refractive index value is thus corrected accordingly using Eqn 4-16a and 4-16b. Other experimentally measured constants for bulk material used in the simulation are listed in Table 4-2 [142].

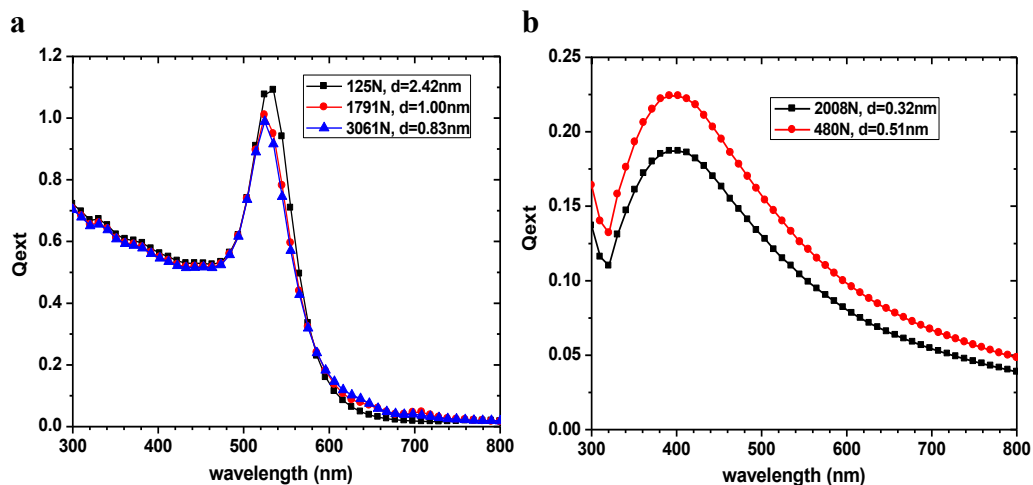
**Table 4-2 Parameters for Drude model used in the simulation [142].**

material	plasma freq (THz)	damping freq (Thz)	Fermi Velocity (m/s)
Au	2183	6.46	1410000
Ag	2180	4.353	1400000

The accuracy of the calculation is largely determined by dipole spacing. In order to guarantee the error is within a few percentile, the dipole spacing needs to be small enough so that [136]

$$|m| k d < 1 \quad \text{Eqn 4-17}$$

In the equation  $|m|$ ,  $k$ , and  $d$  are the absolute value of refractive index, wave number of incident light and dipole spacing respectively. Figure 4-9 shows two sets of data demonstrating the influence of dipole spacing on the simulation results. The plots present the calculated extinction efficiency factor  $Q_{\text{ext}}$ , which is the summation of absorption ( $Q_{\text{abs}}$ ) and scattering ( $Q_{\text{sca}}$ ) efficiency factor, versus the incident wavelength. While keeping other fixed parameters listed in Table 4-3, increasing the number of dipoles  $N$  thus shortening of the dipole distance  $d$  results in a slight change in maximum position, line width, and band intensity. More accurate results are obtained by using a larger number of dipoles. For simulation of 7.5 nm radius Au NPs, compared with sub 1 nm dipole spacing, using  $d = 2.42$  nm leads to obvious peak red shifting and broadening. For 2.5 nm radius Ag NPs, there is rather consistent maximum position by decrease of dipole spacing from 0.51 nm to 0.32 nm.



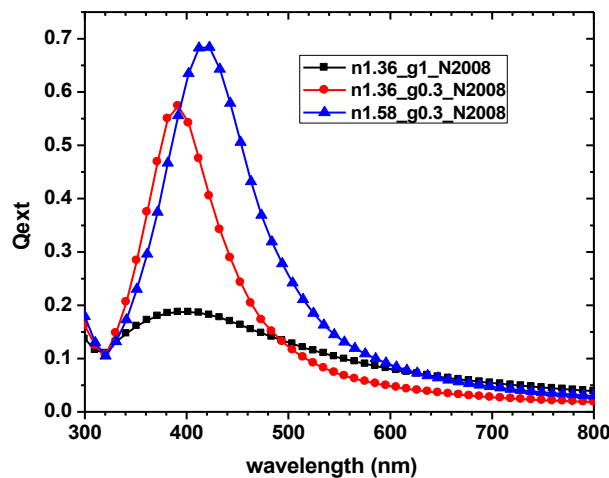
**Figure 4-9 Simulation of a single Au (a) and Ag (b) NP using different dipole spacing.** Other parameters are kept constant and listed in Table 4-3.

**Table 4-3 Parameters used in simulation shown in Figure 4-9.**

material	radius (nm)	medium	refractive index ( $n_m$ )*	g factor
Au	7.5	water	1.33	0
Ag	2.5	ethanol/silica/PVP	1.36	1

\* refractive index of the medium

Other factors that are significant for the simulation are the refractive index of the medium environment ( $n_m$ ) and g factor. The position of the maximum extinction efficiency factor is largely determined by medium refractive index. When all other parameters are fixed, increased  $n_m$  leads to red shifting of the band maximum accompanied with a higher band intensity and a broadened band width (Figure 4-10 red spheres and blue triangles). Also, the g factor plays an essential role on the band width and intensity. As shown in black rectangles and red spheres in Figure 4-10, using a g factor of 1 leads to too broadened SPR for 2.5 nm radius Ag NPs, while  $g = 0.3$  yields reasonable agreement with experimental data (blue triangle).



**Figure 4-10 Simulation results of a single Ag NP with two adjusted parameters (the medium refractive index and g factor)** The two parameters are changed one at a time while keeping the other fixed. Values of all other simulation parameters are listed in Table 4-4.

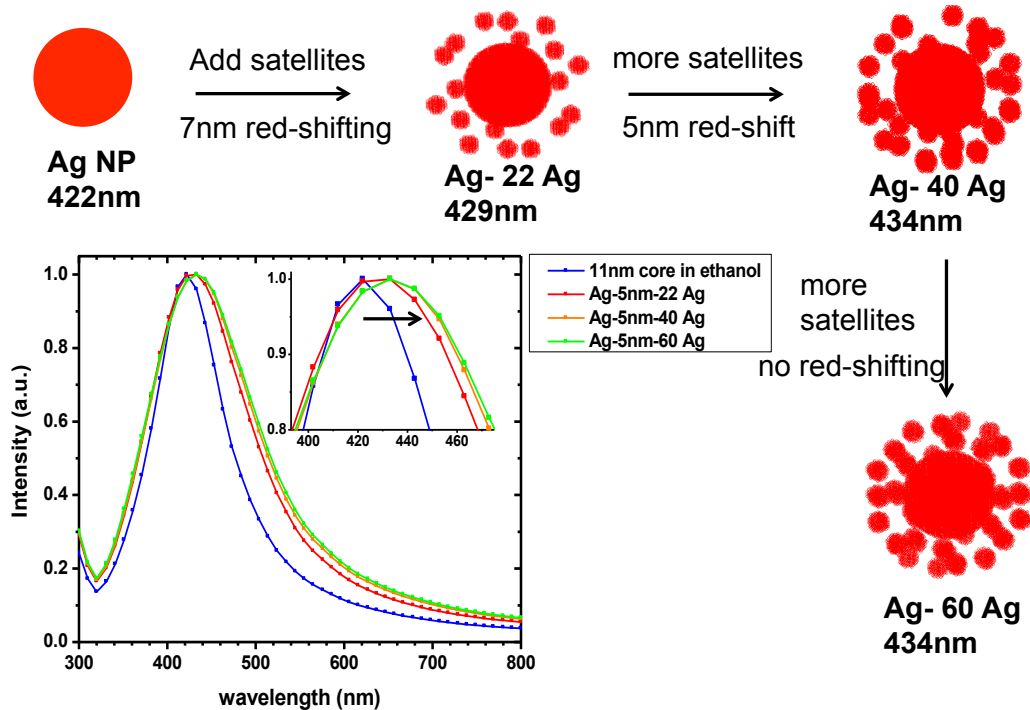
**Table 4-4 Parameters used in simulation shown in Figure 4-10.**

material	radius (nm)	number of dipoles (N)
Ag	2.5	2008

After the parameters for simulation of a single Ag NPs are optimized and the experimental data is reproduced, a cluster of Ag NPs modeling the core @ spacer – satellites structure is then simulated using the optimized parameters for a single Ag NPs. To simplify the modeling, only an isolated structure was simulated instead of the chain-like structure. To guarantee a reasonable accuracy, the choice of d value was small so that  $|m| k d \sim 0.02$ . The medium refractive index value of 1.58 was used for the environment of the ethanol, PVP and silica mixture [143]. To insure no overlap between the small Ag satellites around the core, a set of coordinates derived from a truncated icosahedron, which looks as a C<sub>60</sub> fullerene, was directly used to position 60 Ag satellites. Coordinates were randomly excluded for the 40 and 22 Ag satellites. As shown in Figure 4-11, the total 12 nm red shifting of the extinction efficiency band maximum for no Ag satellites to 60 Ag satellites matches the order of 19 nm total red shifting of the experimental results. However, there is no red shifting from 40 to 60 Ag coverage in the simulation and the band broadening is not as significant as the experiment (Figure 4-8). This discrepancy is most possibly caused

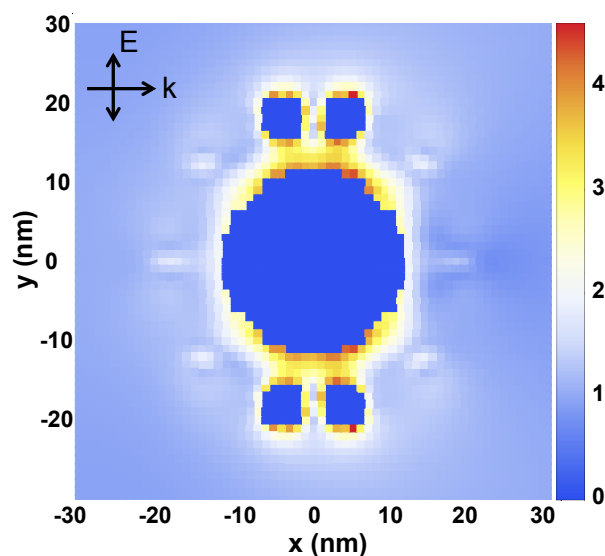


by onset of structure aggregates in experiments, thus core – core coupling and satellites – satellites coupling at adjacent shells come to play a role.



**Figure 4-11 Simulation of Ag @ 5 nm spacer – Ag satellites structures:** Models of structures with different Ag NP loadings shown in red are plotted with Gnuplot. The corresponding normalized extinction efficiency factors are shown in blue, red, orange and green curves, with increasing Ag coverage. The dipole spacing value  $d = 0.7$  nm was used in all simulations.

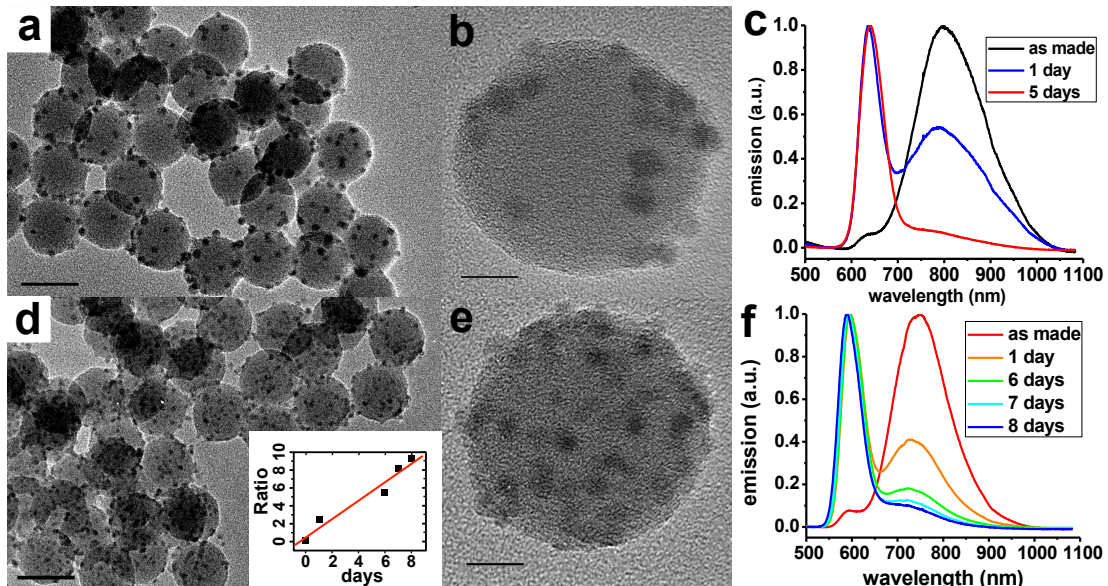
In addition to the reduction of the plasmon resonance energy due to the near field Coulomb interaction, a local electric field enhancement occurring at the gap of NPs is expected. The electric field amplitude distribution  $|\mathbf{E}/\mathbf{E}_0|$  upon 434 nm resonance excitation over the internal and surrounding space of the Ag @ 5 nm spacer – 60 Ag is shown in Figure 4-12. Field enhancement near the surface of small Ag satellites is present due to plasmon coupling with the core.



**Figure 4-12 Simulated normalized electric field amplitude  $|E/E_0|$  distribution on a Ag @ 5 nm spacer – 60 Ag structure, upon 434 nm resonance excitation, dipole spacing value  $d = 0.56$  nm ( $N = 54767$ ).**

6. Chemical conversion of silica-Ag into hydrophilic silica-CdSe quantum dots composites from silica-Ag composites

Finally the Ag NPs attached on the silica nano-spheres were converted into CdSe quantum dots via the reaction with Se precursor and then cation exchange. This resulted in an assembly of quantum dots loaded on 50 nm silica nano-spheres, with size dependent optical feature of both band gap and trap state emission. Moreover, the ratio of emission intensity for band gap transition versus trap state was found to increase over time, indicating changes on surface states of the CdSe NPs on silica. Such hydrophilic silica nano-spheres integrated with quantum dots have potential application in drug delivery and bioimaging probes [144].



**Figure 4-13** Characterization of silica-CdSe composites emitting at 640 nm (a – c) and 590 nm (d – f): (a) (d) Low-resolution TEM images, scale bars are 50 nm; (b) (e) corresponding high-magnification TEM images, scale bars are 10 nm; and (c) (f) Normalized time-dependent fluorescence spectra (excited with 400 nm blue laser) of the two samples measured as made and after different aging stages, shown as curves in different colors. (**Inset of d**) ratio of emission intensity for band gap transition over trap state emission versus aging time (black rectangle) and the linear fit (red curve)

Two batches of silica-CdSe sample with different quantum dot sizes were synthesized, by chemical conversion of two different silica-Ag samples. The morphologies of the silica-CdSe composites were characterized by TEM shown in Figure 4-13, and their corresponding optical emission properties are presented in Figure 4-13 c and f, respectively. Emission spectra are rescaled to facilitate comparison, by setting the baseline to zero and the maximum to one. The band gap

emission peaks at 640 nm and 590 nm confirm the different sizes of the quantum dots. Interestingly, for both sample as made and excited by a 400 nm blue laser, emission profiles were dominated by a broad (140 nm FWHM) trap emission band, accompanied by a small shoulder due to the band edge emission. Following aging in air for several days, the intensity of trap emission started to decrease with a concomitant blue shifting, and the narrower (60 nm FWHM) band edge emission emerged as the dominant feature. As shown in the inset of Figure 4-13 d, the intensity ratio of band edge emission over trap emission changed from the order of 0.1 to 10 over eight days. The time evolution of trap state to band gap emission indicates changes of the surface state attributed to surface defects and vacancies [145, 146]. The origin for this change is undetermined, but may relate to cation exchange.

## 7. Summary

This work introduces a facile synthetic route to uniform Ag NPs on silica nanospheres, and demonstrates the manipulation of key Ag NPs factors: size, shape and surface coverage (NP loading) on silica. Further, core @ shell – satellites metallic chain-like assembly structures were synthesized by adapting our Ag satellites growth method. Dipole – dipole coupling among the metallic assembly structures was evident on both Au @ silica – Ag and Ag @ silica – Ag structures. The systematic red shifting of SPR caused by increased surface coverage of Ag satellites was observed and the order of shifting was accounted for by DDA simulation. The silica-Ag and core @ shell – Ag metallic chain-like nanostructure are candidates for highly stable,

performance – enhanced catalysis and general Raman enhancement applications. To make individually dispersed Au @ silica –Ag nanostructures, a polysorbate can be adsorbed to improve the colloidal stability of individual APS functionalized Au @ silica NPs [49]. This would allow for systematic study of distance dependent dipole – dipole coupling between the plasmonic core and the outer Ag satellites within a single isolated structure. Finally, the silica – Ag composites were converted to hydrophilic silica – CdSe quantum dot composites, which exhibited size dependent band gap fluorescence and trap emission. Notably, over several days aging in air, the intensity ratio of trap emission versus band edge emission increased from the order of 0.1 to 10, due to change of surface state.

## Chapter 5: Summary and Future Outlook

Throughout this dissertation, I have presented recent efforts to build up complicated hybrid nanostructures from metal and semiconductor nanoparticles. Hybrid nanostructures are interesting because coupling effects can occur between similar/dissimilar domains that interact with each other in novel ways, e.g. plasmon – plasmon coupling and plasmon – exciton coupling. Tuning the composition and geometry can allow manipulation of nanostructure properties, and enable applications in multidisciplinary areas. Recently developed synthetic strategies have led to fabrication of new varieties of hybrid nanostructures. Chapter 2 has emphasized and reviewed the non-epitaxial strategy that has been applied to realize remarkable monocrystalline and morphology control on metal @ semiconducting core @ shell hybrid nanostructures. Promising improvements have been made to allow flexible combinations of core and shell in terms of chemical composition, size and shape. Further improvements such as new Se and Te precursors might be necessary to extend the scope of engineered optical properties. Also, improving the reproducibility of uniform cubic-shaped Au nanoparticles ensembles is highly desirable, for supply as starting material to allow for scalable hybrid product.

The metal-semiconductor interface is not yet well understood. Prevalence of defects or reconstruction might be expected to occur at the interface due to the large lattice mismatch. One study [92] has indicated few defects, as well as the existence of a potential barrier at the Au-CdS interface, due to the nonepitaxial nature of the

material. A high potential barrier is able to serve as a spacer to prevent charge transfer between the metal and semiconductor, and thus critical for study of Coulomb interaction of plasmon and exciton. Gaining more knowledge of the interface is an important and challenging area for future study.

Finite control of nanostructure over composition and morphology has been demonstrated in Chapter 3. Anisotropically shaped pseudobinary  $\text{CdS}_x\text{Se}_{1-x}$  nanocrystals including polygon, bullet, rods and multipods nanostructures have been synthesized for the first time. The nanorods ensemble exhibit tunable bright band gap fluorescence that is dependent on dimension. The gradient energy bands generated by one-dimensional gradient composition are of fundamental interest and potential practical importance. Gradient energy bands could enable unidirectional emission and have potential applications in nanoelectronic devices. The nanocrystal growth mechanism is proposed, and supported with control experiments, which suggest that octanethiol acts as a shape directing reagent and oxygen is shown to also factor into the formation of the anisotropically shaped nanocrystals. This part of work helps to gain better understanding of how organic molecules/oxygen can assist to shape the nanocrystal.

Lastly, a core – satellites styled nanostructure has been introduced. A facile synthetic route is demonstrated to realize control growth of Ag NPs as satellites. Plasmon – plasmon coupling has occurred among the core @ shell – satellites chain-like metallic assembly structures, characterized by systematic red shifting of SPR and convinced by numerical simulation. For future study of distance dependent dipole – dipole coupling between the plasmonic core and the surrounding Ag satellites,

individually dispersed (rather than onset of aggregates) core – satellites nanostructure needs to be prepared. The individual surface functionalized Au @ silica colloid could gain sufficient stability by wrapping with a polysorbate [49].



## Bibliography

- [1] Dusastre, V., The invisible revolution. *Nature* **2008**, *451*, 770-771.
- [2] Horikoshi, S.; Serpone, N., Introduction to Nanoparticles. In *Microwaves in Nanoparticle Synthesis*, Wiley-VCH Verlag GmbH & Co. KGaA: 2013; pp 1-24.
- [3] Gribbin, J.; Gribbin, M., *Richard Feynman: A Life in Science*. 1st ed.; Dutton: New York, 1997; p 170.
- [4] Noginov, M. A.; Zhu, G.; Belgrave, A. M.; Bakker, R.; Shalaev, V. M.; Narimanov, E. E.; Stout, S.; Herz, E.; Suteewong, T.; Wiesner, U., Demonstration of a spaser-based nanolaser. *Nature* **2009**, *460*, 1110-1112.
- [5] Zhang, J.; Tang, Y.; Lee, K.; Ouyang, M., Tailoring light-matter-spin interactions in colloidal hetero-nanostructures. *Nature* **2010**, *466*, 91-95.
- [6] Weng, L.; Zhang, H.; Govorov, A. O.; Ouyang, M., Hierarchical synthesis of non-centrosymmetric hybrid nanostructures and enabled plasmon-driven photocatalysis. *Nat Commun* **2014**, *5*.
- [7] Howes, P. D.; Chandrawati, R.; Stevens, M. M., Colloidal nanoparticles as advanced biological sensors. *Science* **2014**, *346*.
- [8] Wagner, F. E.; Haslbeck, S.; Stievano, L.; Calogero, S.; Pankhurst, Q. A.; Martinek, K.-P., Before striking gold in gold-ruby glass. *Nature* **2000**, *407*, 691-692.
- [9] Faraday, M., The Bakerian Lecture: Experimental Relations of Gold (and Other Metals) to Light. *Philosophical Transactions of the Royal Society of London* **1857**, *147*, 145-181.
- [10] Xia, Y.; Halas, N. J., Shape-Controlled Synthesis and Surface Plasmonic Properties of Metallic Nanostructures. *MRS Bull.* **2005**, *30*, 338-348.
- [11] Link, S.; El-Sayed, M. A., Shape and size dependence of radiative, non-radiative and photothermal properties of gold nanocrystals. *Int. Rev. Phys. Chem.* **2000**, *19*, 409-453.
- [12] Njoki, P. N.; Lim, I. I. S.; Mott, D.; Park, H.-Y.; Khan, B.; Mishra, S.; Sujakumar, R.; Luo, J.; Zhong, C.-J., Size Correlation of Optical and Spectroscopic Properties for Gold Nanoparticles. *J. Phys. Chem. C* **2007**, *111*, 14664-14669.

- [13] Link, S.; El-Sayed, M. A., Size and Temperature Dependence of the Plasmon Absorption of Colloidal Gold Nanoparticles. *J. Phys. Chem. B* **1999**, *103*, 4212-4217.
- [14] Xue, C.; Mirkin, C. A., pH-Switchable Silver Nanoprism Growth Pathways. *Angew. Chem. Int. Ed.* **2007**, *46*, 2036-2038.
- [15] Huang, X.; El-Sayed, M. A., Gold nanoparticles: Optical properties and implementations in cancer diagnosis and photothermal therapy. *Journal of Advanced Research* **2010**, *1*, 13-28.
- [16] Kelly, K. L.; Coronado, E.; Zhao, L. L.; Schatz, G. C., The Optical Properties of Metal Nanoparticles: The Influence of Size, Shape, and Dielectric Environment. *J. Phys. Chem. B* **2002**, *107*, 668-677.
- [17] Link, S.; Mohamed, M. B.; El-Sayed, M. A., Simulation of the Optical Absorption Spectra of Gold Nanorods as a Function of Their Aspect Ratio and the Effect of the Medium Dielectric Constant. *J. Phys. Chem. B* **1999**, *103*, 3073-3077.
- [18] Lee, K.-S.; El-Sayed, M. A., Dependence of the Enhanced Optical Scattering Efficiency Relative to That of Absorption for Gold Metal Nanorods on Aspect Ratio, Size, End-Cap Shape, and Medium Refractive Index. *J. Phys. Chem. B* **2005**, *109*, 20331-20338.
- [19] Daniel, M.-C.; Astruc, D., Gold Nanoparticles: Assembly, Supramolecular Chemistry, Quantum-Size-Related Properties, and Applications toward Biology, Catalysis, and Nanotechnology. *Chem. Rev.* **2004**, *104*, 293-346.
- [20] Xu, L.; Kuang, H.; Wang, L.; Xu, C., Gold nanorod ensembles as artificial molecules for applications in sensors. *J. Mater. Chem.* **2011**, *21*, 16759-16782.
- [21] Nie, S.; Emory, S. R., Probing Single Molecules and Single Nanoparticles by Surface-Enhanced Raman Scattering. *Science* **1997**, *275*, 1102-1106.
- [22] Kühn, S.; Håkanson, U.; Rogobete, L.; Sandoghdar, V., Enhancement of Single-Molecule Fluorescence Using a Gold Nanoparticle as an Optical Nanoantenna. *Phys. Rev. Lett.* **2006**, *97*, 017402.
- [23] Ni, W.; Yang, Z.; Chen, H.; Li, L.; Wang, J., Coupling between Molecular and Plasmonic Resonances in Freestanding Dye-Gold Nanorod Hybrid Nanostructures. *J. Am. Chem. Soc.* **2008**, *130*, 6692-6693.

- [24] Rossetti, R.; Nakahara, S.; Brus, L. E., Quantum size effects in the redox potentials, resonance Raman spectra, and electronic spectra of CdS crystallites in aqueous solution. *The Journal of Chemical Physics* **1983**, *79*, 1086-1088.
- [25] Brus, L. E., Electron - electron and electron - hole interactions in small semiconductor crystallites: The size dependence of the lowest excited electronic state. *The Journal of Chemical Physics* **1984**, *80*, 4403-4409.
- [26] Murray, C. B.; Norris, D. J.; Bawendi, M. G., Synthesis and characterization of nearly monodisperse CdE (E = sulfur, selenium, tellurium) semiconductor nanocrystallites. *J. Am. Chem. Soc.* **1993**, *115*, 8706-8715.
- [27] Bawendi, M. <http://nanocluster.mit.edu/research.php>.
- [28] Singh, A.; Li, X.; Protasenko, V.; Galantai, G.; Kuno, M.; Xing, H.; Jena, D., Polarization-Sensitive Nanowire Photodetectors Based on Solution-Synthesized CdSe Quantum-Wire Solids. *Nano Lett.* **2007**, *7*, 2999-3006.
- [29] Peng, X.; Manna, L.; Yang, W.; Wickham, J.; Scher, E.; Kadavanich, A.; Alivisatos, A. P., Shape control of CdSe nanocrystals. *Nature* **2000**, *404*, 59-61.
- [30] Ithurria, S.; Tessier, M. D.; Mahler, B.; Lobo, R. P. S. M.; Dubertret, B.; Efros, A. L., Colloidal nanoplatelets with two-dimensional electronic structure. *Nat. Mater.* **2011**, *10*, 936-941.
- [31] Manna, L.; Milliron, D. J.; Meisel, A.; Scher, E. C.; Alivisatos, A. P., Controlled growth of tetrapod-branched inorganic nanocrystals. *Nat. Mater.* **2003**, *2*, 382-385.
- [32] Manna, L.; Scher, E. C.; Alivisatos, A. P., Synthesis of Soluble and Processable Rod-, Arrow-, Teardrop-, and Tetrapod-Shaped CdSe Nanocrystals. *J. Am. Chem. Soc.* **2000**, *122*, 12700-12706.
- [33] Yu, H.; Li, J.; Loomis, R. A.; Wang, L.-W.; Buhro, W. E., Two- versus three-dimensional quantum confinement in indium phosphide wires and dots. *Nat. Mater.* **2003**, *2*, 517-520.
- [34] Li, L.-s.; Hu, J.; Yang, W.; Alivisatos, A. P., Band Gap Variation of Size- and Shape-Controlled Colloidal CdSe Quantum Rods. *Nano Lett.* **2001**, *1*, 349-351.
- [35] Wang, X.-Y.; Zhang, J.-Y.; Nazzal, A.; Darragh, M.; Xiao, M., Electronic structure transformation from a quantum-dot to a quantum-wire system: Photoluminescence decay and polarization of colloidal CdSe quantum rods. *Appl. Phys. Lett.* **2002**, *81*, 4829-4831.

- [36] Qu, L.; Peng, X., Control of Photoluminescence Properties of CdSe Nanocrystals in Growth. *J. Am. Chem. Soc.* **2002**, *124*, 2049-2055.
- [37] Jasieniak, J.; Mulvaney, P., From Cd-Rich to Se-Rich – the Manipulation of CdSe Nanocrystal Surface Stoichiometry. *J. Am. Chem. Soc.* **2007**, *129*, 2841-2848.
- [38] Peng, X.; Schlamp, M. C.; Kadavanich, A. V.; Alivisatos, A. P., Epitaxial Growth of Highly Luminescent CdSe/CdS Core/Shell Nanocrystals with Photostability and Electronic Accessibility. *J. Am. Chem. Soc.* **1997**, *119*, 7019-7029.
- [39] Dabbousi, B. O.; Rodriguez-Viejo, J.; Mikulec, F. V.; Heine, J. R.; Mattoussi, H.; Ober, R.; Jensen, K. F.; Bawendi, M. G., (CdSe)ZnS Core–Shell Quantum Dots: Synthesis and Characterization of a Size Series of Highly Luminescent Nanocrystallites. *J. Phys. Chem. B* **1997**, *101*, 9463-9475.
- [40] Carbone, L.; Nobile, C.; De Giorgi, M.; Sala, F. D.; Morello, G.; Pompa, P.; Hytch, M.; Snoeck, E.; Fiore, A.; Franchini, I. R.; Nadasan, M.; Silvestre, A. F.; Chiodo, L.; Kudera, S.; Cingolani, R.; Krahne, R.; Manna, L., Synthesis and Micrometer-Scale Assembly of Colloidal CdSe/CdS Nanorods Prepared by a Seeded Growth Approach. *Nano Lett.* **2007**, *7*, 2942-2950.
- [41] Talapin, D. V.; Nelson, J. H.; Shevchenko, E. V.; Aloni, S.; Sadtler, B.; Alivisatos, A. P., Seeded Growth of Highly Luminescent CdSe/CdS Nanoheterostructures with Rod and Tetrapod Morphologies. *Nano Lett.* **2007**, *7*, 2951-2959.
- [42] Mauser, C.; Limmer, T.; Da Como, E.; Becker, K.; Rogach, A. L.; Feldmann, J.; Talapin, D. V., Anisotropic optical emission of single CdSe/CdS tetrapod heterostructures: Evidence for a wavefunction symmetry breaking. *Physical Review B* **2008**, *77*, 153303.
- [43] Grivas, C.; Li, C.; Andreakou, P.; Wang, P.; Ding, M.; Brambilla, G.; Manna, L.; Lagoudakis, P., Single-mode tunable laser emission in the single-exciton regime from colloidal nanocrystals. *Nat Commun* **2013**, *4*.
- [44] Jones, M. R.; Osberg, K. D.; Macfarlane, R. J.; Langille, M. R.; Mirkin, C. A., Templated Techniques for the Synthesis and Assembly of Plasmonic Nanostructures. *Chem. Rev.* **2011**, *111*, 3736-3827.
- [45] Carbone, L.; Cozzoli, P. D., Colloidal heterostructured nanocrystals: Synthesis and growth mechanisms. *Nano Today* **2010**, *5*, 449-493.

- [46] Lai, C.-W.; Hsiao, J.-K.; Chen, Y.-C.; Chou, P.-T., Spherical and Anisotropic Silica Shell Nanomaterials. In *Nanotechnologies for the Life Sciences*, Wiley-VCH Verlag GmbH & Co. KGaA: 2007.
- [47] Ow, H.; Larson, D. R.; Srivastava, M.; Baird, B. A.; Webb, W. W.; Wiesner, U., Bright and Stable Core–Shell Fluorescent Silica Nanoparticles. *Nano Lett.* **2004**, *5*, 113-117.
- [48] Ming, T.; Zhao, L.; Yang, Z.; Chen, H.; Sun, L.; Wang, J.; Yan, C., Strong Polarization Dependence of Plasmon-Enhanced Fluorescence on Single Gold Nanorods. *Nano Lett.* **2009**, *9*, 3896-3903.
- [49] Reineck, P.; Gómez, D.; Ng, S. H.; Karg, M.; Bell, T.; Mulvaney, P.; Bach, U., Distance and Wavelength Dependent Quenching of Molecular Fluorescence by Au@SiO<sub>2</sub> Core–Shell Nanoparticles. *ACS Nano* **2013**, *7*, 6636-6648.
- [50] Liz-Marzán, L. M.; Giersig, M.; Mulvaney, P., Synthesis of Nanosized Gold–Silica Core–Shell Particles. *Langmuir* **1996**, *12*, 4329-4335.
- [51] Tokmakoff, A. 12.1. Forster Resonance Energy Transfer. <http://www.mit.edu/~tokmakof/TDQMS/Notes/12.1.%20Forster.pdf> (accessed 10/09/2013).
- [52] Sahoo, H., Förster resonance energy transfer – A spectroscopic nanoruler: Principle and applications. *Journal of Photochemistry and Photobiology C: Photochemistry Reviews* **2011**, *12*, 20-30.
- [53] Stockman, M. I., The spaser as a nanoscale quantum generator and ultrafast amplifier. *Journal of Optics* **2010**, *12*, 024004-024017.
- [54] Zhang, J.; Tang, Y.; Lee, K.; Ouyang, M., Nonepitaxial Growth of Hybrid Core-Shell Nanostructures with Large Lattice Mismatches. *Science* **2010**, *327*, 1634-1638.
- [55] Fröhlich, D.; Nöthe, A.; Reimann, K., Observation of the Resonant Optical Stark Effect in a Semiconductor. *Phys. Rev. Lett.* **1985**, *55*, 1335-1337.
- [56] Pryor, C. E.; Flatté, M. E., Predicted ultrafast single-qubit operations in semiconductor quantum dots. *Appl. Phys. Lett.* **2006**, *88*, -.
- [57] Jain, P. K.; Huang, W.; El-Sayed, M. A., On the Universal Scaling Behavior of the Distance Decay of Plasmon Coupling in Metal Nanoparticle Pairs: A Plasmon Ruler Equation. *Nano Lett.* **2007**, *7*, 2080-2088.

- [58] Wustholz, K. L.; Henry, A.-I.; McMahon, J. M.; Freeman, R. G.; Valley, N.; Piotti, M. E.; Natan, M. J.; Schatz, G. C.; Duyne, R. P. V., Structure–Activity Relationships in Gold Nanoparticle Dimers and Trimers for Surface-Enhanced Raman Spectroscopy. *J. Am. Chem. Soc.* **2010**, *132*, 10903-10910.
- [59] Chen, G.; Wang, Y.; Yang, M.; Xu, J.; Goh, S. J.; Pan, M.; Chen, H., Measuring Ensemble-Averaged Surface-Enhanced Raman Scattering in the Hotspots of Colloidal Nanoparticle Dimers and Trimers. *J. Am. Chem. Soc.* **2010**, *132*, 3644-3645.
- [60] Lim, D.-K.; Jeon, K.-S.; Kim, H. M.; Nam, J.-M.; Suh, Y. D., Nanogap-engineerable Raman-active nanodumbbells for single-molecule detection. *Nat. Mater.* **2010**, *9*, 60-67.
- [61] Camden, J. P.; Dieringer, J. A.; Wang, Y.; Masiello, D. J.; Marks, L. D.; Schatz, G. C.; Van Duyne, R. P., Probing the Structure of Single-Molecule Surface-Enhanced Raman Scattering Hot Spots. *J. Am. Chem. Soc.* **2008**, *130*, 12616-12617.
- [62] Sheikholeslami, S.; Jun, Y.-w.; Jain, P. K.; Alivisatos, A. P., Coupling of Optical Resonances in a Compositionally Asymmetric Plasmonic Nanoparticle Dimer. *Nano Lett.* **2010**, *10*, 2655-2660.
- [63] Brousseau Iii, L. C.; Novak, J. P.; Marinakos, S. M.; Feldheim, D. L., Assembly of Phenylacetylene-Bridged Gold Nanocluster Dimers and Trimers. *Adv. Mater.* **1999**, *11*, 447-449.
- [64] Chen, G.; Wang, Y.; Tan, L. H.; Yang, M.; Tan, L. S.; Chen, Y.; Chen, H., High-Purity Separation of Gold Nanoparticle Dimers and Trimers. *J. Am. Chem. Soc.* **2009**, *131*, 4218-4219.
- [65] Alivisatos, A. P., Semiconductor Clusters, Nanocrystals, and Quantum Dots. *Science* **1996**, *271*, 933-937.
- [66] Eustis, S.; El-Sayed, M. A., Why gold nanoparticles are more precious than pretty gold: Noble metal surface plasmon resonance and its enhancement of the radiative and nonradiative properties of nanocrystals of different shapes. *Chem. Soc. Rev.* **2006**, *35*, 209-217.
- [67] Lee, J.-S.; Shevchenko, E. V.; Talapin, D. V., Au–PbS Core–Shell Nanocrystals: Plasmonic Absorption Enhancement and Electrical Doping via Intra-particle Charge Transfer. *J. Am. Chem. Soc.* **2008**, *130*, 9673-9675.
- [68] Lee, J.-S.; Bodnarchuk, M. I.; Shevchenko, E. V.; Talapin, D. V., “Magnet-in-the-Semiconductor” FePt–PbS and FePt–PbSe Nanostructures: Magnetic

- Properties, Charge Transport, and Magnetoresistance. *J. Am. Chem. Soc.* **2010**, *132*, 6382-6391.
- [69] Costi, R.; Saunders, A. E.; Elmalem, E.; Salant, A.; Banin, U., Visible Light-Induced Charge Retention and Photocatalysis with Hybrid CdSe–Au Nanodumbbells. *Nano Lett.* **2008**, *8*, 637-641.
- [70] Li, P.; Wei, Z.; Wu, T.; Peng, Q.; Li, Y., Au–ZnO Hybrid Nanopyramids and Their Photocatalytic Properties. *J. Am. Chem. Soc.* **2011**, *133*, 5660-5663.
- [71] Achermann, M., Exciton–Plasmon Interactions in Metal–Semiconductor Nanostructures. *The Journal of Physical Chemistry Letters* **2010**, *1*, 2837-2843.
- [72] Palmstrom, C. J., Epitaxy of Dissimilar Materials. *Annu. Rev. Mater. Sci.* **1995**, *25*, 389-415.
- [73] Fan, F.-R.; Liu, D.-Y.; Wu, Y.-F.; Duan, S.; Xie, Z.-X.; Jiang, Z.-Y.; Tian, Z.-Q., Epitaxial Growth of Heterogeneous Metal Nanocrystals: From Gold Nanooctahedra to Palladium and Silver Nanocubes. *J. Am. Chem. Soc.* **2008**, *130*, 6949-6951.
- [74] Chen, X.; Lou, Y.; Samia, A. C.; Burda, C., Coherency Strain Effects on the Optical Response of Core/Shell Heteronanostructures. *Nano Lett.* **2003**, *3*, 799-803.
- [75] Lee, K. Synthesis and Characterization of Functional One Dimensional Nanostructures. University of Maryland, College Park, 2011.
- [76] Li, M.; Yu, X.-F.; Liang, S.; Peng, X.-N.; Yang, Z.-J.; Wang, Y.-L.; Wang, Q.-Q., Synthesis of Au–CdS Core–Shell Hetero-Nanorods with Efficient Exciton–Plasmon Interactions. *Adv. Funct. Mater.* **2011**, *21*, 1788-1794.
- [77] Nan, F.; Liang, S.; Liu, X.-L.; Peng, X.-N.; Li, M.; Yang, Z.-J.; Zhou, L.; Hao, Z.-H.; Wang, Q.-Q., Sign-reversed and magnitude-enhanced nonlinear absorption of Au–CdS core–shell hetero-nanorods. *Appl. Phys. Lett.* **2013**, *102*, 163112.
- [78] Liu, X.-L.; Liang, S.; Nan, F.; Pan, Y.-Y.; Shi, J.-J.; Zhou, L.; Jia, S.-F.; Wang, J.-B.; Yu, X.-F.; Wang, Q.-Q., Stepwise synthesis of cubic Au–AgCdS core-shell nanostructures with tunable plasmon resonances and fluorescence. *Opt. Express* **2013**, *21*, 24793-24798.
- [79] Wang, H.; Sun, Z.; Lu, Q.; Zeng, F.; Su, D., One-Pot Synthesis of (Au Nanorod)–(Metal Sulfide) Core–Shell Nanostructures with Enhanced Gas-Sensing Property. *Small* **2012**, *8*, 1167-1172.

- [80] Son, D. H.; Hughes, S. M.; Yin, Y.; Paul Alivisatos, A., Cation Exchange Reactions in Ionic Nanocrystals. *Science* **2004**, *306*, 1009-1012.
- [81] Bording, J. K.; Taftø, J., Molecular-dynamics simulation of growth of nanocrystals in an amorphous matrix. *Physical Review B* **2000**, *62*, 8098-8103.
- [82] Love, J. C.; Estroff, L. A.; Kriebel, J. K.; Nuzzo, R. G.; Whitesides, G. M., Self-Assembled Monolayers of Thiolates on Metals as a Form of Nanotechnology. *Chem. Rev.* **2005**, *105*, 1103-1170.
- [83] Yoo, H.; Millstone, J. E.; Li, S.; Jang, J.-W.; Wei, W.; Wu, J.; Schatz, G. C.; Mirkin, C. A., Core-Shell Triangular Bifrustums. *Nano Lett.* **2009**, *9*, 3038-3041.
- [84] Zhang, Q.; Ge, J.; Pham, T.; Goebel, J.; Hu, Y.; Lu, Z.; Yin, Y., Reconstruction of Silver Nanoplates by UV Irradiation: Tailored Optical Properties and Enhanced Stability. *Angew. Chem. Int. Ed.* **2009**, *48*, 3516-3519.
- [85] Xiong, Y., Morphological changes in Ag nanocrystals triggered by citrate photoreduction and governed by oxidative etching. *Chem. Commun.* **2011**, *47*, 1580-1582.
- [86] Sheppard, N., The infra-red spectrum, and the assignment of the fundamental modes of vibration of thioacetic acid. *Transactions of the Faraday Society* **1949**, *45*, 693-697.
- [87] Mehta, S. K.; Chaudhary, S.; Kumar, S.; Bhasin, K. K.; Torigoe, K.; Sakai, H.; Abe, M., Surfactant assisted synthesis and spectroscopic characterization of selenium nanoparticles in ambient conditions. *Nanotechnology* **2008**, *19*, 295601.
- [88] NIST 1-Decanethiol, NIST Online Standard Reference Data Program. <http://webbook.nist.gov/cgi/cbook.cgi?ID=C143102&Mask=80> (accessed 01/29/2014).
- [89] Zeng, J.; Tao, J.; Su, D.; Zhu, Y.; Qin, D.; Xia, Y., Selective Sulfuration at the Corner Sites of a Silver Nanocrystal and Its Use in Stabilization of the Shape. *Nano Lett.* **2011**, *11*, 3010-3015.
- [90] Thomson, J. W.; Nagashima, K.; Macdonald, P. M.; Ozin, G. A., From Sulfur-Amine Solutions to Metal Sulfide Nanocrystals: Peering into the Oleylamine-Sulfur Black Box. *J. Am. Chem. Soc.* **2011**, *133*, 5036-5041.



- [91] Beberwyck, B. J.; Surendranath, Y.; Alivisatos, A. P., Cation Exchange: A Versatile Tool for Nanomaterials Synthesis. *J. Phys. Chem. C* **2013**, *117*, 19759-19770.
- [92] Lambright, S.; Butaeva, E.; Razgoniaeva, N.; Hopkins, T.; Smith, B.; Perera, D.; Corbin, J.; Khon, E.; Thomas, R.; Moroz, P.; Mereshchenko, A.; Tarnovsky, A.; Zamkov, M., Enhanced Lifetime of Excitons in Nonepitaxial Au/CdS Core/Shell Nanocrystals. *ACS Nano* **2013**, *8*, 352-361.
- [93] Murray, C. B.; Kagan, C. R.; Bawendi, M. G., SYNTHESIS AND CHARACTERIZATION OF MONODISPERSE NANOCRYSTALS AND CLOSE-PACKED NANOCRYSTAL ASSEMBLIES. *Annu. Rev. Mater. Sci.* **2000**, *30*, 545-610.
- [94] Buhro, W. E.; Colvin, V. L., Semiconductor nanocrystals: Shape matters. *Nat. Mater.* **2003**, *2*, 138-139.
- [95] Hu, J.; Li, L.-s.; Yang, W.; Manna, L.; Wang, L.-w.; Alivisatos, A. P., Linearly Polarized Emission from Colloidal Semiconductor Quantum Rods. *Science* **2001**, *292*, 2060-2063.
- [96] Kazes, M.; Lewis, D. Y.; Ebenstein, Y.; Mokari, T.; Banin, U., Lasing from Semiconductor Quantum Rods in a Cylindrical Microcavity. *Adv. Mater.* **2002**, *14*, 317-321.
- [97] Huynh, W. U.; Dittmer, J. J.; Alivisatos, A. P., Hybrid Nanorod-Polymer Solar Cells. *Science* **2002**, *295*, 2425-2427.
- [98] Gur, I.; Fromer, N. A.; Geier, M. L.; Alivisatos, A. P., Air-Stable All-Inorganic Nanocrystal Solar Cells Processed from Solution. *Science* **2005**, *310*, 462-465.
- [99] Zhang, Y.; Tang, Y.; Lee, K.; Ouyang, M., Catalytic and Catalyst-free Synthesis of CdSe Nanostructures with Single-Source Molecular Precursor and Related Device Application. *Nano Lett.* **2008**, *9*, 437-441.
- [100] Cui, Y.; Banin, U.; Björk, M. T.; Alivisatos, A. P., Electrical Transport through a Single Nanoscale Semiconductor Branch Point. *Nano Lett.* **2005**, *5*, 1519-1523.
- [101] Jun, Y.-w.; Choi, J.-s.; Cheon, J., Shape Control of Semiconductor and Metal Oxide Nanocrystals through Nonhydrolytic Colloidal Routes. *Angew. Chem. Int. Ed.* **2006**, *45*, 3414-3439.

- [102] Liu, L.; Zhuang, Z.; Xie, T.; Wang, Y.-G.; Li, J.; Peng, Q.; Li, Y., Shape Control of CdSe Nanocrystals with Zinc Blende Structure. *J. Am. Chem. Soc.* **2009**, *131*, 16423-16429.
- [103] Ithurria, S.; Dubertret, B., Quasi 2D Colloidal CdSe Platelets with Thicknesses Controlled at the Atomic Level. *J. Am. Chem. Soc.* **2008**, *130*, 16504-16505.
- [104] Shieh, F.; Saunders, A. E.; Korgel, B. A., General Shape Control of Colloidal CdS, CdSe, CdTe Quantum Rods and Quantum Rod Heterostructures. *J. Phys. Chem. B* **2005**, *109*, 8538-8542.
- [105] Swafford, L. A.; Weigand, L. A.; Bowers, M. J.; McBride, J. R.; Rapaport, J. L.; Watt, T. L.; Dixit, S. K.; Feldman, L. C.; Rosenthal, S. J., Homogeneously Alloyed CdS<sub>x</sub>Se<sub>1-x</sub> Nanocrystals: Synthesis, Characterization, and Composition/Size-Dependent Band Gap. *J. Am. Chem. Soc.* **2006**, *128*, 12299-12306.
- [106] Jang, E.; Jun, S.; Pu, L., High quality CdSeS nanocrystals synthesized by facile single injection process and their electroluminescence. *Chem. Commun.* **2003**, 2964-2965.
- [107] Zhong, X.; Feng, Y.; Knoll, W.; Han, M., Alloyed Zn<sub>x</sub>Cd<sub>1-x</sub>S Nanocrystals with Highly Narrow Luminescence Spectral Width. *J. Am. Chem. Soc.* **2003**, *125*, 13559-13563.
- [108] Zhong, X.; Han, M.; Dong, Z.; White, T. J.; Knoll, W., Composition-Tunable Zn<sub>x</sub>Cd<sub>1-x</sub>Se Nanocrystals with High Luminescence and Stability. *J. Am. Chem. Soc.* **2003**, *125*, 8589-8594.
- [109] Bailey, R. E.; Nie, S., Alloyed Semiconductor Quantum Dots: Tuning the Optical Properties without Changing the Particle Size. *J. Am. Chem. Soc.* **2003**, *125*, 7100-7106.
- [110] Chen, O.; Chen, X.; Yang, Y.; Lynch, J.; Wu, H.; Zhuang, J.; Cao, Y. C., Synthesis of Metal-Selenide Nanocrystals Using Selenium Dioxide as the Selenium Precursor. *Angew. Chem. Int. Ed.* **2008**, *47*, 8638-8641.
- [111] Hou, B.; Benito-Alifonso, D.; Webster, R.; Cherns, D.; Galana, M. C.; Fermín, D. J., Rapid phosphine-free synthesis of CdSe quantum dots: promoting the generation of Se precursors using a radical initiator. *J. Mater. Chem. A* **2014**, *2*, 6879-6886.
- [112] Chen, O.; Zhao, J.; Chauhan, V. P.; Cui, J.; Wong, C.; Harris, D. K.; Wei, H.; Han, H.-S.; Fukumura, D.; Jain, R. K.; Bawendi, M. G., Compact high-quality

- CdSe-CdS core-shell nanocrystals with narrow emission linewidths and suppressed blinking. *Nat. Mater.* **2013**, *12*, 445-451.
- [113] Wei, S.-H.; Zhang, S. B.; Zunger, A., First-principles calculation of band offsets, optical bowings, and defects in CdS, CdSe, CdTe, and their alloys. *J. Appl. Phys.* **2000**, *87*, 1304-1311.
- [114] Novikov, B. V.; Ilinskii, A. V.; Lieder, K. F.; Sokolov, N. S., Determination of exciton diffusion length from photoconductivity low-temperature spectra. *Phys. Status Solidi B* **1971**, *48*, 473-480.
- [115] Katari, J. E. B.; Colvin, V. L.; Alivisatos, A. P., X-ray Photoelectron Spectroscopy of CdSe Nanocrystals with Applications to Studies of the Nanocrystal Surface. *J. Phys. Chem.* **1994**, *98*, 4109-4117.
- [116] Liu, L.; Peng, Q.; Li, Y., An Effective Oxidation Route to Blue Emission CdSe Quantum Dots. *Inorg. Chem.* **2008**, *47*, 3182-3187.
- [117] Jasieniak, J.; Smith, L.; Embden, J. v.; Mulvaney, P.; Califano, M., Re-examination of the Size-Dependent Absorption Properties of CdSe Quantum Dots. *J. Phys. Chem. C* **2009**, *113*, 19468-19474.
- [118] Tao, A. R.; Habas, S.; Yang, P., Shape Control of Colloidal Metal Nanocrystals. *Small* **2008**, *4*, 310-325.
- [119] Henzie, J.; Andrews, S. C.; Ling, X. Y.; Li, Z.; Yang, P., Oriented assembly of polyhedral plasmonic nanoparticle clusters. *Proceedings of the National Academy of Sciences* **2013**, *110*, 6640-6645.
- [120] Lee, H. K.; Lee, Y. H.; Zhang, Q.; Phang, I. Y.; Tan, J. M. R.; Cui, Y.; Ling, X. Y., Superhydrophobic Surface-Enhanced Raman Scattering Platform Fabricated by Assembly of Ag Nanocubes for Trace Molecular Sensing. *ACS Applied Materials & Interfaces* **2013**, *5*, 11409-11418.
- [121] McFarland, A. D.; Van Duyne, R. P., Single Silver Nanoparticles as Real-Time Optical Sensors with Zeptomole Sensitivity. *Nano Lett.* **2003**, *3*, 1057-1062.
- [122] An, C.; Peng, S.; Sun, Y., Facile Synthesis of Sunlight-Driven AgCl:Ag Plasmonic Nanophotocatalyst. *Adv. Mater.* **2010**, *22*, 2570-2574.
- [123] Signori, A. M.; Santos, K. d. O.; Eising, R.; Albuquerque, B. L.; Giacomelli, F. C.; Domingos, J. B., Formation of Catalytic Silver Nanoparticles Supported on Branched Polyethyleneimine Derivatives. *Langmuir* **2010**, *26*, 17772-17779.

- [124] Lee, J.-M.; Kim, D.-W.; Lee, Y.-H.; Oh, S.-G., New Approach for Preparation of Silver-Polystyrene Heterogeneous Nanocomposite by Polyol Process. *Chem. Lett.* **2005**, *34*, 928-929.
- [125] You, L.; Mao, Y.; Ge, J., Synthesis of Stable SiO<sub>2</sub>@Au-Nanoring Colloids as Recyclable Catalysts: Galvanic Replacement Taking Place on the Surface. *J. Phys. Chem. C* **2012**, *116*, 10753-10759.
- [126] Deng, Z.; Chen, M.; Wu, L., Novel Method to Fabricate SiO<sub>2</sub>/Ag Composite Spheres and Their Catalytic, Surface-Enhanced Raman Scattering Properties. *J. Phys. Chem. C* **2007**, *111*, 11692-11698.
- [127] Hu, B.; Zhao, Y.; Zhu, H.-Z.; Yu, S.-H., Selective Chromogenic Detection of Thiol-Containing Biomolecules Using Carbonaceous Nanospheres Loaded with Silver Nanoparticles as Carrier. *ACS Nano* **2011**, *5*, 3166-3171.
- [128] Wei, H.; Xu, H., Hot spots in different metal nanostructures for plasmon-enhanced Raman spectroscopy. *Nanoscale* **2013**, *5*, 10794-10805.
- [129] Lee, D. C.; Mikulec, F. V.; Pelaez, J. M.; Koo, B.; Korgel, B. A., Synthesis and Magnetic Properties of Silica-Coated FePt Nanocrystals. *J. Phys. Chem. B* **2006**, *110*, 11160-11166.
- [130] Zhang, Q.; Li, W.; Wen, L.-P.; Chen, J.; Xia, Y., Facile Synthesis of Ag Nanocubes of 30 to 70 nm in Edge Length with CF<sub>3</sub>COOAg as a Precursor. *Chemistry – A European Journal* **2010**, *16*, 10234-10239.
- [131] Liz-Marzan, L. M.; Giersig, M.; Mulvaney, P., Synthesis of nanosized gold-silica core-shell particles. *Langmuir* **1996**, *12*, 4329-4335.
- [132] Silvert, P.-Y.; Herrera-Urbina, R.; Duvauchelle, N.; Vijayakrishnan, V.; Elhsissen, K. T., Preparation of colloidal silver dispersions by the polyol process. Part 1-Synthesis and characterization. *J. Mater. Chem.* **1996**, *6*, 573-577.
- [133] Pham, T.; Jackson, J. B.; Halas, N. J.; Lee, T. R., Preparation and characterization of gold nanoshells coated with self-assembled monolayers. *Langmuir* **2002**, *18*, 4915-4920.
- [134] Sun, Y.; Xia, Y., Shape-Controlled Synthesis of Gold and Silver Nanoparticles. *Science* **2002**, *298*, 2176-2179.
- [135] Zhang, Z.; Zhao, B.; Hu, L., PVP Protective Mechanism of Ultrafine Silver Powder Synthesized by Chemical Reduction Processes. *J. Solid State Chem.* **1996**, *121*, 105-110.

- [136] Draine, B. T.; Flatau, P. J., Discrete-Dipole Approximation For Scattering Calculations. *Journal of the Optical Society of America A* **1994**, *11*, 1491-1499.
- [137] Purcell, E. M.; Pennypacker, C. R., Scattering and Absorption of Light by Nonspherical Dielectric Grains. *Astrophysical Journal* **1973**, *186*, 705-714.
- [138] Ashcroft, N. W.; Mermin, N. D., *Solid State Physics*. Thomson Learning, Inc: Beijing, 1976; p 18.
- [139] Doyle, W. T.; Agarwal, A., Optical Extinction of Metal Spheres. *Journal of the Optical Society of America* **1965**, *55*, 305-308.
- [140] Voisin, C.; Del Fatti, N.; Christofilos, D.; Vallée, F., Ultrafast Electron Dynamics and Optical Nonlinearities in Metal Nanoparticles. *J. Phys. Chem. B* **2001**, *105*, 2264-2280.
- [141] Johnson, P. B.; Christy, R. W., Optical Constants of the Noble Metals. *Physical Review B* **1972**, *6*, 4370-4379.
- [142] Murata, K.-i.; Tanaka, H., Surface-wetting effects on the liquid-liquid transition of a single-component molecular liquid. *Nat Commun* **2010**, *1*, 16.
- [143] Billaud, P.; Huntzinger, J.-R.; Cottancin, E.; Lermé, J.; Pellarin, M.; Arnaud, L.; Broyer, M.; Del Fatti, N.; Vallée, F., Optical extinction spectroscopy of single silver nanoparticles. *Eur. Phys. J. D* **2007**, *43*, 271-274.
- [144] Kim, J.; Piao, Y.; Hyeon, T., Multifunctional nanostructured materials for multimodal imaging, and simultaneous imaging and therapy. *Chem. Soc. Rev.* **2009**, *38*, 372-390.
- [145] Lambe, J. J.; Klick, C. C.; Dexter, D. L., Nature of Edge Emission in Cadmium Sulfide. *Physical Review* **1956**, *103*, 1715-1720.
- [146] Bawendi, M. G.; Carroll, P. J.; Wilson, W. L.; Brus, L. E., Luminescence properties of CdSe quantum crystallites: Resonance between interior and surface localized states. *The Journal of Chemical Physics* **1992**, *96*, 946-954.